Ilmari Kangas

Validation of tissue simulant parameters for compliance standards of body worn devices

Faculty of Electronics, Communications and Automation

Thesis submitted for examination for the degree of Master of Science in Technology.

Helsinki 15.3.2011

Thesis supervisor:

Prof. Keijo Nikoskinen

Thesis instructor:

D.Sc. (Tech.) Jafar Keshvari

Aalto University
School of Science
and Technology

AALTO UNIVERSITY
SCHOOL OF SCIENCE AND TECHNOLOGY

ABSTRACT OF THE
MASTER'S THESIS

Author: Ilmari Kangas

Title: Validation of tissue simulant parameters for compliance standards of body worn devices

Date: 15.3.2011 Language: English Number of pages:8+66

Faculty of Electronics, Communications and Automation

Department of Radio Science and Technology

Professorship: Electromagnetics Code: S-96

Supervisor: Prof. Keijo Nikoskinen

Instructor: D.Sc. (Tech.) Jafar Keshvari

A project team PT 62209 of the TC 106 committee of the international standardization unit IEC is developing a new standard 62209-Part 2: "Procedure to determine the specific absorption rate (SAR) for wireless communication devices used in close proximity to the human body (frequency range of 30 MHz to 6 GHz)". In a typical SAR measurement procedure for wireless communications devices a flat phantom filled with tissue simulant liquid is used to represent a human body. This study took part in the development of the standard 62209-Part 2 by assessing the validity of the tissue simulant liquids proposed by IEC and FCC in exposure situations where the radiation source is located close to the body.

The aim of this work was to compare SAR, the amount of absorbed radiation, in an anatomically realistic human phantom and a flat phantom filled with the tissue simulant liquids. A flat phantom is expected to produce a slightly higher SAR in order to cover the worst case exposure scenarios. The study was conducted using the finite-difference time-domain method (FDTD) based simulation software package SEMCAD X. The human phantom was irradiated at several locations where body worn devices are typically expected to be held using different distances and frequencies.

In some simulated exposure scenarios it turned out that SAR measured in the flat phantom underestimated that to be expected in an actual human body. Therfore, the results of this study indicate that the proposed tissue simulant liquids might be inadequately suited for representing the dielectric parameters of the human body. However, further studies including a variety of human models should be conducted before drawing any final conclusion.

Keywords: Specific Absorption Rate, phantom, dipole antenna

AALTO-YLIOPISTO
TEKNILLINEN KORKEAKOULU

DIPLOMITYÖN
TIIVISTELMÄ

Tekijä: Ilmari Kangas

Työn nimi: Kudoksia simuloivien parametrien validisointi keholla kannettavien laitteiden altistusstandardeille

Päivämäärä: 15.3.2011 Kieli: Englanti Sivumäärä:8+66

Elektroniikan, tietoliikenteen ja automaation tiedekunta

Radiotieteen ja -tekniikan laitos

Professuuri: Sähkömagnetiikka Koodi: S-96

Valvoja: Prof. Keijo Nikoskinen

Ohjaaja: TkT Jafar Keshvari

Kansainvälisen standardisointiyksikön IEC:n komitean TC 106 projektiryhmä 62209 valmistelee parhaillaan standardia 62209-Part 2: "Procedure to determine the specific absorption rate (SAR) for wireless communication devices used in close proximity to the human body (frequency range of 30 MHz to 6 GHz)". Tyypillisesti langattoman viestintälaitteen ominaisabsorptionopeusmittauksessa käytetään kudoksia simuloivalla nesteellä täytettyä litteää fantomia edustamaan ihmiskehoa. Tämä työ otti osaa standardin 62209-Part 2:sen valmisteluun selvittämällä IEC:n ja FCC:n ehdottamien ihmiskudoksia simuloivien nesteiden kelpoisuutta altistustilanteissa, joissa säteilylähde sijaitsee lähellä kehoa.

Työn tarkoituksena oli verrata keskenään SAR:a, absorboituneen tehon määrää, anatomisesti todenmukaisessa ihmisfantomissa ja kudoksia simuloivalla nesteellä täytetyssä litteässä fantomissa. Litteän fantomin oletetaan lievästi yliarvioivan SAR:a, jotta aliarviointeja ei varmasti tapahtuisi. Tutkimus suoritettiin aika-alueen differenssimenetelmään (FDTD) pohjautuvalla simulointiohjelmistolla SEMCAD X. Ihmisfantomia säteilytettiin keholla kannettavien laitteiden tyypillisiltä olinpaikoilta useilta etäisyyksyyksiltä ja taajuuksilta.

Joissakin simuloiduissa altistustilanteissa havaittiin litteässä fantomissa mitatun SAR:n aliarvioivan todellisessa ihmiskehossa odotettua arvoa. Näin ollen työn lopputulos antaa vitteitä IEC:n ja FCC:n ehdottamien nesteparametrien ihmiskehon dieletristen parametrien edustuksen kyseenalaistamiseen. Lopullisten johtopäätösten tekemiseksi tulisi kuitenkin suoritettaa jatkotutkimuksia erilaisilla ihmisfantomeilla.

Avainsanat: Ominaisabsorptionopeus, fantomi, dipoliantenni

Preface

I would like to thank my thesis instructor D.Sc. Jafar Keshvari and supervisor Prof. Keijo Nikoskinen for their professional help and guidance. I would also like to express my gratitude to William Martin for revising the language of the thesis.

Helsinki, 17.1.2011

Ilmari Kangas

Contents

Symbols and abbreviations

Symbols

$\mathbf{B}$	magnetic flux density [Vs/m^2]
$\mathbf{E}$	electric field [V/m]
$\mathbf{H}$	magnetic field [A/m]
$\mathbf{D}$	electric flux density [As/m^2]
$H_{x,y,z}$	magnetic field component [A/m]
c	speed of light in vacuum $\approx 3 \times 10^8$ [m/s]
c_b	blood specific heat capacity [J/(kg C)]
c_p	specific heat capacity [J/(kg C)]
d	diameter [m]
E	energy [Ev]
$E_{x,y,z}$	electric field component [V/m]
f	frequency [Hz]
h	Planck's constant $\approx 6.626 \times 10^{-}34$ [J s]
k	tissue thermal conductivity [W/(C m)]
L	length [m]
P	power [W]
t	time [s]
T	temperature [C]
T_{art}	arterial inlet blood temperature [C]
W_b	blood perfusion
ρ	density of charges [C/m^3]
ρ_{eff}	effective density [C/m^3]
ϵ_r	relative permittivity
ϵ_0	permittivity in vacuum $\approx 8.8542 \times 10^{-}12$ [As/Vm]
μ	permeability [Vs/Am]
σ	conductivity [S/m]
$\Delta x, \Delta y, \Delta z$	lattice space increment
Δt	time increment

Abbreviations

ABC	Absorbing Boundary Condition
BMI	Body Mass Index
CAD	Computer Aided Design
CENELEC	European Commitee for Electrotechnical Standardization
CT	Computed Tomography
DUT	Device Under Test
EM	Electromagnetic
FCC	Federal Communications Commission
FDTD	Finite Difference Time Domain
ICNIRP	International Commision on Non-Ionizing Radiation
IEC	International Electrotechnical Commision
IEEE	The Institute of Electrical and Electronics Engineers
IRPA	The International Radiation Protection Association's
MIRD	Medical Internal Radiation Dose
MRI	Magnetic Resonance Imaging
NCRP	National Council on Radiation Protection and Measurements
PEC	Perfectly Electric Conductor
PML	Perfectly Matched Layer
RF	Radio Frequency
RFID	Radio Frequency Identification
SAR	Specific Absorption Rate
UPML	Uniaxial Perfectly Matched Layer
VC	Virtual Classroom
VF	Virtual Family
VHP	Visible Human Project
WHO	World Health Organization
WiFi	Wireless Fidelity

1 Introduction and objectives

International standards and regulations set exposure limits for wireless communication devices. Experimental compliance testing for a mobile phone that is to be introduced to the market is typically done with flat phantoms filled with human tissue simulating liquid. It is believed that the compliance testing of hand-held and body mounted devices can be assessed using a flat phantom filled with the body tissue simulating liquid as defined in the respective sections of the IEC (International Electrotechnical Commission) 62209 Part 2 standard. However, the reasoning is not sufficiently backed up by scientific data. Therefore, the standard needs to be amended with respect to this issue.

The main aim of this study was to evaluate the specific absorption rate (SAR) in the body of an anthropomorphic phantom when it is irradiated with a half-wave dipole antenna close to the body and to compare it against the SAR in the flat phantom filled with the tissue simulant liquids proposed by IEC and FCC (Federal Communications Commission). The SAR value describes how much radiated energy is absorbed by a certain mass in a tissue. For the tissue simulant liquids to be scientifically valid, the SAR in the flat phantom needs to slightly overestimate the SAR in the models derived from real humans, thus covering the worst case exposure scenarios.

The study was carried out with computer simulations. A finite difference time domain (FDTD) method based software package SEMCAD X was used as a simulation platform. The FDTD method provides a way to perform simulations whose results are in agreement with physical measurements done on phantoms. Thus, it is a feasible method for evaluating exposure schemes that would be burdensome or impossible to perform on physical phantoms. The study made use of an anatomically correct model of an adult male from the Virtual Family Project. Multiple frequencies, antenna distances from the object and locations on the phantom were considered in order to cover different exposure scenarios. A combination of these variables resulted in total of 432 simulations for the adult male phantom.

This thesis consists of eight chapters. Chapter 2 explains the basics of the FDTD method. The concept of Specific Absorption Rate (SAR) is introduced in Chapter 3. Additionally, further discussion on electromagnetic field absorption and biophysical effects is presented under this chapter. A brief description of various international standardization organizations engaged in formulating radio frequency safety standards, e.g. IEC and FCC, is given in Chapter 4. The purpose of the IEC 62209 Part 2 standard is explained at the end of the chapter. Chapter 5 provides an overview on phantoms employed in computer simulations and introduces the models utilized in this study. The actual simulation settings are described in detail in Chapter 6. The results are reported in Chapter 7. Finally, conclusions are drawn in Chapter 8.

2 Finite Difference Time Domain Method (FDTD)

The FDTD method is a computational technique for solving Maxwell's Equations for electromagnetics. It is mathematically straightforward and it is considered easy to understand. Other approaches to electromagnetic computation are, e.g. the Method of Moments, the finite element method, physical optics, theory of diffraction and finite integration theory. However, FDTD has become the most popular numerical method for a wide range of applications due to its exponentially increasing availability of computational power. It is feasible method for evaluating exposure schemes that would be practically impossible with analytical methods. Therefore, FDTD is excellently suited for calculating the specific absorption rate (SAR) levels and the induced currents in an anatomically based model of a human. Examples of FDTD based commercial software packages offering three-dimensional solutions to electromagnetic field problems are presented in Table 1.

Table 1: Examples of FDTD based commercial software.

Product	Manufacturer/supplier
CONCERTO	Vector Fields
EMPIRE XCcel^{TM}	IMST GmbH
FIDELITY	Zeland Software
GEMS	2COMU
SEMCAD X	SPEAG
XFDTD	Remcom

2.1 Maxwell's Equations

Maxwell's Equations in an isotropic (direction-independent), nondispersive (frequency independent) and linear (field-independent) medium can be written in differential form as

$$\nabla \times \mathbf{E} = -\frac{\partial \mathbf{B}}{\partial t} \tag{1}$$

$$\nabla \times \mathbf{H} = \frac{\partial \mathbf{D}}{\partial t} + \sigma \mathbf{E} \tag{2}$$

$$\nabla \cdot \mathbf{D} = \rho \tag{3}$$

$$\nabla \cdot \mathbf{B} = 0 \tag{4}$$

where the following material relations apply:

$$\mathbf{D} = \epsilon_r \epsilon_0 \mathbf{E} \tag{5}$$

$$\mathbf{B} = \mu_r \mu_0 \mathbf{H} \tag{6}$$

Equations (1) - (6) are all the needed information to describe every problem in electromagnetism. If the initial values, boundary conditions and field sources are specified, a solution for Maxwell's Equations is always found. However, for practical reasons, analytical solution can be obtained only for the simplest canonical field problems, such as the homogeneous sphere in a homogeneous electric field. In more complex situations numerical techniques have to be applied. In the FDTD method the computational domain is divided into, usually very small, rectangular cells referred to as voxels. The electric and magnetic fields are then calculated in every voxel using direct computational algorithms based on Maxwell's Equations.

Substituting Equations (5) and (6) to (1) and (2) yields Maxwell's curl equations

$$\frac{\partial \mathbf{H}}{\partial t} = -\frac{1}{\mu}\nabla \times \mathbf{E} - \frac{1}{\mu} \tag{7}$$

$$\frac{\partial \mathbf{E}}{\partial t} = \frac{1}{\epsilon}\nabla \times \mathbf{H} - \frac{\sigma}{\mu}\mathbf{E} \tag{8}$$

that are considered as the starting point of the FDTD method. Equations (7) and (8) are equivalent to the following set of six coupled scalar equations expressed in a Cartesian coordinate system:

$$\frac{\partial H_x}{\partial t} = \frac{1}{\mu}(\frac{\partial E_y}{\partial z} - \frac{\partial E_z}{\partial y}) \tag{9}$$

$$\frac{\partial H_y}{\partial t} = \frac{1}{\mu}(\frac{\partial E_z}{\partial x} - \frac{\partial E_x}{\partial z}) \tag{10}$$

$$\frac{\partial H_z}{\partial t} = \frac{1}{\mu}(\frac{\partial E_x}{\partial y} - \frac{\partial E_y}{\partial x}) \tag{11}$$

$$\frac{\partial E_x}{\partial t} = \frac{1}{\epsilon}(\frac{\partial H_z}{\partial y} - \frac{\partial H_y}{\partial z} - \sigma E_x) \tag{12}$$

$$\frac{\partial E_y}{\partial t} = \frac{1}{\epsilon}(\frac{\partial H_x}{\partial z} - \frac{\partial H_z}{\partial x} - \sigma E_y) \tag{13}$$

$$\frac{\partial E_z}{\partial t} = \frac{1}{\epsilon}(\frac{\partial H_y}{\partial x} - \frac{\partial H_x}{\partial y} - \sigma E_z) \tag{14}$$

The above field representation forms the basis of the FDTD numerical algorithm.

2.2 Yee algorithm

The algorithm used in FDTD simulations is known as the Yee algorithm. It was introduced by Kane Yee in 1966 as an approach to discretize Maxwell's time-dependent curl equations [1]. It was later developed by Allen Taflove, the coiner of the acronym FDTD, who was first to notice that it would be convenient to divide the computational space into so-called Yee cells. Each Yee cell in the physical volume of interest is assigned a material type that has corresponding dielectric properties in order to generate a valid representation of the structure.

As opposed to solving the electric or magnetic fields alone using a wave equation, the Yee algorithm solves both electric and magnetic fields using the coupled Maxwell's curl equations. As a result, this leads to a more robust solution than using either of the fields alone. The Yee cell defines the relative locations of the electric- and magnetic field components $(E_x, E_y, E_z, H_x, H_y, H_z)$ as illustrated in Figure 1. The fields are all offset by half a space step. The E field components are surrounded by four H field components and vice versa. However, this arrangement of field components in a Cartesian coordinate system is only one possibility among many others [2].

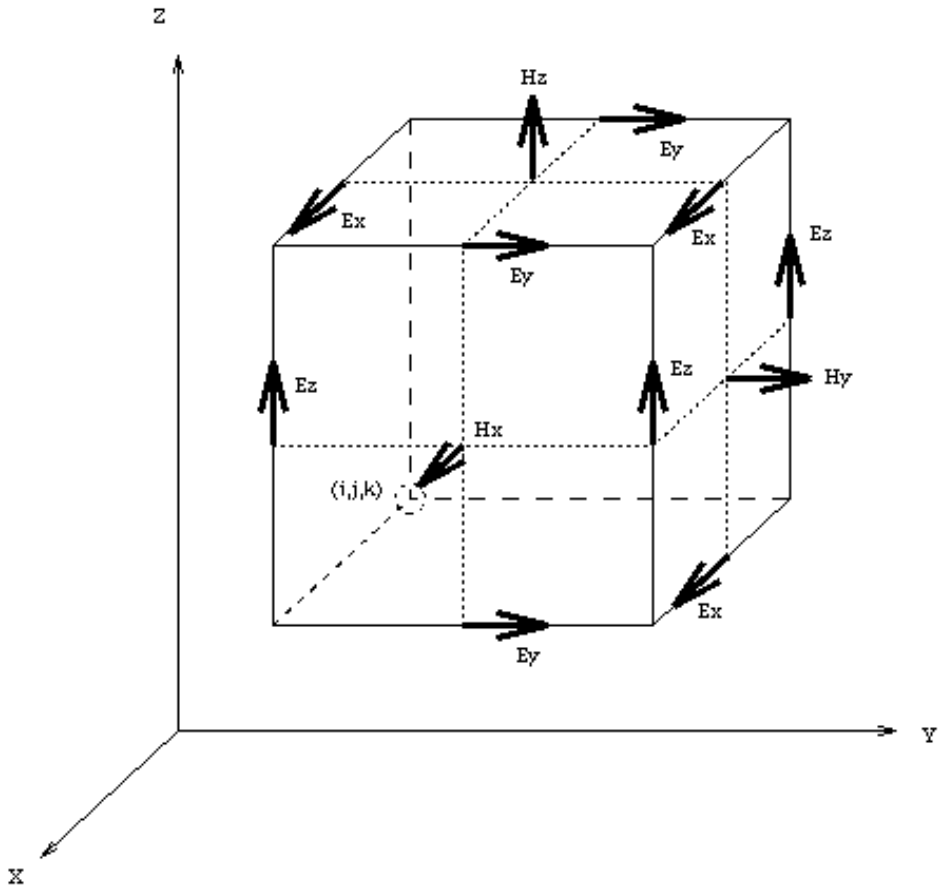

Figure 1: Yee cell.

In addition to being offset spatially, the Yee algorithm also centres its E and H components in time, so that the leapfrog time-stepping algorithm is imposed. All of the E field components in the space at a certain time instant are used to calculate the H field components at the next time instant. Then the new E field components are obtained from the previously calculated H field components. In this manner the cyclic process yields the E and H field components through the whole modelled space until time-stepping is concluded. Leapfrog time-stepping is fully explicit, so that there is no need to solve a system of linear simultaneous equations.

As a consequence, the required computer memory storage and execution time is remarkably low, proportional only to the number of electromagnetic field unknowns in the computational domain. The leapfrog algorithm has proven to be an accurate and robust algorithm for a variety of problems.

Using Yee's notation, any grid point is defined as

$$(i, j, k) \equiv (i\Delta x, j\Delta y, k\Delta z) \tag{15}$$

and any function of space and time as

$$F^n_{i,j,k} \equiv F(i\Delta, j\Delta, k\Delta, n\Delta t) \tag{16}$$

where $\Delta = \Delta x = \Delta y = \Delta z$ is the lattice space increment, Δt is the time increment and i, j, k are integers.

Space and time derivatives are approximated using central differences

$$\frac{\partial F^n_{i,j,k}}{\partial x} \approx \frac{F^n_{i+\frac{1}{2},j,k} - F^n_{i-\frac{1}{2},j,k}}{\Delta} \tag{17}$$

$$\frac{\partial F^n_{i,j,k}}{\partial t} \approx \frac{F^{n+\frac{1}{2}}_{i,j,k} - F^{n-\frac{1}{2}}_{i,j,k}}{\Delta t} \tag{18}$$

An easy way to demonstrate the FDTD algorithm is to examine an incident plane wave entering a region of space. It is assumed that the plane wave has only an electric field parallel to the z-axis and magnetic field parallel to the x-axis. Also, at time point $t = 0$ all electromagnetic fields in the sampling space are assumed to be identically zero.

Since only (9) and (14) involve both the E_z and H_x component, Equations (9)-(14) are reduced to

$$\frac{\partial H_x}{\partial t} = -\frac{1}{\mu}\frac{\partial E_z}{\partial y} \tag{19}$$

$$\frac{\partial E_z}{\partial t} = -\frac{1}{\epsilon}\frac{\partial H_x}{\partial y} - \sigma E_z \tag{20}$$

Discretizing the y- and t-axes using the Notations (15) and (16) and applying the central difference approximation yields the following representation for the H-field at $y = (j + \frac{1}{2})\Delta y$ and $t = n\Delta t$

$$\frac{\partial H_x|^n_{j+\frac{1}{2}}}{\partial t} = \frac{H_x|^{(n+\frac{1}{2})\Delta t}_{(j+\frac{1}{2})\Delta y} - H_x|^{(n-\frac{1}{2})\Delta t}_{(j+\frac{1}{2})\Delta y}}{\Delta t} = -\frac{1}{\mu}\frac{E_z|^{n\Delta t}_{(j+1)\Delta y} - E_z|^{n\Delta t}_{j\Delta y}}{\Delta y} \tag{21}$$

Thus, the H-field can be written at the latest time point $(n + \frac{1}{2})\Delta t$ as

$$H_x|^{(n+\frac{1}{2})\Delta t}_{(j+\frac{1}{2})\Delta y} = H_x|^{(n-\frac{1}{2})\Delta t}_{(j+\frac{1}{2})\Delta y} - \frac{\Delta t}{\mu\Delta y}(E_z|^{n\Delta t}_{(j+1)\Delta y} - E_z|^{n\Delta t}_{j\Delta y}) \tag{22}$$

Similar treatment for the E-field yields

$$\epsilon\frac{\partial E_z}{\partial t} = \frac{\epsilon E_z|_{j\Delta y}^{(n+1)\Delta t} - \epsilon E_z|_{j\Delta y}^{n\Delta t}}{\Delta t} =$$

$$-\frac{H_x|_{(j+\frac{1}{2})\Delta y}^{(n+\frac{1}{2})\Delta t} - H_x|_{(j+\frac{1}{2})\Delta y}^{(n-\frac{1}{2})\Delta t}}{\Delta y} - \sigma\frac{E_z|_{j\Delta y}^{(n+1)\Delta t} - E_z|_{j\Delta y}^{n\Delta t}}{2} \tag{23}$$

and for the E-field at $t = (n+1)\Delta t$

$$E_z|_{j\Delta y}^{(n+1)\Delta t} = \frac{2\Delta t}{2\epsilon + \Delta t\sigma}\left(\frac{H_x|_{(j-\frac{1}{2})\Delta y}^{(n+\frac{1}{2})\Delta t} - H_x|_{(j+\frac{1}{2})\Delta y}^{n\Delta t}}{\Delta y}\right) + \frac{2\epsilon - \Delta t\sigma}{2\epsilon + \Delta t\sigma}E_z|_{j\Delta t}^{n\Delta t} \tag{24}$$

Equations (22) and (24) are the so-called update equations and they characterise the fundamental principle of the FDTD method.

The leapfrog scheme is illustrated in Figure 2. As the above analysis denotes, at time step $t = n + 1/2$, the $H_x^{(j+\frac{1}{2})}$ component is calculated as a function of the previous value $t = n + 1/2$ $H_x^{(j-\frac{1}{2})}$ in the same mesh point, and as a function of the E_z component at time point $t = n$ in the adjacent mesh point. Correspondingly, the E_z component is calculated, at time step $t = n + 1$, as a function of the same component at the previous time step E_z^n, and as a function of the H_x component at time point $t = n + 1$ in the adjacent mesh point. Accordingly, with a time step Δt, calculations are performed at distinct time instants: t_1, t_2, t_3,..., where $t_1 = \Delta t$, $t_2 = 2\Delta t$, $t_3 = 3\Delta t$ for electric fields, and $t_1 = \Delta t/2$, $t_2 = 3\Delta t/2$, $t_3 = 5\Delta t/2$ for magnetic fields.

Propagation of the incident plane wave is modelled by the commencement of time-stepping, which is simply the implementation of the update equations to determine the field behaviour at certain time point and location. Time stepping continues as the incident wave eventually hits the modelled object contained within the sampling space. The outgoing scattered waves are then ideally terminated at the boundaries of the sampling region using proper boundary conditions. Finally, time-stepping is ended when the desired late-time pulse response or steady-state behaviour has been met.

2.3 Accuracy and Numerical Stability

The space grid size is critical regarding the accuracy of the FDTD method. The size must be chosen with care so that over one increment the electric and magnetic fields do not change substantially. Enough sampling points need to be taken to ensure accurate results at the highest frequency of interest. In turn, the available computational resources dictate the upper limit of accuracy of any computational simulation. Cell size is directly affected by the material parameters. Any increase in permittivity or conductivity means shorter wavelengths in the material, hence smaller cell size is required. A good rule of thumb is 10 cells per wavelength, which is sufficient to realize less than $\pm 7\%$ uncertainty of the FDTD solution of near

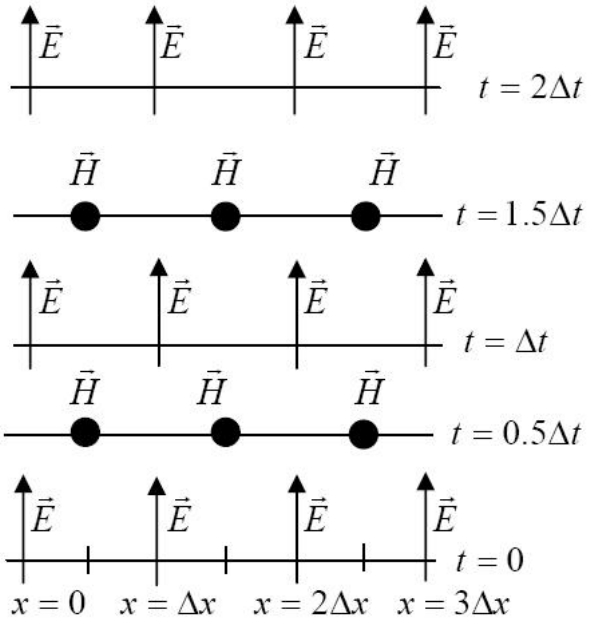

Figure 2: Interleaving of the electric and magnetic fields in space and time.

fields due to the approximation of the spatial derivatives [3]. However, some small scale features of the geometry might require higher resolution to ensure adequate representation.

2.3.1 Courant criterion

Once the cell size is determined, the stability of the update equations needs to be ensured by satisfying a certain relation between spatial and time intervals. The correct stability criterion, the Courant-Friedrich-Levy criterion (CFL), for the original Yee algorithm was first presented by Taflove [4]. The CFL criterion states that the time increment Δt must satisfy the following inequality

$$\Delta t \leq \frac{1}{c\sqrt{\frac{1}{(\Delta x)^2} + \frac{1}{(\Delta y)^2} + \frac{1}{(\Delta z)^2}}} \tag{25}$$

for a cubic lattice where c is the local wave phase velocity. The criterion dictates the limit for the maximum time step in order to preserve the stability. However, smaller time steps do not generally lead to substantial accuracy improvements. Essentially, the only effect is increased computational time. The most common situation in which the time step needs to be chosen smaller than CFL is when the simulation space contains conductive materials. Although, this is usually not a concern, since the smallest time step is derived from the speed of light in free space.

2.3.2 Staircase effect

The simulation accuracy is also dependent on the shape of the modelled geometry. As the space is divided into rectangular cells, the FDTD method performs a staircased approximation on the smoothly varying surfaces as illustrated in Figure 3.

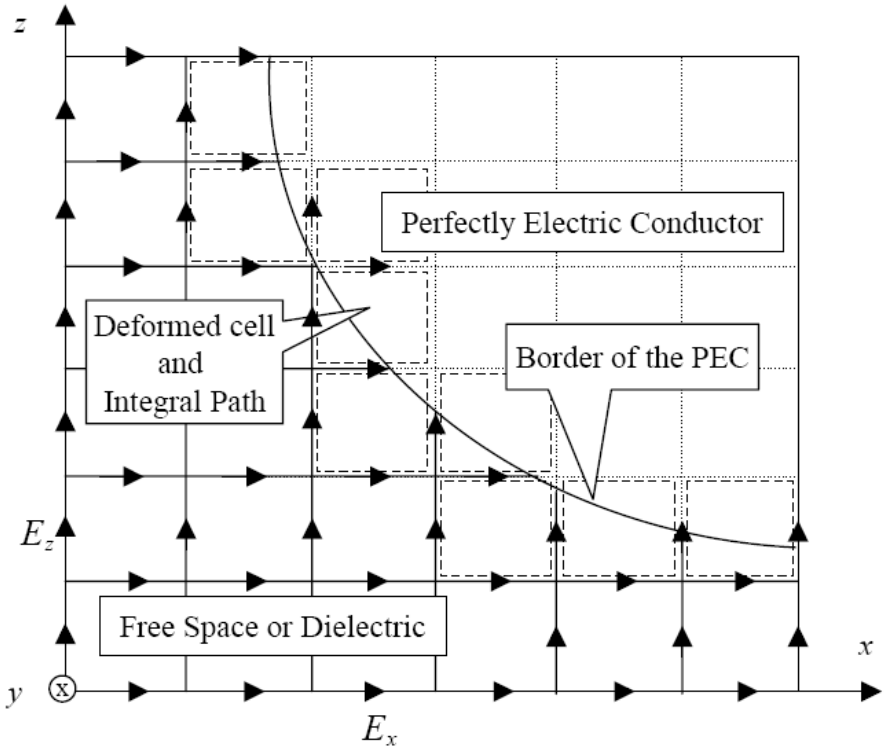

Figure 3: Intersection between the FDTD mesh and a PEC surface in the x-z plane.

In the case of perfect conductors with curved surfaces and edges, or structures non-conformally aligned with the grid this approximation may lead to significant errors. A method to reduce the staircase effect is to decrease the cell size, resulting in a finer grid. Then again, the computational efficiency might suffer for having an excessively fine grid on lesser priority areas of the model. One way to overcome this issue is to impose a grid with varying spatial increments along the different coordinate axis. Thus, finer cell size is applied only in the areas of rapid field fluctuation. An optimized grid can significantly reduce the simulation time and yield more accurate results. Additionally, the staircase effect can be reduced by using the Conformal FDTD algorithm. It is basically an enhanced conventional FDTD which makes more detailed representation of the geometry as shown in Figure 4.

2.3.3 Dispersion

Another issue regarding simulation accuracy is the grid dispersion error which is inherently present in the FDTD algorithm. The error arises when waves of differ-

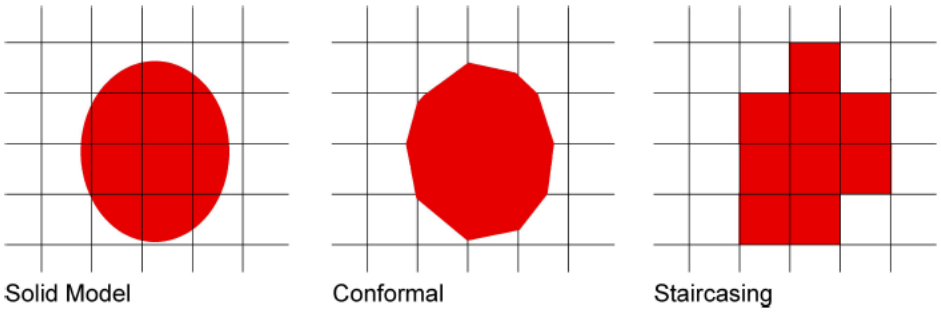

Figure 4: Demonstration of the Conformal FDTD algorithm.

ent frequencies progress at different speeds through the computational grid. Thus, dispersion errors accumulated in time can have a significant effect on the accuracy of results. For accurate and stable results, the solution to diminish this error is finer discretization of the grid. Again, the drawback of this method is the excessive computational resource demand as discussed above.

2.4 Boundary conditions

A basic difficulty encountered in applying the FDTD method, is how to model open-region problems. The central difference equations cannot be applied at the outer boundary since the updating of tangential component of the electric field requires magnetic field values at points outside of the lattice truncation. Since the computational domain has to be terminated somewhere because of the limited amount of computer storage capacity, a special treatment has to be implemented at the outer boundary. This is conducted by applying absorbing boundary conditions (ABC) in order to create the illusion of an infinite space. One of the active areas of FDTD research has been the quest for an ABC that produces negligible reflections [6]. Most of the popular ABCs can be divided into analytical and material-based techniques. The former are obtained by factoring the wave equation and the latter are based on the dampening of the fields as they propagate through the absorbing material medium. The accuracy of the FDTD method is proportional to the accuracy of the ABC.

In 1994 a highly efficient and flexible type of ABC called the perfect matched layer (PML) was introduced by J-P Berenger which was set to revolutionize the FDTD method [7],[8]. It is a widely accepted boundary condition and practice has shown it to to be orders of magnitude more absorbing than earlier ABCs [9]. The objective of the PML is to ensure that incident waves of arbitrary angle, frequency and polarization are matched at the outer boundary. The principle function of the PML is based on splitting vector field components into two orthogonal components in the PML region and then giving each one separate treatment regarding loss parameter adjustment. As a result, the propagating wave in the PML medium is attenuated by lossy layers and finally reflected back from the last layer when the amplitude is reduced by several orders of magnitude.

A later formulation of the Berenger's PML that has gained popularity due to its simplicity and efficiency is called the Uniaxial Perfectly Matched Layer (UPML). It was introduced by S. Gedney in 1996 and it is physically and mathematically equal to Berenger's PML. The main advantages of the UPML over Berenger's PML are that the formulation is based on Maxwell's Equations, rather than a modified set of equations, and the application to the FDTD method is more computationally efficient [10]. Furthermore, the UPML extends the use of the PML to nonorthogonal coordinate systems. The UPML technique is employed by the electromagnetic simulation tool SEMCAD X, which was used to conduct this study.

2.5 Advantages and disadvantages of FDTD

The FDTD method is computationally simple, no formulation of integral equations of matrix algebra is required. It is a powerful technique to model different types of materials, e.g. anisotropic, dispersive, inhomogeneous, located in the computational domain. Besides dealing with electric devices, the method is an adequate technique for calculating electromagnetic field effects in biological tissues. The FDTD method can be used for any type of source signal, meaning either a Gaussian pulse or sinusoidal signal. Using a gaussian pulse as a source signal, a wide frequency range can be solved with only one simulation. The ability to obtain wideband results using transient excitation is a significant advantage of time-domain based methods compared to frequency-domain based. In additon, data in the frequency-domain is easily obtained from results yielded in the time domain. Also, the advantage of a time based method is the ability to deal with nonlinear behaviour of the computational domain. The weaknesses of FDTD are related to its capabilities for modelling geometries of arbitrary shape. As discussed above, the rectangular lattice is not best suited for describing the shape of circular objects. Due to the simplicity of the method, the sources of errors in FDTD are well known, which enables strict influence on the simulation accuracy. Essentially, the accuracy of the method can be made as high as desired by reducing the cell size. Furthermore, there is basically no upper limit to the number of the field unknowns. Naturally, cell size and the amount of field unknowns have a direct impact on simulation time.

3 Specific absorption rate

In the past two decades the use of communication terminals such as cell phones and other electric devices operating in the radio frequency range has been rapidly increasing. Concerns about the human health effects exist because the antennas of small electric devices can deliver large amounts of radiation to very small and sensitive areas of the human body. Exposure to time-varying electromagnetic fields is used to measure the specific dosimetric[1] quantities that take account of different frequency ranges and waveforms. In the lower radio frequency range 100 kHz - 10 GHz specific absorption rate, SAR, is used. At even lower frequencies the current density is a more practical quantity. At high frequencies quantities like power density are applied. In this thesis the focus is on the frequency range 30 MHz - 6 GHz, hence the analysis concentrates mainly on SAR.

The specific absorption rate is used to measure the rate at which radiation power is absorbed by the unit mass of tissue. The concept of SAR evolved in the early 1970s and has become the basis of all the major RF exposure standards worldwide. The SAR value is expressed in units of watts per kilogram (W/kg) or in units of milliwatts per kilogram (mW/kg). The local SAR, defined as a power absorption in an infinite small tissue mass dP/dm, can be calculated from the root-mean-square value of electric field magnitude E_{rms} at a point within the tissue as

$$SAR = \frac{dP}{dm} = \frac{\sigma E_{rms}^2}{\rho} \tag{26}$$

where σ (S/m) is the conductivity and ρ (kg/m^3) is the density of the tissue at a particular point. Unlike an electric field, SAR is a scalar quantity. Generally, local SAR values are calculated as an average over a particular, usually 1g or 10g, mass.

The absorption of power into the lossy tissue appears as temperature rise dT. Thus, SAR can be also calculated as the rate of temperature rise at a given point within the tissue as

$$SAR = c_p \frac{dT}{dt} \tag{27}$$

where c_p is the speficic heat capacity (J/(kgK)) of the tissue and dT change of temperature during a period of dt. However, SAR calculation by temperature rise requires relatively high power to expose the tissue over a very short duration to avoid thermal diffusion errors. Therefore, electric field measurement is the regularly used method for evaluating low power transmitters for SAR.

3.1 Electromagnetic (EM) field absorption

The SAR is applicable to any tissue or organ of interest, where it is commonly evaluated as an average over a given mass. It can also be expressed as a whole-body average. The whole-body average is obtained by integrating the local SAR over the whole body. Since the RF energy induced in the body is scattered and absorbed at

[1]Dosimetry is the calculation of physical quantities of energy or substances that are imparted to an absorbing body.

various interfaces, the internal SAR distribution is usually highly inhomogeneous. The accuracy and reliability of a given SAR value is strongly dependent on the density and conductivity of the tissue. Among the parameters and the geometry of the tissue, the SAR distribution in a biological body exposed to an RF field depends on

- operational frequency, intensity and polarization of the incident wave
- orientation of the body relative to the source
- position, size, shape and posture of the body
- ground effects and reflector effects of other objects in the field near the exposed body.

[12],[13]

The incident wave is usually either E-, H-, or k- polarized depending on which component is parallel to the longest dimension of the object body. Studies have shown that under plane wave exposure conditions E-polarization yields the highest absorption, i.e. when the long axis of the body is parallel to the electric field vector. In addition, if the length of the body is half that of an incident wave, whole body resonance is obtained leading to more effective absorption. A "standard man", used by researchers, is considered to be 1.75 metres tall which makes him resonant at 86 MHz. Respectively, different size bodies absorb energy more efficiently at their resonant frequency. Absorption can be even higher if partial body resonances are considered. Unlike E-polarization, H-polarization does not yield a resonance peak, though at high frequencies absorption is similar to that of E-polarization. In k-polarization resonances are observed, although absorption is notable weaker than in E-polarization. Due to whole and partial body resonances, the high absorption in the human body can occur in the frequency range from about 30 MHz to 3 GHz. This frequency range is generally referred to as the resonance region.

A rough description of the penetration capabilities of EM fields into the human body can be obtained by considering the attenuation of the field as a function of frequency. The measure of how deep the EM field can penetrate into a material is called the penetration depth. It is the depth at which the electric field falls to 37 % and SAR to 13.7 % of the value it has at the surface. Depending on dielectric parameters, the EM field penetrates deeper into some tissues than others. However, as Figure 5 illustrates, the penetration depth in the muscle represents well the average biological tissue penetration depth.

Figure 6 presents the whole-body averaged SAR for various human models as a function of frequency. Below the frequency 30 MHz the wave length is large with respect to body length even inside the body and absorption decreases rapidly with decreasing frequency. Although, substantial absorption can take place in the neck and ankles. As discussed above, absorption is highest at the resonance region where the peak appears. At frequencies from 3 GHz to 300 GHz energy absorption occurs mainly at the surface layers of the body. The SAR on the surface can rise significantly with rising frequency. However, the thermoregulatory system of the skin is well adapted to the electromagnetic radiation induced surface heating.

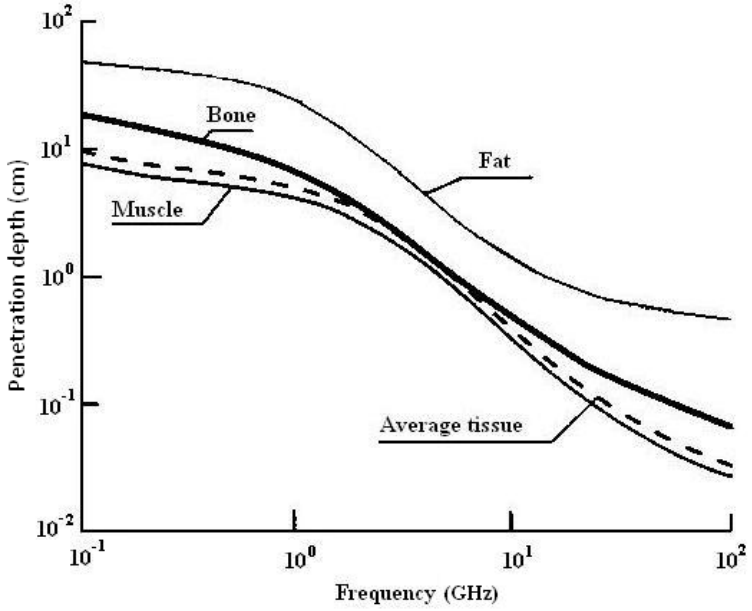

Figure 5: Penetration depths of EM field in different tissues [14].

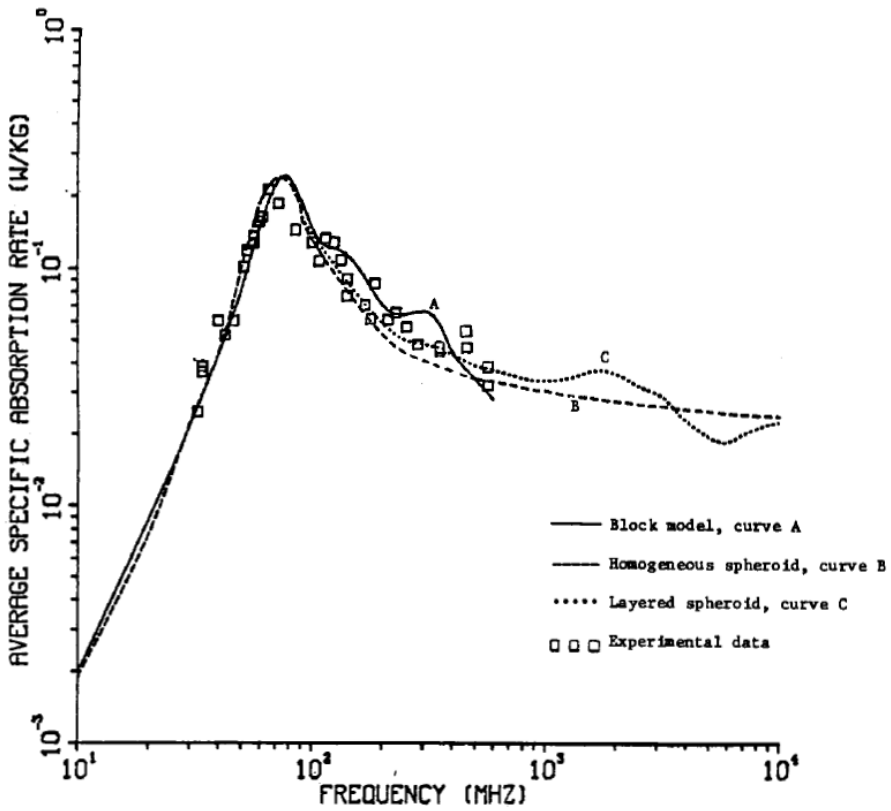

Figure 6: Whole-body averaged SAR for homogeneous and multilayered models of man for E-polarization [15].

3.2 Biophysical effects

The energies of the electromagnetic spectrum are propagated in the forms of waves which act as small bundles of energy called photons. The energy carried by a photon is directly proportional to the frequency f (Hz) of the specific electromagnetic radiation. It can be expressed as an equation

$$E = hf \tag{28}$$

where h is Planck's constant (6.63×10^{-34}) Js. The energy is measured in electron-volts (eV).

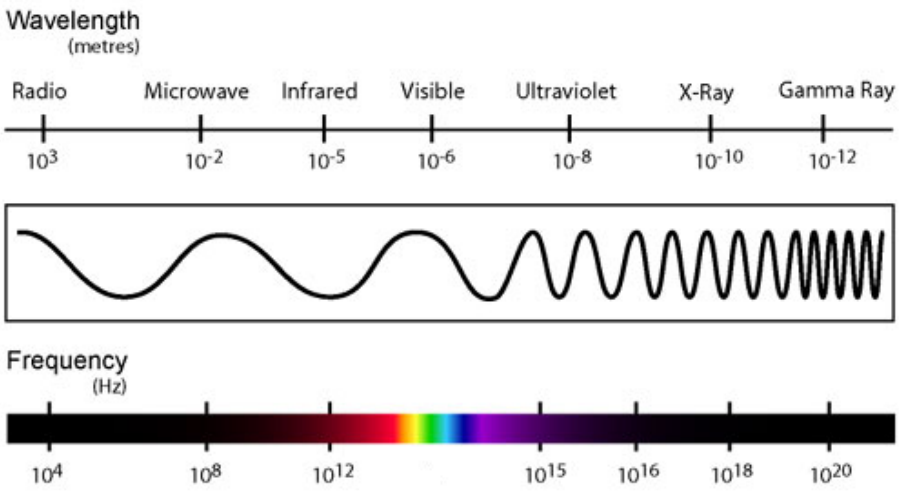

Figure 7: Electromagnetic spectrum.

The electromagnetic radiation is categorized as either non-ionizing or ionizing radiation. The ionizing radiation is energetic enough to dislodge orbital electrons and produce ion pairs, and it is associated with short and long term health effects. At high doses cell killing and, in extreme cases, death of the exposed individual may occur. Exposure at lower doses may result in damage to the genetic material and in an increase in the risk of cancer. The required energy of the radiation photon to produce ionization in living tissue is at minimum 12 eV [16]. Even though weak hydrogen bonds in macromolecules may involve ionization levels less than 12 eV, the radiation of energies below this limit is generally regarded non-ionizing. As Equation 28 indicates, the lower the frequency, the lower is the photon energy. Even at a frequency of 1 THz (10^{12} Hz) the energy is still only 4 meV. Thus, according to Figure 7 which illustrates the electromagnetic spectrum the radiation at radio frequencies is non-ionizing. This is mainly the reason for the widespread belief that radio waves cannot be a cause of cancer. However, while ionizing does not occur, the radio waves can still have harmful effects. The energy of the non-ionizing radiation absorbed into the molecule either has an effect on the energy levels of its atom, or changes the rotational, vibrational, and transitional energies of the

molecule [17]. Further, the impact on biological tissue is dependent upon the energy of the radiated photons, the penetration capabilities into the tissue of these photons and the chemical reaction proneness of the specific molecules when the energy is absorbed.

3.2.1 Thermal and non-thermal effects

Conventionally, biological effects induced by RF fields have been classified into thermal effects resulting from high-level RF power and non-thermal effects associated with low-level fields. Non-thermal effects generally relate to the effect at which the increase in temperature is barely observable. Although non-thermal effects have been detected, they have still remained somewhat ambiguous and without plausible evidence [18], [14]. At the moment, biological effects and health impairments of the low level RF fields are at the centre of the bioelectromagnetic research. On the other hand, thermal effects are widely known and understood. Numerous studies have shown that exposure to high-level RF fields, depending on exposure time and temperature, can result in disturbance in cell activity, exceeding of the thermoregulatory capabilities of the tissue and permanent destruction of tissues. Even death can result when heat is diffused from irradiated portion of the body to the rest of the body by the vascular system. The effects have been demonstrated on laboratory animals such as rats, rabbits and dogs.

The human body regulates temperature rises by activating cooling mechanisms in the tissues, mainly sweating and adjustments of blood circulation in the body surface. As the absorbed energy increases, the operation of the cooling mechanisms starts to break down, leading into an uncontrolled rise in body temperature. However, sensitivity among biological processes to temperature changes varies vastly. The threshold for a perception in temperature change is about 0.07 K, while necrosis (cell death) starts with a 5 K rise in body temperature. Some areas of the body, such as the eyes and the testes, are particularly vulnerable to RF heating because there is relatively little blood flow in them to provide sufficient cooling.

The SAR value cannot be directly interpreted as a temperature rise in biological tissue. Even when the characteristics associated with absorbed energy such as distribution and exposure time are known, the temperature patterns are further affected by the thermal properties of the tissues and the cooling effect of the blood circulation. Also, surrounding conditions have to be taken into account, e.g. temperature and moisture in air. Approximations of the local temperature rise are usually based on Penne's bioheat equation

$$\rho c_p = \frac{\delta T}{\delta t} = \Delta \times k \Delta T - c_b W_b (T - T_{art}) + \rho_{eff} SAR \tag{29}$$

where T (C) is tissue temperature rise, ρ_{eff} is the effective density (kg/m^3), c_p (Jkg^{-1}C^{-1}) is the specific heat capacity and k (W m^{-1}C^{-1}) is the tissue thermal conductivity. W_b is the blood perfusion, c_b (Jkg^{-1}C^{-1}) is the blood specific heat capacity and T_{art} is the the arterial inlet blood temperature. Blood perfusion refers to the process of nutritive delivery of arterial blood to the tissue. Penne's equation

basically describes temperature changes over a small volume element as a sum of entering and leaving heat energy.

As mentioned above, the distribution of the absorbed energy by a biological tissue is dependent on the dielectric properties of the tissue. Furthermore, the distribution is also non-uniform at the level of cells and molecules. The absorption is observed to be highest in tissues of high water content, i.e. high conductivity, such as muscle, brain tissue and skin. On the other hand, absorption is an order of magnitude lower in dry tissues such as bone and fat. The reflections of radio waves from interfaces between tissues of different conductivities can yield standing waves accompanied with absorption peaks. The SAR value at these "hot spots" can exceed significantly the mean SAR of the whole body. Severe skin burns over the rib cage of laboratory animals have been observed due to this effect when exposed to high level radio frequency fields. Local "hot spots" are also produced by various other methods, which are dependent on frequency and exposure situation, e.g. small radiation device such as mobile phone positioned in close proximity to the human body.

Regarding the thermal effect induced by radio waves, it is relevant to consider at which level the temperature rise starts to harm the biological tissues. Many studies have been conducted on laboratory animals in order to gain profound comprehension on the issue. Also, studies have been carried out on volunteer test persons and workers in thermally stressful environments. Tables 2 and 3 present some outcomes of these studies. Table 2 provides critical thresholds for different health effects as temperature levels, whereas Table 3 uses SAR values. When the temperature of a tissue has been over 41 °C for half an hour heath injuries start to occur. Respectively, the central nervous system starts to receive damage when the threshold of 42 - 44 °C is exceeded. Again, it is worth reminding that the temperature of the tissue cannot be directly derived from SAR due to active and passive heat regulation. Consequently, suggestions have been made that it would be more justifiable to base the exposure limitations on temperature rise rather than SAR.

Table 2: Temperature thresholds for harmful biological effects on humans and laboratory animals [14].

Effect	Object	Threshold (°C)	Exposure duration
Heatstroke	Human	> 42	1 - 2 h
Injury to the central nervous system	Human, mouse, rat, cat, dog	42 - 44	1 - 2 h
Skin burn	Human	55 - 60	3 - 10 s
Pain sensation	Human	45	3 - 10 s
Behavioural changes	Rat	1 °C (increase)	40 - 60 min
Cataracts	Rabbit	≥ 41	≥ 30 min

Thermoregulatory response studies performed on resting volunteers have demonstrated that 30 minutes of exposure to EMF, under conditions in which whole body

Table 3: SAR thresholds for harmful biological effects on laboratory animals [14].

Effect	Species	Frequency (MHz)	Threshold (W/kg)	Exposure duration
Death	Mouse	2450	42	4 h
	Rat	2450	18	4 h
	Mouse	7000	30	50 - 70 min
	Rat	7000	14	60 - 100 min
Damage to fetus	Rat	27, 12	11	3 min (42.2 °C)
Memory lapse	Rat	600	10	20 min
Reduction in fetal weight	Rat	970	4.8	22 h/day
	Rat	6000	7.3	102 h
Temporary infertility on males	Rat	2450	5.6	4 h/day, 5 day/week, 4 weeks

SAR was less than 4 W/kg, caused an increase in the whole body temperature of less than 1 °C. However, when 4 W/kg is exceeded, the increase in body temperature starts to have harmful, in some cases even dangerous, effects. The adverse effects typically appear as behavioural changes, performance reduction and fatigue. Long time exposure can cause failure of the thermoregulatory mechanisms, which may result in heatstroke and, eventually, death.

4 Radiation safety standards

Various international organisations have been engaged in formulating the RF safety standards for human beings, see Table 4. An international standard usually has no regulatory or mandatory status and it becomes binding only if officially adopted within a country. Safety standards are based on the results of critical analysis of the relevant scientific research including all laboratory and epidemiology research that relates to any biological response from short-term and long-term exposure. Following the analysis, a threshold SAR is then established for the most sensitive confirmed response that could be considered harmful to humans. To increase confidence that the standard is below the SAR level at which adverse effects could occur, the threshold is usually lowered 10 to 50 times below the observed threshold. Contemporary safety standards for exposure to radio frequency electromagnetic energy cover a frequency range from at least 3 kHz up to 300 GHz.

Table 4: International expert and standardization organizations.

Organization
ICNIRP - International Commision on Non-Ionizing Radiation
FCC - Federal Communications Commission
IEEE - The Institute of Electrical and Electronics Engineers
IEC - International Electrotechnical Commision
CENELEC - European Commitee for Electrotechnical Standardization
WHO - World Health Organization

The International Radiation Protection Association's (IRPA) International Commission on Non-Ionizing Radiation Protection (ICNIRP) publishes guidelines for exposure to RF/microwaves which are employed by EU countries and in many industrialized countries outside Europe. In the United States, the Federal Communications Commission (FCC) has adopted and used recognized safety guidelines for evaluating RF environmental exposure since 1985. The FCC guidelines for human exposure to RF fields were derived from the recommendations of two expert organizations, the National Council on Radiation Protection and Measurements (NCRP) and the Institute of Electrical and Electronics Engineers (IEEE). The guidelines recommended by IEEE are also applied in Canada. The IEEE safety limits are generally similar to those of the ICNIRP, with a few exceptions. In Russia and China similar norms are followed that were established in the former Soviet Union.

In most countries different standards have been defined for occupational and for general public exposures. Workers are assumed to be healthy adults, aware of the risks and exposed only during work periods. The exposure standards for workers are defined according to scientific research concerning biological effects and health risks, so that adverse effects are prevented. The general public on the other hand, contains the full spectrum of health sensitivities and is potentially exposed 24 hours per day unaware of the risks. Thus stricter safety precautions in general public

exposure limits are dictated. Commonly, the exposure limits for the general public are one fifth of those applied to workers. SAR limits for occupational and for general public exposures, issued by various international and national standard bodies and regulatory authorities, are presented in Tables 5 and 6.

Table 5: SAR limits for the occupational exposure.

Limit	ICNIRP [19]	IEEE, USA [20]	FCC, USA [21]
Status	Recommendation	National standard	National regulation
Year	1998	2006	1997
Whole-body SAR (W/kg)	0.4	0.4	0.4
Limbs SAR (W/kg)	20	20	20
Head and trunk SAR (W/kg)	10	8	8
Averaging time (min)	6	6	6
Averaging mass (g)	10	10	1 (head and trunk), 10 (limbs)
Frequency range of SAR assessment	100 kHz - 10 GHz	100 kHz - 3 GHz	100 kHz - 6GHz

The basic exposure limits have been given in terms of the whole body and local SAR below 10 GHz in the European standards, below 6 GHz in the FCC regulation and below 3 GHz in the IEEE standard. As discussed in the previous chapter, repeated experiments resulted in an average value of 4 W/kg for the whole body to be the threshold level at which harmful biological effects may occur. The requisition is that a temperature rise of one degree is not exceeded. In the workplace or controlled environments a safety factor of 10 is included for exposure. Respectively, for the general public in an uncontrolled environment the SAR value is reduced by a factor of 50. Since the SAR distribution inside the human body varies from point to point, different exposure limits are defined for devices that expose only part of the body, such as mobile phones. According to ICNIRP guidelines the maximum local SAR is 2 W/kg averaged in a tissue element having a mass of 10 g. However, the FCC regulation limits maximum permissible localized exposures of smaller regions in the human body to 1.6 W/kg in any 1 g of tissue which corresponds roughly to 0.8 W/kg averaged over 10 g at 900 MHz.

At frequencies of 10 - 300 GHz the specific absorption rate is no longer a valid exposure quantity since absorption takes place mainly at the surface. At this region power density is used both for the definition of basic restrictions and derived reference levels. The limits are 50 W/m^2 for workers and 10 W/m^2 for the general

public, see Table 7.

Table 6: SAR limits for the general public exposure.

Limit	ICNRP [19]	IEEE, USA [20]	FCC, USA [21]
Status	Recommendation	National standard	National regulation
Year	1998	2006	1997
Whole-body SAR (W/kg)	0.08	0.08	0.08
Limbs SAR (W/kg)	4	4	4
Head and trunk SAR (W/kg)	2	2	1.6
Averaging time (min)	6	6	30
Averaging mass (g)	10	10	1 (head and trunk), 10 (limbs)
Frequency range of SAR assessment	100 kHz - 10 GHz	100 kHz - 3 GHz	100 kHz - 6GHz

Table 7: Basic restrictions for power density of EM radiation at frequencies 10 - 300 GHz (ICNIRP 1998).

Exposure	Power density (W/m^2)
Occupational	50
Public	10

4.1 IEC 62209 Part 2

The IEC international standard under development IEC 62209 Part 2: "Evaluation of the Human Exposure to Radio Fields from Hand-Held and Body-Mounted Wireless Communication Devices in the Frequency range 30 MHz to 6 GHz (Human Models, Instrumentation, Procedures)," has the objective of measuring the human exposure from devices capable of transmitting electromagnetic fields intended to be used in a position near the human body. The standard applies for radio frequency exposure in the frequency range of 30 MHz to 6 GHz to any wireless communication device with the radiating parts of the device at distances up to 200 mm from the body, i.e. when held in the hand or in front of the face, mounted on the body, combined with other transmitting or non-transmitting devices or accessories garments. The respective sections of the standard provide definitions and evaluation for the following general categories of device types: body-mounted, body-supported, desktop, front-of-face, hand-held, laptop, limb-mounted, multi-band, push-to-talk, clothing-integrated. These types of devices include but are not limited to mobile-phones, cordless microphones, auxiliary broadcast devices and radio transmitters in personal computers. The standard gives guidelines for a reproducible measurement methodology for determining the compliance of wireless devices with the SAR limits. For transmitters used in close proximity to the human ear, the procedures defined in IEC 62209 Part 1 apply.

5 Phantoms

In order to estimate the risk of irradiation to a person or population, it is necessary to know the respective doses in the body. The amount of absorbed radiation can be measured experimentally or analytically by employing a representation of the human body, the so called phantom. The experimental approach is regarded as burdensome and difficult process whilst the mathematical modelling of an exposure scenario has been proved to be an extremely flexible and efficient method.

This chapter provides an historical overview and general information regarding phantoms used in computer simulations. Additionally, the phantom projects Visible Human, the first phantom to represent complete human anatomy, and The Virtual Family, a family of phantoms whose one member was utilized in this study, are introduced at the end of this chapter

The purpose of phantoms is to simulate anatomical and electrical properties of the human body. They have been used in dosimetry calculations for radiography, radiotherapy, nuclear medicine, radiation protection and to investigate the effects of low frequency electromagnetic fields [25]. Earlier, when computational resources were meagre, studies of energy absorption evaluations were performed on simple, spherical and cylindrical models of humans that could be solved by analytical methods. Eventually, this procedure was followed by analyses of the exposure of prolate spheroidal models and block models of the body. Recently, the advancement of medical imaging techniques, especially computed tomography (CT) and magnetic resonance imaging (MRI), has allowed the construction of high resolution three-dimensional computational models of the actual anatomy of individual humans.

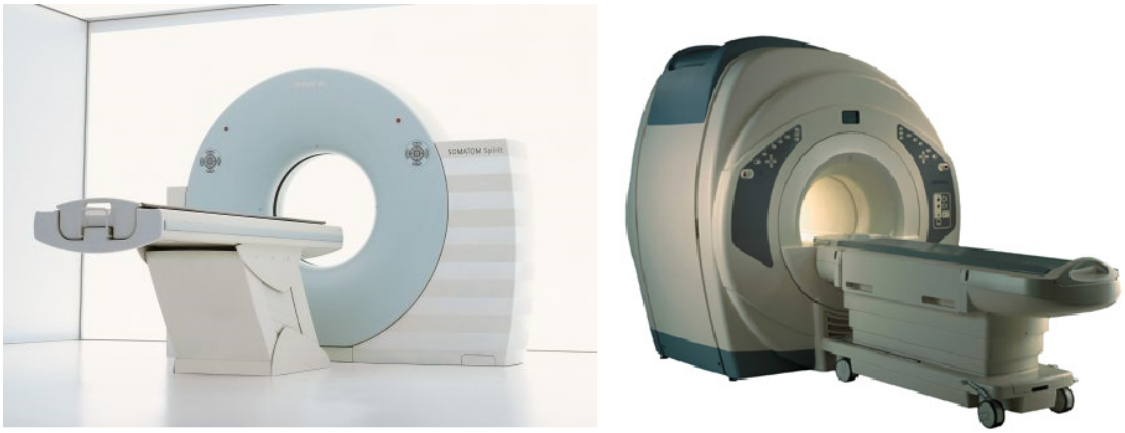

Figure 8: CT (left) and MRI (right) scanners [22].

Though it is neither always necessary nor practical for the phantoms to emulate the anatomical details, it is important to define the relevant features, dimensions and material properties that affect SAR measurement. The statistical breakdown of anatomical shapes and sizes can be acquired from studies of the human population to guide the specification of a realistic phantom shape. The main parameters for phantoms are the mass and position of organs as well as their shape and the shape of the body. Also, the solid representation of organ interfaces and thin tissue structures

is a prominent requirement in order to correctly render reflections, interference and hot spots at tissue boundaries.

The first complex phantom which contained organs described by mathematical expressions was devised about forty years ago for the use of the Medical Internal Radiation Dose (MIRD) Committee of the Society of Nuclear Medicine [26]. This so-called MIRD phantom was based on the concept of a reference man, a person with the anatomical and physiological properties defined in the ICRP Publication 23 [27]. The phantom consists of three types of tissues: lung, skeletal tissue and soft tissue. Eventually MIRD phantoms representing both genders at various ages were developed in order to provide more accurate statistical representation of the population. Although having a large number of organs and their respective masses in accordance with the ICRP data on reference man, MIRD models are unrealistic regarding organ shape and location. The internal disposition of organs of the MIRD phantom Adam is shown in Figure 9.

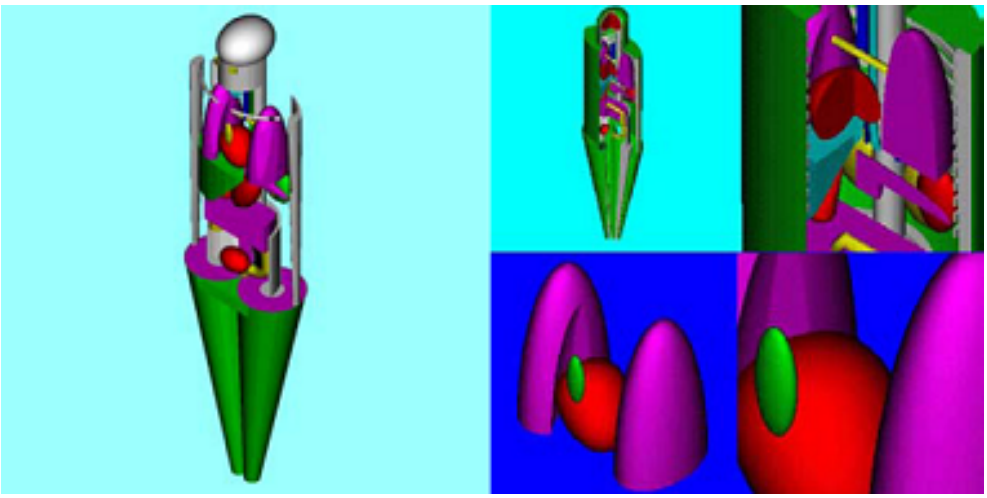

Figure 9: The adult human phantom ADAM [23].

As the human anatomy was too complex to be realistically modelled with a limited set of simple surface equations, it was not until the advent of advanced medical imaging and computing technologies (MRI, CT) when the development of more complex voxel models became possible. Magnetic resonance imaging and computed tomography have since became widely used methods in the medical field to obtain topographic images of patients' internal structures for diagnoses of defects in soft tissues such as ligaments, muscles and brain tissues. The image sets of most anatomically realistic body phantoms have been typically segmented using cubical voxels over the entire body region with resolution usually corresponding to the pixel size of the original set of images. The resolution ranges from about 0.5 mm $\times$ 0.5 mm $\times$ 1.0 mm for phantoms of newborn children to more than 5 mm in case of some adult phantoms.

One of the first anatomically realistic voxel phantoms was the NORMAN model based on MRI scans of a single subject and scaled to the height and mass of the reference man. The MRI images were taken at 10 mm intervals with 2 mm $\times$ 2

mm resolution and voxels were segmented to 38 tissue types. The model was used to estimate organ doses from both external and internal photon sources. A model called VIPMAN was developed based on the colour images of the Visible Human Project (see 5.1), see Figure 10. The image resolution was 0.33 mm $\times$ 0.33 mm and the slice thickness 1 mm. Several other models have been also generated based on the same data [28].

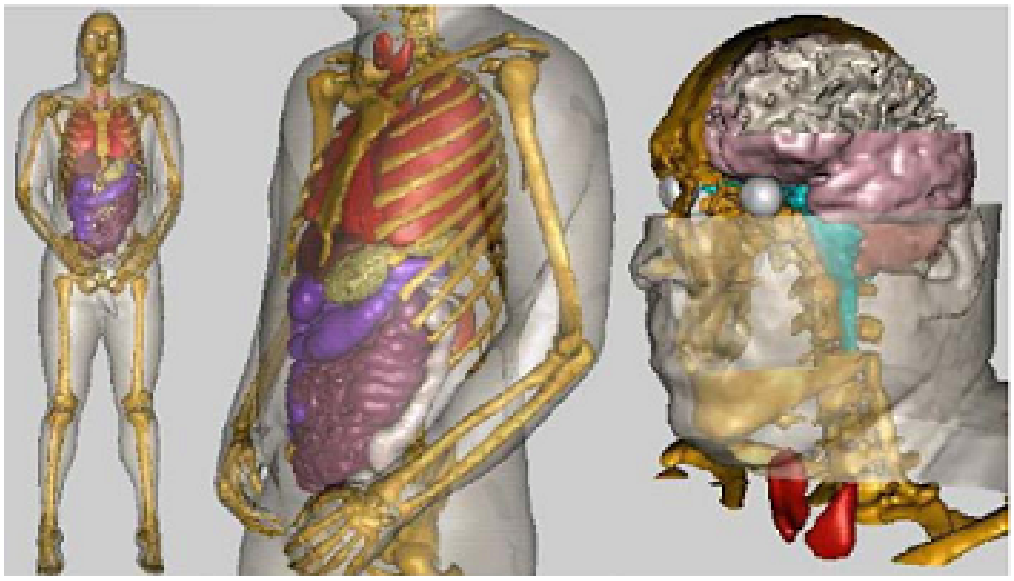

Figure 10: The VIPMAN developed from the photographic images of the Visual Human Project [23].

A well known GSF (National Research Centre for Environment and Health in Germany) phantom called Golem was developed from CT images of 2.08 mm $\times$ 32.08 mm resolution and 8 mm slice thickness representing 121 different types of tissues or organs, see Figure 11. The realism of the organ shape is demonstrated in Figure 12 where a CT slice of Golem and a cross section of Adam are shown alongside.

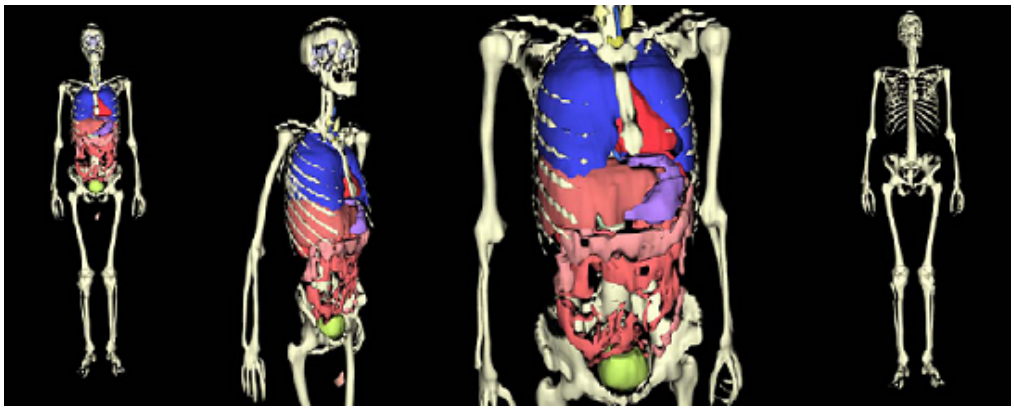

Figure 11: Golem voxel phantom [23].

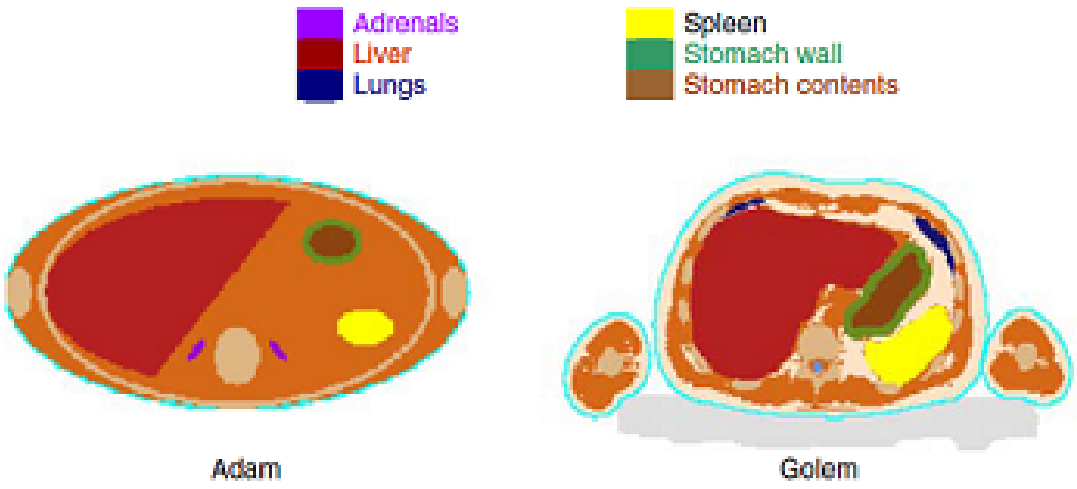

Figure 12: Comparison of an axial slice of the voxel phantom Golem (right) with the corresponding one of the mathematical phantom Adam (left) [24].

Even though the development of anatomically realistic phantoms of the human body for electromagnetic field dosimetry has mostly concentrated on male subjects, several models of females have been also developed. The voxel phantom family of GSF contains three female models, Helga, Donna and Irene, which are shown in Figure 13.

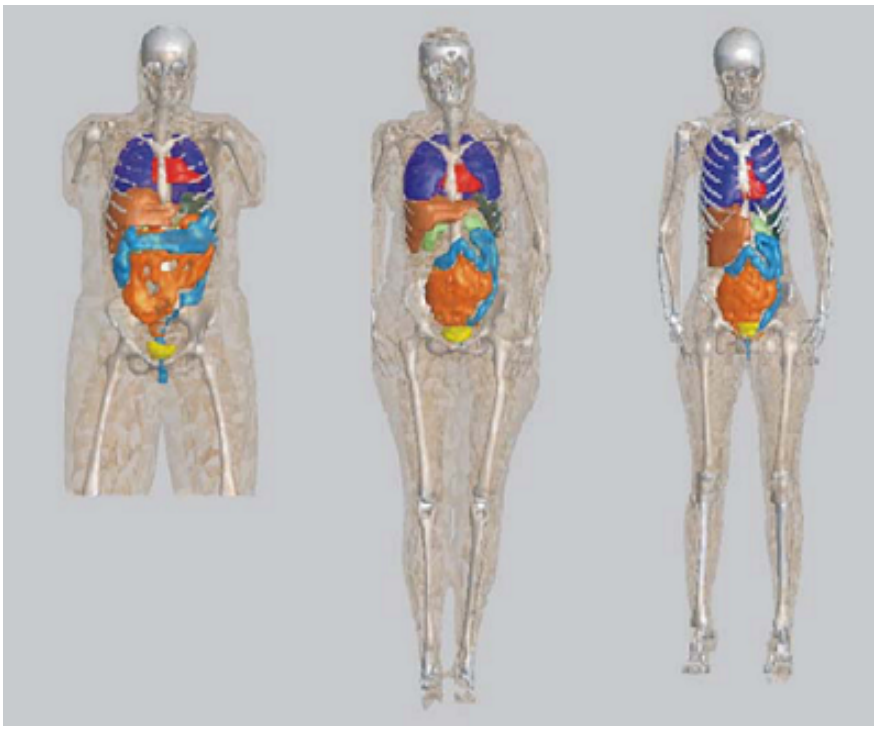

Figure 13: The three female phantoms of GSF: Helga, Donna and Irene [23].

One useful characteristic of the voxel phantoms is the possibility to vary their size and thereby simulate a larger or smaller individual. Because of the limited availability of whole body phantoms of children, adult phantoms were often scaled to the anatomical dimensions of children. However, phantoms of children have been also generated from authentic child models. Figure 14 displays the GSF Baby and Child phantoms developed from a cadaver of a dead baby and a body of a leukemia patient who was receiving a whole-body irradiation treatment. In conclusion, a list of popular whole or partial body phantoms is provided in Table 8.

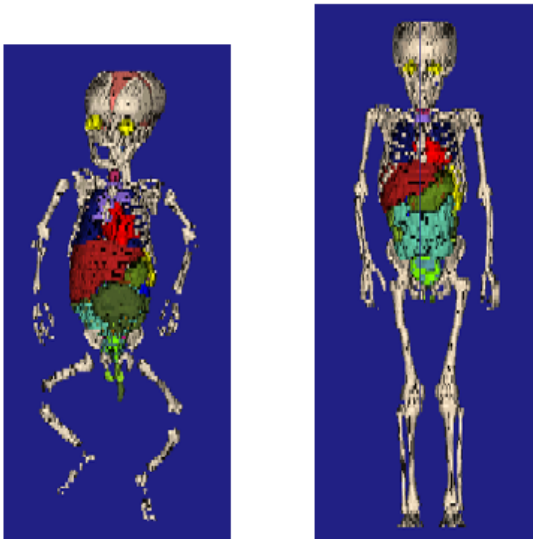

Figure 14: Three-dimensional reconstruction of some organs of the paediatric voxel phantoms Baby (left) and Child (right) [24].

Table 8: Existing whole or partial body phantoms.

Phantom	Images	Age and sex	Comment
Child [29]	CT	7-year-old female	Small for age (5 to 7-year-old)
Baby [29]	CT	8-week-old female	
VoxelMan [30]	CT	Adult male	Head and torso
NORMAN [31]	MRI	Adult male	Only ten ribs
Golem [32]	CT	38-year-old male	
ADELAIDE [33]	CT	14-year-old female	Torso
Otoko [34]	CT	Adult male	
UF newborn [35]	CT	6-day-old female	
UF 2 month [35]	CT	2-month-old male	Small for age
UF Series B 9-month [36]	CT	9-month-old male	Extension to the UF Series A phantoms by inclusion of arms and legs and resizing of some organs
UF B 4-year [36]	CT	4-year-old female	
UF B 8-year [36]	CT	8-year-old female	
UF B 11-year [36]	CT	11-year-old	
UF B 14-year [36]	CT	14-year-old	
Visible-human [37]	CT, MRI	38-year-old male	
Frank [24]	CT	48-year-old male	Head and torso
Donna [24]	CT	40-year-old female	
Helga [24]	CT	26-year-old female	Legs absent below mid-thigh
Irene [38]	CT	32-year-old female	
Nagaoka man [39]	MRI	22-year-old male	
Nagaoka woman [39]	MRI	22-year-old female	
KR-man [40]	MRI	28-year-old male	
Pregnant woman [41]	CT	30 weeks pregnant	Part torso
NAOMI [42]	MRI	23-year-old female	
Ella [43]	MRI	26-year-old female	
Duke [43]	MRI	34-year-old male	
Billie [43]	MRI	11-year-old female	
Thelonious [43]	MRI	6-year-old male	
Louis [44]	MRI	14-year-old male	
Eartha [44]	MRI	8-year-old female	
Dizzie [44]	MRI	8-year-old male	
Roberta [44]	MRI	5-year-old female	

5.1 Visible Human

The Visible Human Project (VHP) was the first extensive research to build a digital image library of volumetric data representing complete, normal adult male and female anatomy. The project was established by the U.S. National Library of Medicine in 1989 and the initial aim was the acquisition of transverse Magnetic Resonance Interferometry (MRI), Computerized Tomography (CT) and cryosection images of a representative male and female cadaver at an average of one millimeter intervals, as shown in Figure 15. The donors for the cadavers were a 39-year-old convicted murderer executed by the state of Texas in 1993 and an anonymous 59-year-old Maryland woman. Visible Human models are used by doctors to plan surgeries, and their anatomy is being studied by medical students. Additionally, automobile manufacturers now include passenger injury models based on Visible Human data in their vehicle crash simulation models [37].

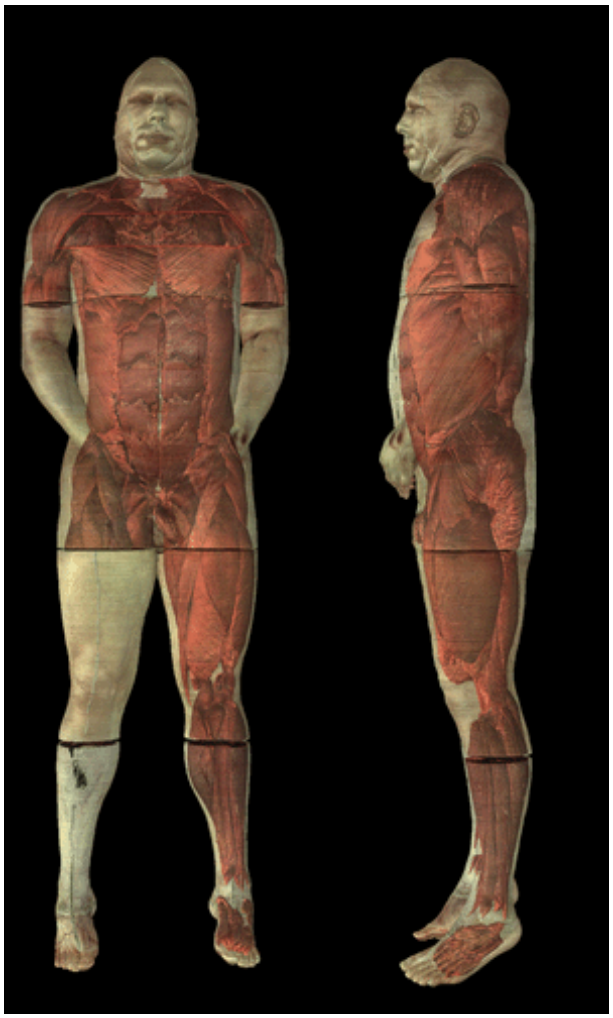

Figure 15: Visible Human male [46].

The Visible Human Male data set consisting of MRI, CT and anatomical images was released in November, 1994. Axial MRI images of the head and neck, and

longitudinal sections of the rest of the body were taken at 4 mm intervals. The MRI images are 256 by 256 pixel resolution with each pixel made up of 12 bits of gray tone. The CT data consist of axial CT scans of the entire body taken at 1 mm intervals at a pixel resolution of 512 by 512 with each pixel made up of 12 bits of gray tone. The approximately 7.5 megabyte axial anatomical images at 1 mm intervals are 2048 pixels by 1216 pixels, with each pixel being 0.33 mm in size, and defined by 24 bits of colour. There are 1871 cross-sections for both CT and anatomical images. The heterogeneous model has more than 40 different tissues and is available in 6, 3 and 1 mm voxel sizes. [45]

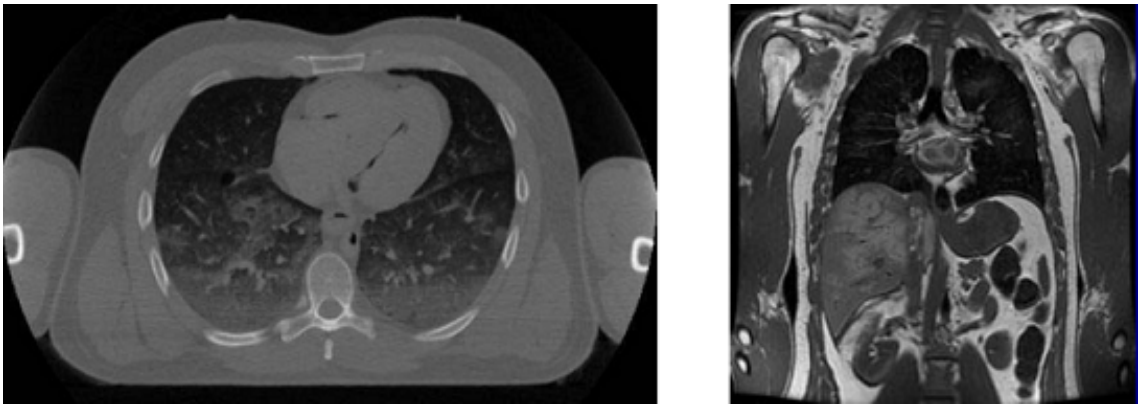

Figure 16: On the right a CT image of thorax and on the left an MRI scan of the abdomen of the Visible Human male [45].

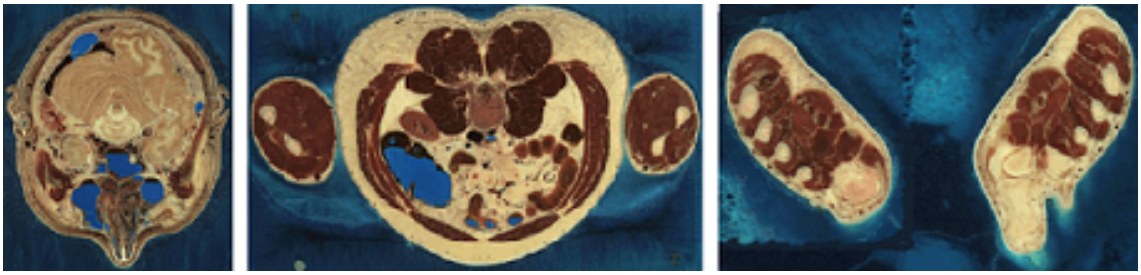

Figure 17: Cryosections of the Visible Human male. From left to right: head, thorax and feet [45].

The Visible Human female data set having the same characteristics as the The Visible Human male was released in November, 1995. However, the axial anatomical images were obtained at 0.33 mm intervals. Spacing in the "Z" dimension was reduced to 0.33 mm in order to match the 0.33 mm pixel sizing in the "X-Y" plane. As a result, developers interested in three-dimensional reconstructions are able to work with cubic voxels. There are 5189 anatomical images in the Visible Human female data set. [45]

5.2 Virtual Family

The Virtual Family project was a development of anatomically correct whole body human models of an adult male (34 years old), an adult female (26 years old) and two children (an 11-year-old girl and a six-year-old boy) for the optimized evaluation of electromagnetic exposure [43], see Figures 18 and 19. The models were developed based on high resolution MRI image sets of whole body scans of four healthy volunteers. Sizes and body masses of the adult models were chosen according to worldwide averages of height and body mass index (BMI) and German statistics were considered for the children. More than 80 different tissues and organs in the MR images were identified by an expert team of biologists and physicians. All tissues and organs were reconstructed as three-dimensional unstructured triangulated surface objects, resulting in high precision images of individual features of the body. All four models are freely available to the scientific community for research purposes. The Virtual Family models are being widely applied in studies on electromagnetic exposure, device optimization and medical applications.

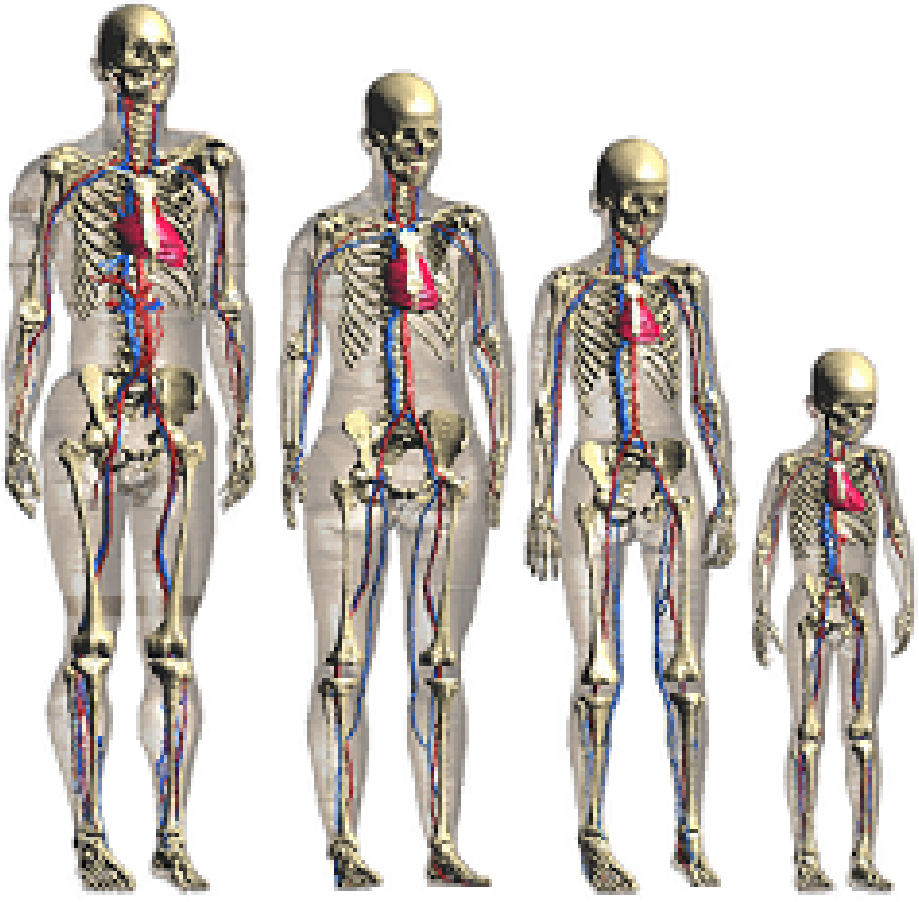

Figure 18: Whole-body human models of the Virtual Family: Duke, Ella, Billie, Thelonious (from left to right) [44].

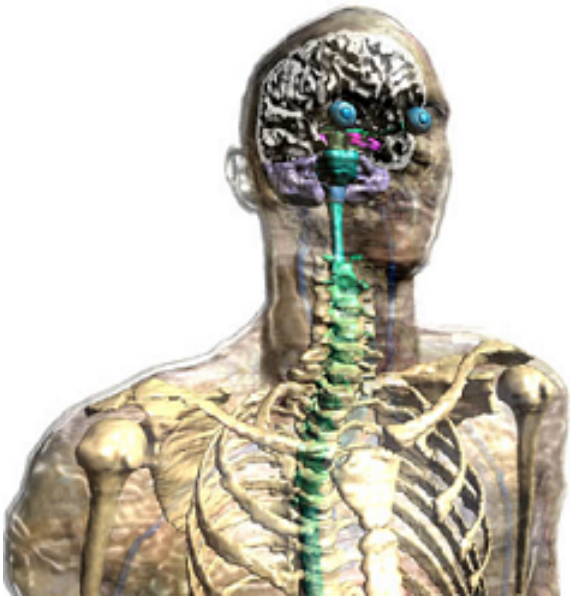

Figure 19: Duke - phantom of a 34-year-old male [44].

The 34-year-old male phantom Duke from Virtual Family, shown in Figure 19, was employed in this study. The phantom is comprised of 77 tissues, that is, skin, bone, muscle, fat, nerve, blood, white matter, gray matter, cerebellum, and so forth. It is 1.74 m tall and weighs 70 kg. As explained previously, the dielectric properties of the tissues, i.e. permittivity ϵ and conductivity σ, are dependent on frequency, which has to be taken into account especially at high frequencies. The frequency dependence of some typical human tissues is demonstrated in Table 9. A calculator for deriving dielectric parameters for tissues at specific frequencies provided in the website of Italian National Research Council was used to obtain these values [47].

Table 9: Dielectric parameters for some human tissues at different frequencies.

	Permittivity			Conductivity S/m		
Tissue	450 MHz	1800 MHz	5800 MHz	450 MHz	1800 MHz	5800 MHz
Muscle	56.75	53.54	48.48	0.80	1.34	4.96
Blood	63.67	59.37	52.53	1.36	2.043	6.50
Skin (dry)	45.75	38.87	35.11	0.70	1.18	3.71
Fat	5.56	5.34	4.95	0.04	0.07	0.29
White brain matter	41.4	37.01	32.62	0.45	0.91	3.49
Grey brain matter	56.55	50.07	44.00	0.75	1.39	4.98
Nerve	34.88	30.86	27.21	0.45	0.84	2.94

5.3 Flat phantom

A flat phantom is a simple flat-bottomed structure for which the SAR can easily be measured and calculated. It consists of a thin dielectric shell which is filled with a liquid simulating the dielectric characteristics of the human body. Typically, flat phantoms are about the size of a human torso. An advantage of a flat-bottomed phantom is that it provides maximal surface area contact with the device under test (DUT) and therefore generally estimates well SAR in a real person. In addition, a flat-bottomed phantom can be utilized for devices of various sizes. The SAR compliance evaluation for devices intended to operate close to body conditions, such as shoulder, waist or chest worn transmitters, is typically done with a flat phantom.

The shape of the phantom defined in IEC 62209 Part 2 is an ellipse with length 600 mm, width 400 mm and thickness of wall of the phantom 2 mm as illustrated in Figures 20 and 21. The phantom shell is made of low loss and low permittivity material, i.e. σ =5 S/m and ϵ =0.0016.

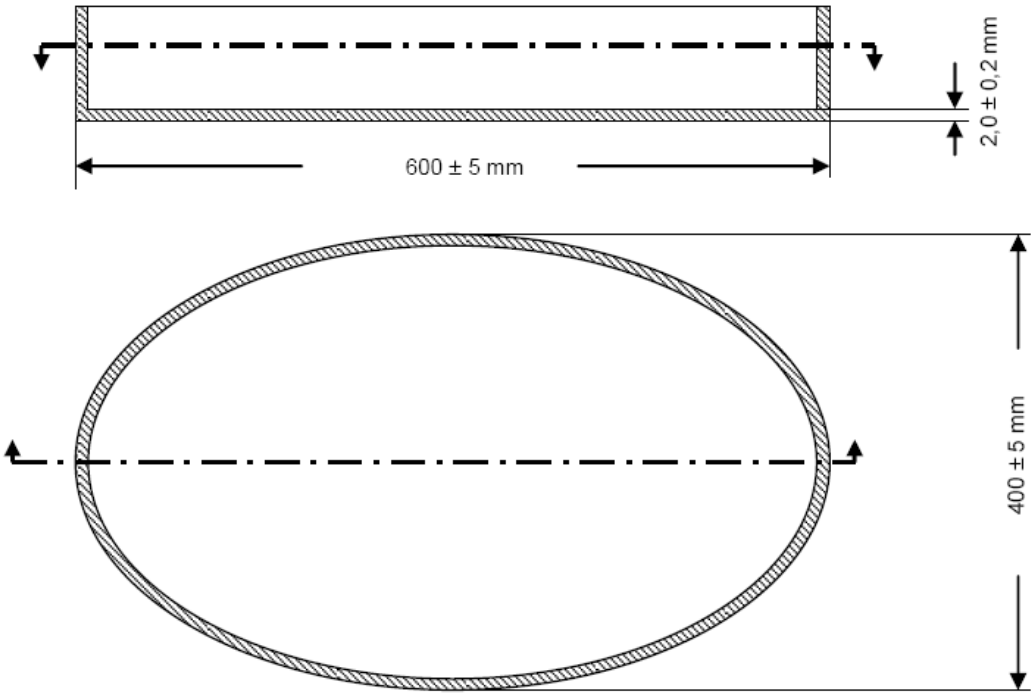

Figure 20: Dimensions of the elliptical phantom.

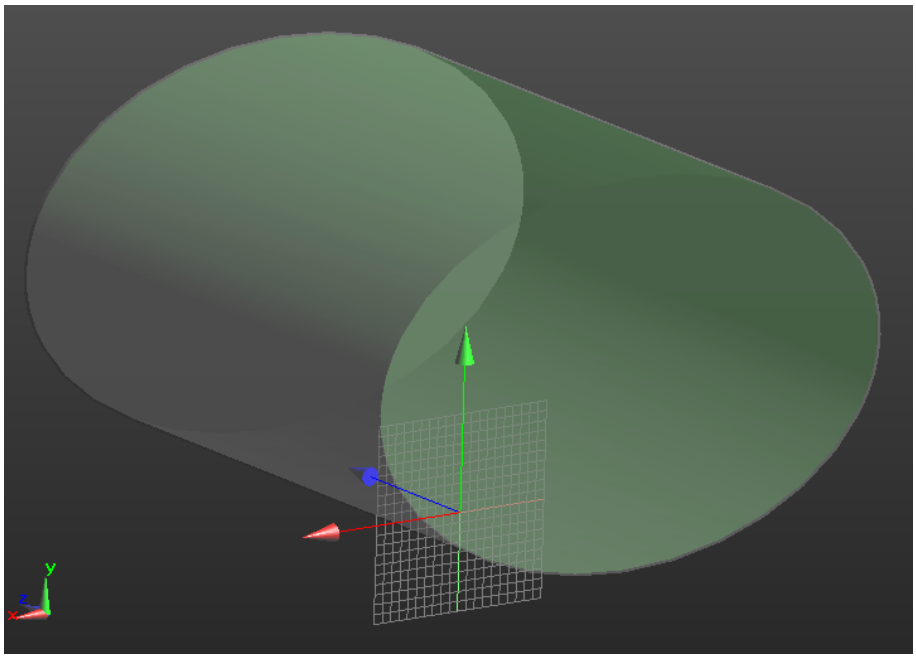

Figure 21: Elliptical phantom.

5.3.1 Tissue simulant liquids

The dielectric properties of tissues have been comprehensively studied during the past several decades. Tissue dielectric parameters depend on frequency, i.e. permittivities decrease and conductivities increase with frequency. Slight differences in published values for tissue dielectric properties exists, which is mainly due to different measurement methods, tissue temperatures, tissue aging effects, etc.

The choice of tissue dielectric parameters for homogeneous tissue-equivalent liquid determines the extent of any over- or underestimation when compared with SAR results from heterogeneous modelling. The detailed structure of internal body anatomies must be taken into account when selecting the equivalent tissue parameters. Additonally, these parameters must be chosen carefully in order to ensure that the SAR measured in the homogeneous phantom does not underestimate what is expected in an actual human body. The tissue simulant liquids are assumed to have a density of 1 000 kg/m^3.

The values for dieletrcic parameters of the tissue simulant liquids for head SAR measurements were derived for 10 frequencies in the frequency range of 300 MHz to 3000 MHz using an analytical model of an infinite half-space of layered tissues exposed to a plane wave. In order to obtain a feasible representation of the general public, the tissue layers were varied in composition and thickness to cover the anatomical variation of the exposed head region. Based on the worst case tissue layer compositions of the head with respect to absorption at each frequency, head tissue simulant liquid dielectric parameters for homogeneous modelling were derived resulting in the same or slightly higher spatial peak absorption [48]. It is believed that at close distances, a conservative exposure estimate for the body can

be achieved using the parameters for head tissue-equivalent liquids defined in IEC 62209 Part 1. Therefore, the head parameters are employed for the measurements of hand-held and body-mounted devices. The permittivity and conductivity of the liquid at frequencies of interest are presented in Table 10.

Table 10: Dielectric properties of the head tissue simulant liquid material (IEC).

Frequency MHz	Real part of complex permittivity, ϵ'_r	Conductivity, σ S/m
30	55.0	0.75
150	52.3	0.76
450	43.5	0.87
900	41.5	0.97
1450	40.5	1.2
1800	40.0	1.4
2450	39.2	1.8
3500	37.9	2.91
5800	35.1	5.48

The tissue simulant electrical parameters recommended by FCC are based on average electrical parameters for human muscle. However, conductivity has been increased some 10 % assuming worst-case absorption due to high losses. The dielectric properties at frequencies of interest are shown in Table 11.

Table 11: Dielectric properties of the human muscle simulant liquid material (FCC).

Frequency MHz	Real part of complex permittivity, ϵ'_r	Conductivity, σ S/m
30	91.8	0.72
150	61.9	0.80
450	56.7	0.94
900	55.0	1.05
1450	54.0	1.3
1800	53.3	1.52
2450	52.7	1.95
3500	51.4	2.82
5800	48.2	6.0

6 Simulation methods

The purpose of the simulations is to evaluate the usability of the tissue simulant liquids proposed by IEC and FCC in radiation measurements of body worn devices . The liquids are considered representative when the SAR values measured in the liquids contained within a flat phantom slightly overestimate the SAR values measured in anatomically realistic human phantoms. Body worn devices operate at different frequencies and can have arbitrary locations on the body resulting in a number of different exposure scenarios. A typical example of a body worn device is a mobile phone, wireless enabled PDA or other battery operated wireless device with the ability to transmit while mounted on a person's body.

6.1 Frequencies and sources

The considered frequencies were limited to the frequencies of those devices between 30 MHz and 6000 MHz that are technically in use. Mobile phones typically operate at GSM frequencies near 900 and 1800 MHz or at the UMTS frequencies up to 2100 MHz. Wireless Fidelity (WiFi) based communication devices, such as laptops, employ a frequency range around 2450 MHz. The radio frequency identification (RFID) devices expose at a frequencies up to 6000 MHz. Hence, the following frequencies were chosen in the simulations: 30, 150, 450, 900, 1450, 1800, 2450, 3500 and 5800 MHz.

Typically, flat phantoms are irradiated using a standard source, e.g. half-wave dipole, patch antenna or open-ended waveguide. In this study half-wave dipoles were chosen as radiators and were designed for each frequency according to the protocol in IEC-62209 Part 2 Annex B, see Figure 22. A dipole antenna has an easy structure and consists normally of just two metal wires with a specified length and a power source, i.e. feed point. As the name indicates, a half-wave dipole has a total length of a half the wavelength. The feed point is located between the two metal wires. When a sinusoidal power source is employed the voltage reaches its minimum and maximum at the different ends of the dipole, hence maximum current is obtained between the metal wires peaking at the feed point. The dimensions of the dipoles at the frequencies of interest described in the aforementioned IEC document are presented in Table 12. As one can notice, the lengths of the half-wave dipoles deviate slightly from a half of the wavelength. This has to do with the actual measurement situation where the lengths of the dipoles are optimized by taking into account the effect of the surroundings located in close proximity to the dipole. In other words, the wavelength is shorter in dielectric material than in free space, hence the shorter dipole.

The locations of the radiators were selected according to common locations of body worn devices. A total of six locations included two waist positions, two chest positions, shoulder and thigh. In addition, simulations were conducted with a dipole antenna tilted 90 degrees from its original position in order to gain more information on field distribution. Because the distance from the body varies for different body worn devices, it was necessary to vary the distance for the dipole antennas

accordingly. However, due to an already large number of variables, i.e. locations and frequencies, the dipoles were simulated only for the following four distances: 5, 10, 25 and 50 mm. The distances were measured from the dipole axis.

Table 12: Dimensions of the dipoles.

Frequency MHz	L mm	d mm
30	4400	3.6
150	940	3.6
450	290	3.6
900	149.0	3.6
1450	89.1	3.6
1800	72.0	3.6
2450	51.5	3.6
3500	37.0	3.6
5800	20.6	3.6

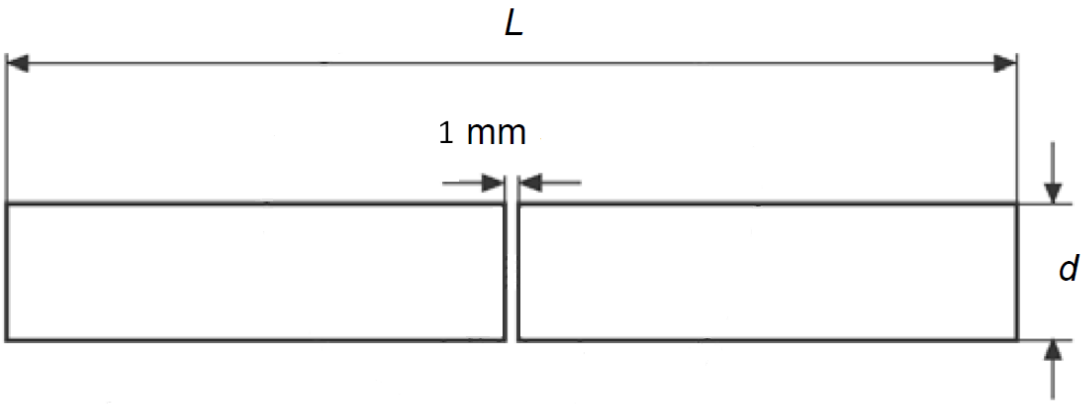

Figure 22: A half-wave dipole.

6.2 Simulation platfrom

An FDTD based SEMCAD X simulation platform was used to conduct this study. All simulations were done with graded meshes. The mesh resolution was highest near the feed point and lowest at the corners of the computational domain. The verification of the at-least-10-cells-per-wavelength rule in the tissue of the highest permittivity was crucial especially at high frequencies in order to ensure sufficient accuracy of the FDTD method. At lower frequencies the mesh cell size was adjusted so that an adequate representation of the model geometry was obtained. At high frequencies it was practical to exclude the parts of the body not included in the exposure to reduce the mesh cell size and, respectively, the simulation time. However, it was not necessary to actually delete parts of the model as SEMCAD allows to truncate the extremities of the model using the UPML boundaries. By default, the grid extends $\lambda/4$ wavelengths from the extremities of the model. However, manual settings permit the decreasing of the grid region by applying "negative" padding between the model and the UPML boundaries. The truncation of the unnecessary region of the model when it is irradiated in close proximity of the right side of the chest at 900 and 5800 MHz using UPML boundaries is shown in Figures 23 and 24.

The feed point source was a 1 V voltage source and the reference impedance was set to 50 Ω. The feed point impedance depends on the body model next to the dipole antenna and on the orientation of the antenna. In order to compare the results from different body models to results obtained from the flat phantom the calculated SAR needs to be normalized. In this study, the normalization was done to 1 W net input power. The SAR extraction algorithm in SEMCAD follows the recommendations of the IEEE Standard C95.3-2002, hence the averaging is done over a cube containing the respective mass of 1 or 10 g. SEMCAD provides three different implementations of the IEEE standard for SAR averaging named as Peak Spatial Average SAR (Fast), Spatial Average SAR Distribution and Spatial Average SAR Distribution with averaging information. The Peak Spatial Average method was used in this study as it was the fastest and recommended for situations where large or high resolution volumes must be evaluated [49].

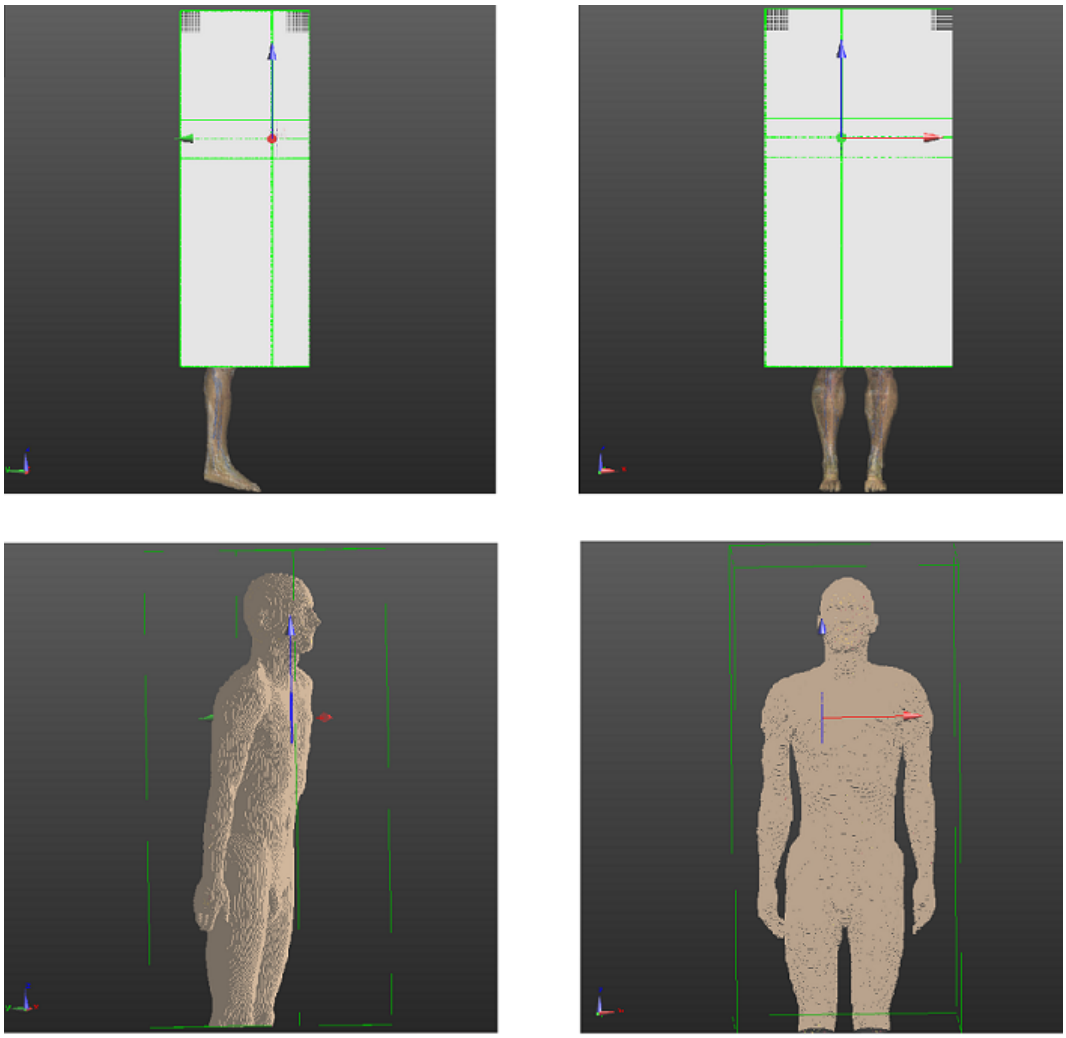

Figure 23: Above is the FDTD grid at 900 MHz from front and right. Everything that is not contained within the grid is ignored. Below is the truncated and voxelized model ready for the simulation.

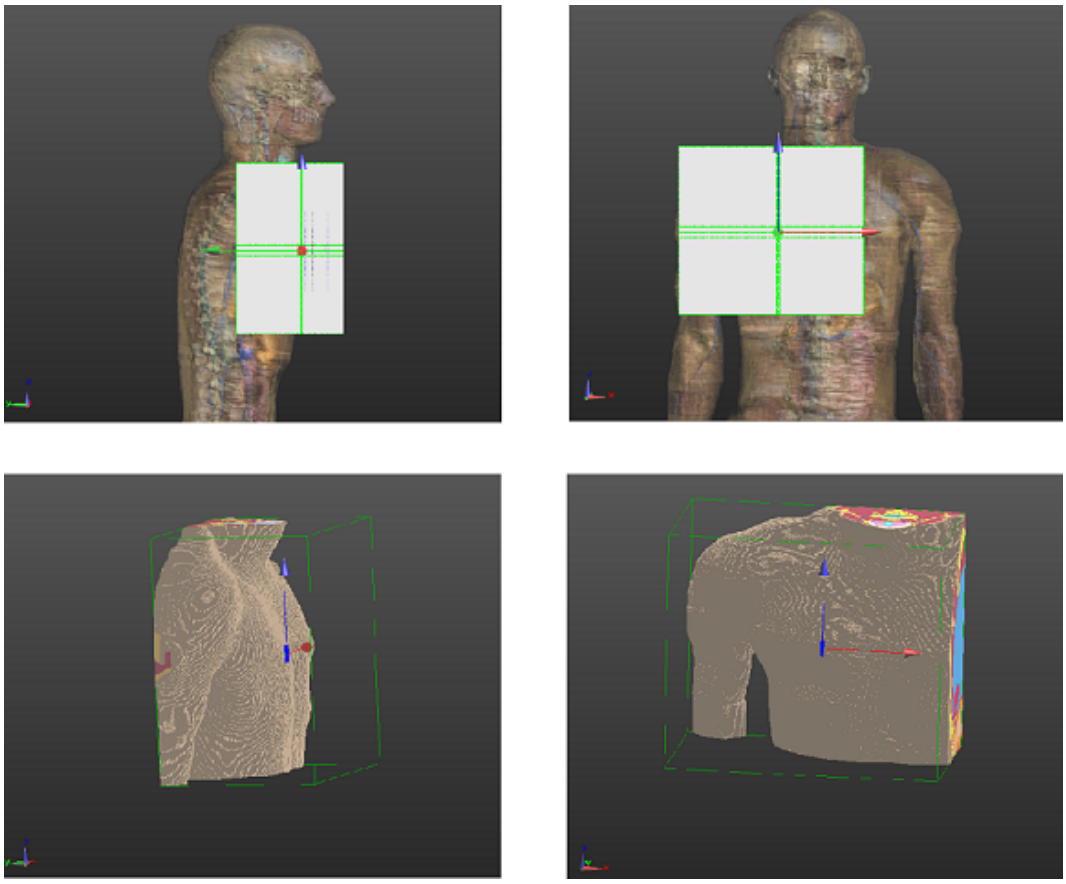

Figure 24: Above is the FDTD grid at 5800 MHz from front and right. Everything that is not contained within the grid is ignored. Below is the truncated and voxelized model ready for the simulation.

6.3 Simulation settings for Duke from the Virtual Family

The Duke phantom was available as a CAD (Computer Aided Design) model and a voxel model for different frequencies. The CAD representation of the phantom, which is designed solely for SEMCAD X, was used in this study.

The dipoles for the frequencies 900, 1450, 1800, 2450, 3500 and 5800 MHz were designed out of two symmetrical cylinders having the corresponding dimensions described in Table 12. The three lowest frequencies, 30, 150 and 450 MHz were ignored at the moment as further configurations were considered in order to reduce the dipole length. The dipoles were quadrupled and the clones were assigned to their respective locations at 5, 20 and 45 mm from the feed point of the original dipoles. After the transmitters were initialized, the male phantom Duke was imported into the computational domain. Then, a representative spot for the "Chest right" location was defined bearing in mind that there needed to be enough free space for the dipole to turn 90 degrees. The phantom was rotated and shifted so that the feed points of the closest dipoles ended up touching the skin layer of the model. Although, the surface of the phantom was unlevel, a modest attempt was made in order to achieve parallelism at this particular location between the plane of the outer layer of the model and the long axis of the dipoles. On the other hand, it would be practical to sustain the parallelism between the long axis of the model and the coordinate axis as this would yield optimal size for the computational domain, i.e. only a minimum amount of free space around the model would be contained within the rectangular grid. When a satisfying compromise was reached, the phantom was shifted 5 mm from the origin in y direction away from the dipoles, see Figure 25.

After the model was set, simulations were prepared for all frequencies and distances of interest. This meant setting "ignore" status in every simulation for all the dipoles expect for the one that had the right combination of the dimensions and the distance. The dielectric parameters and the densities of different tissues and organs of the phantom needed to be initialized with proper values. The values were obtained from the Gabriel material database that was included in the software. As the rest of the basic settings, i.e. sources and sensors, were dealt with, left were the configurations for the mesh and the cell size. As mentioned above, SEMCAD X provides an adequate way of limiting the size of the computational domain. Negative values for padding were set so that sufficient amount of the model was covered depending on the used frequency. Correspondingly, cell size was determined depending on the frequency and adjusted to insure both modest simulation time and accurate resolution. After the grids were generated all the prepared exposure scenarios were voxelized. Lastly, harmonic simulations were run using the "Run Batch" feature which automatically starts the next simulation after the one being processed has finished. Steady state was reached after 6 - 12 periods depending on size of the computational domain, i.e. frequency in use.

When all the required simulations for the "Chest right" location were conducted, that is, 24 simulations excluding the frequencies 30, 150 and 450 MHz, the next location on the body according to a definition "Shoulder" was determined. The location was set on the right shoulder as Figure 27 shows. Now, only the UPML

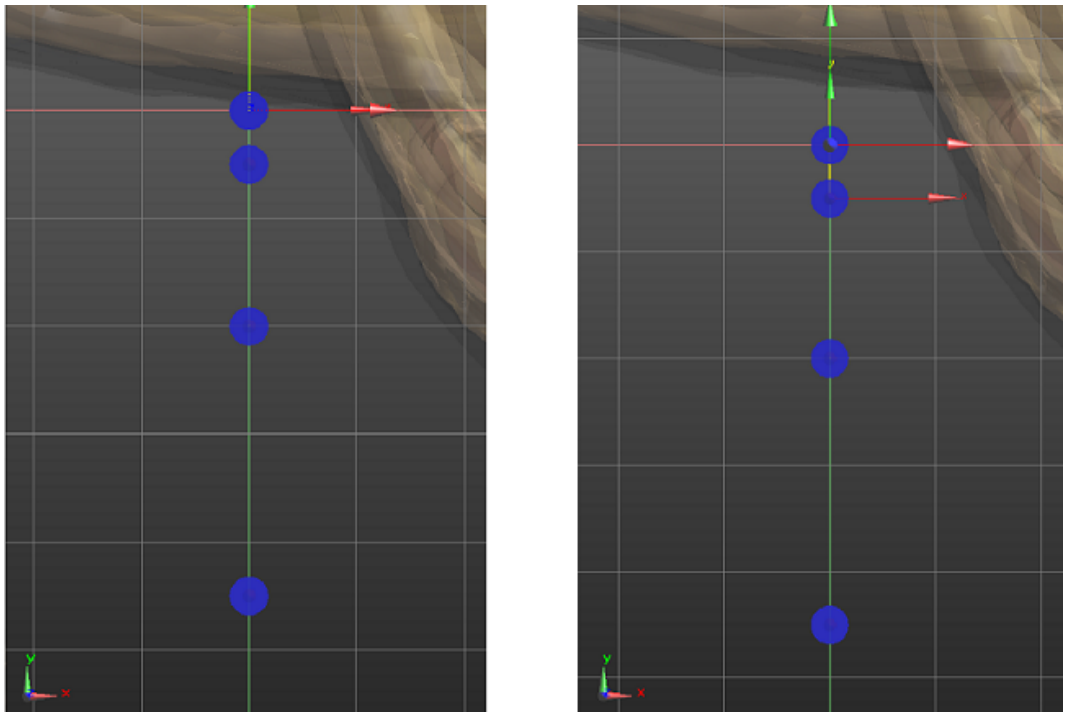

Figure 25: On the left the closest dipole is partially inside the phantom. On the right the phantom has been shifted 5 mm.

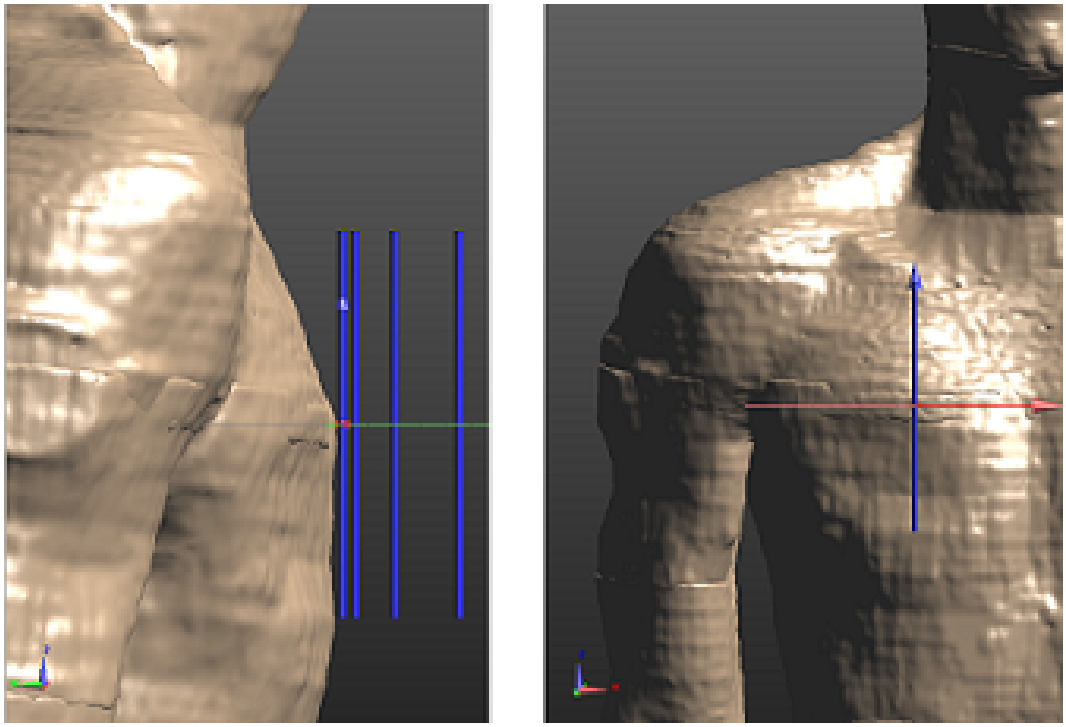

Figure 26: Depiction of the "Chest Right" location.

boundaries and the cell size needed to be reconfigured as the material parameters and such remained the same. The “Shoulder” location was followed by the “Waist A” and “Waist B” locations which were defined on the body by making use of the instructional picture provided, see Figures 28, 29 and 30. Correspondingly, locations were defined for “Thigh” and “Chest Middle” as shown in Figures 31 and 32. The “Chest Middle” position required some additional configuration as the surface geometry of the model at this region presented challenges. Figure 32 indicates that the shortest distance separating the model and the dipole had to be measured from the end of the dipole arm, not from the feed point. Because the arm length varies according to used frequency, this basically meant a separate treatment for each dipole and adding additional sources.

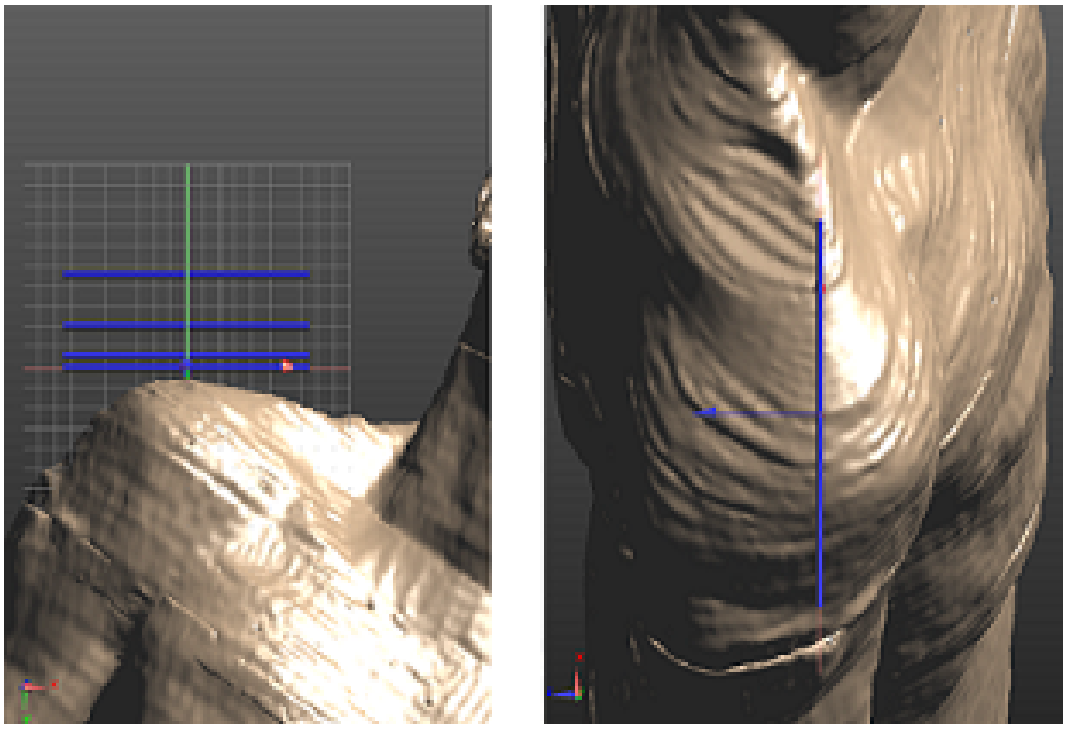

Figure 27: Depiction of the “Shoulder” location.

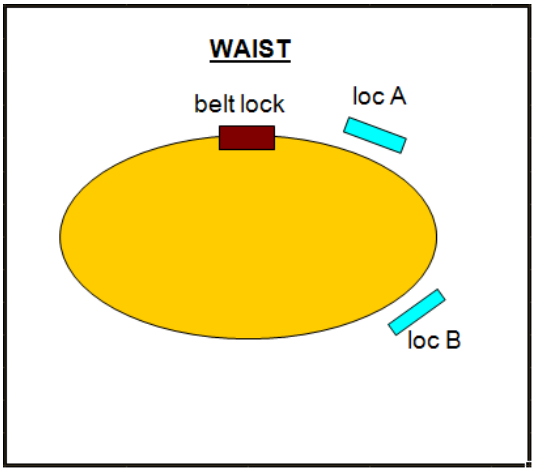

Figure 28: An instructional picture defining the locations of Waist A and B on a human phantom.

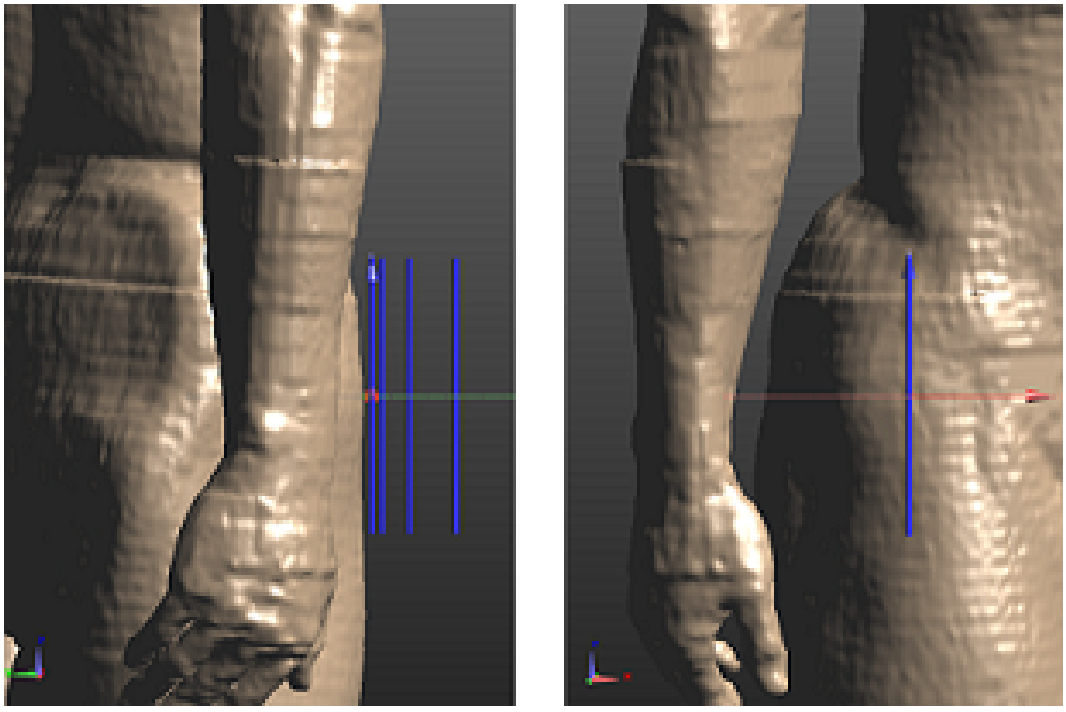

Figure 29: Depiction of the "Waist A" location.

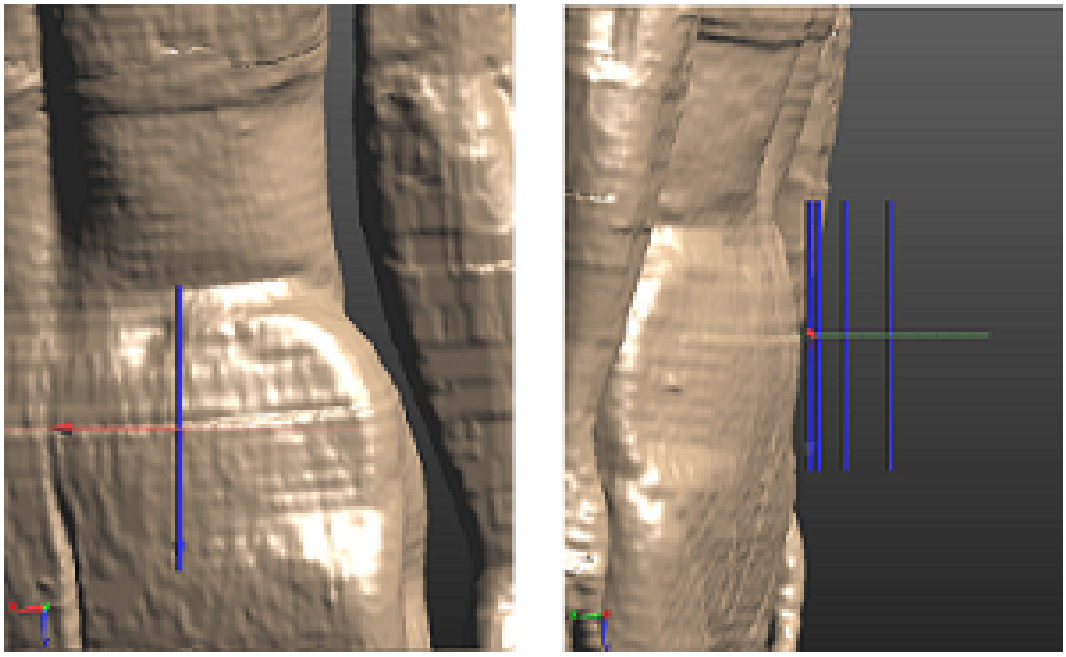

Figure 30: Depiction of the “Waist B” location.

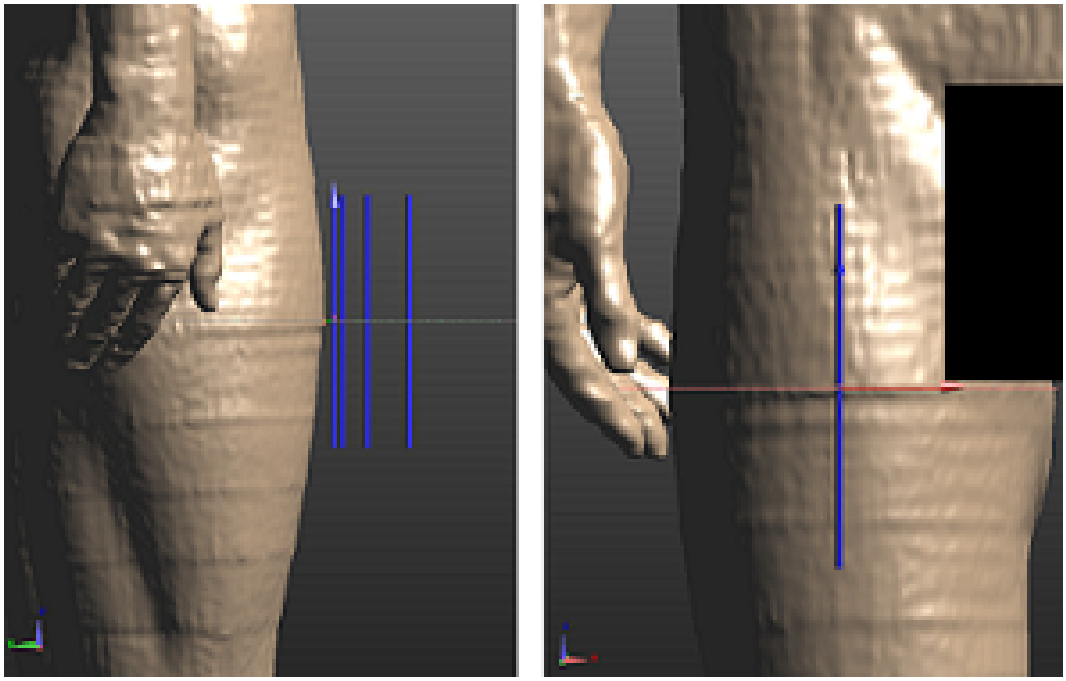

Figure 31: Depiction of the “Thigh” location.

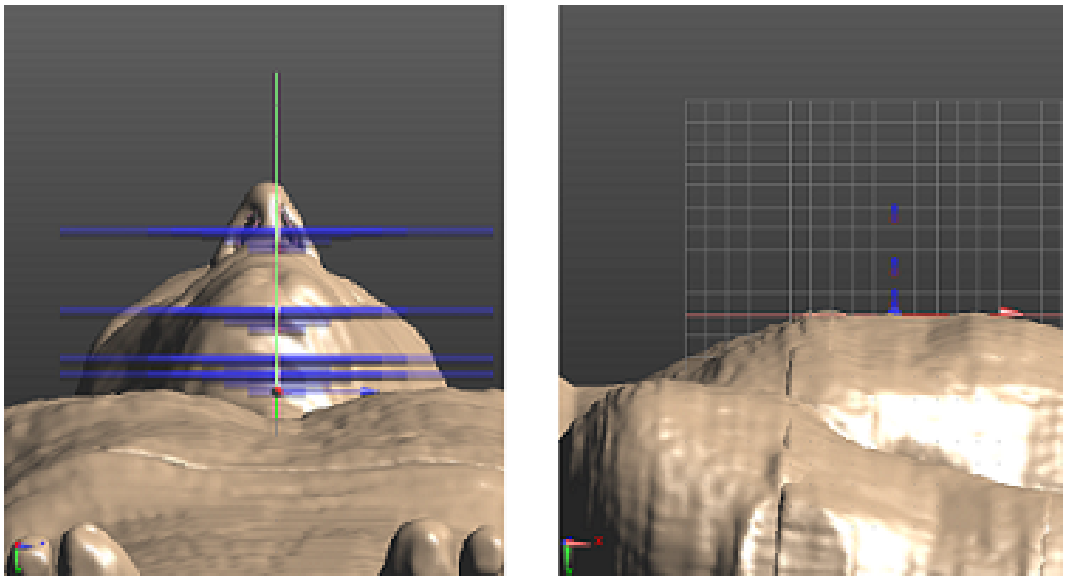

Figure 32: Depiction of the “Chest Middle” location.

The simulations were carried out with both vertical and horizontal polarizations. A different polarization was obtained by rotating the dipole antenna 90 degrees. In a rectangular coordinate system this would not cause any staircase errors in the antenna geometry. Also, no reconfiguration of the UPML boundaries was needed since the phantom remained in the same position with respect to the coordinate system. Because the dipoles were assigned multiple locations on the phantom, the definitions "vertical" and "horizontal" were case specific. The irradiation scenarios for all six locations using horizontal polarization are depicted in Figures 33, 34 and 35.

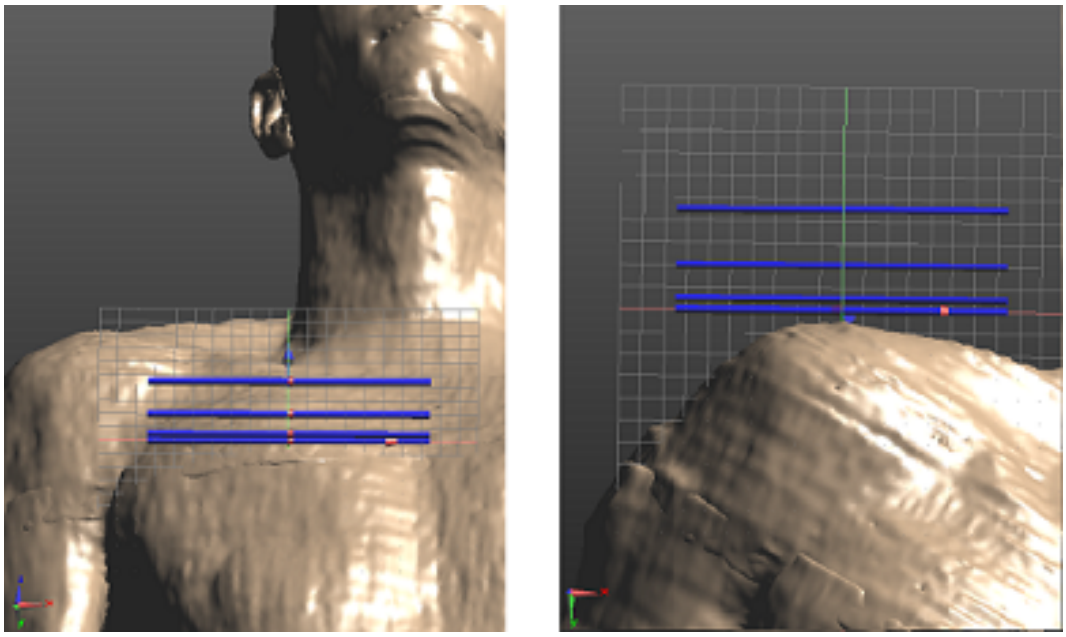

Figure 33: Depiction of the "Chest Right" and "Shoulder" location when the dipoles are tilted 90 degrees.

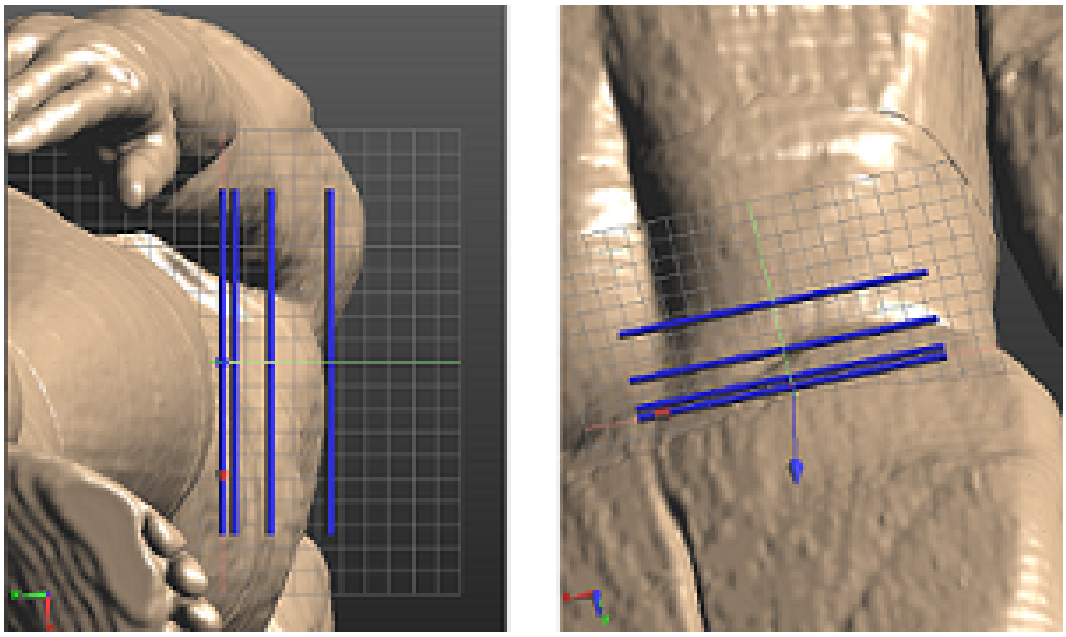

Figure 34: Depiction of the “Waista A” and “Waist B” location when the dipoles are tilted 90 degrees.

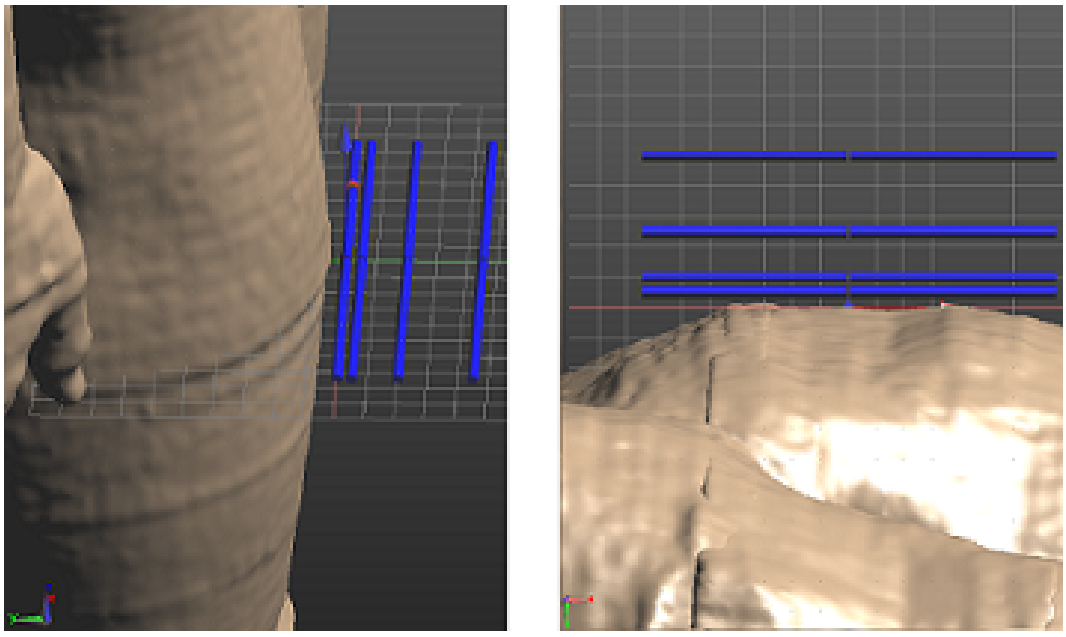

Figure 35: Depiction of the “Thigh” and “Chest Middle” location when the dipoles are tilted 90 degrees.

Lastly, simulations at 30, 150 and 450 MHz were considered. The length of a half wave dipole is 4997, 999 and 333 mm respectively at these frequencies and slightly shorter when a phantom is in close proximity. A transmitter of this length positioned close to the body obviously does not represent any real life situation. Additionally, a lengthy antenna compared to the height of the employed phantom would result in an unnecessarily extended computational domain and more challenging adjustments. However, it was decided that the length of a half-wave dipole at 450 MHz was somewhat within reasonable limits. Dipole length reductions by applying lumped inductor elements were considered for 30 and 150 MHz frequencies. Several attempts to optimize the dipole length with two inductors located symmetrically at both arms were made for 150 MHz. However, no feasible matching was reached that would yield satisfactory results on all distances and body locations. 30 MHz proved to be an even more challenging case. Consequently, slightly reduced original half-wave lengths of the dipoles were applied, see Table 12.

Due to the extreme length of the dipoles at lower frequencies, different dipole positions were considered at some body locations to prevent overlapping between PEC and dielectric materials. A new "Shoulder" location for frequencies 30 and 150 MHz was decided as shown in Figure 36. Correspondingly, the new locations for "Thigh", "Waist A", "Waist B" and "Chest Right" are displayed in Figures 36 - 39.

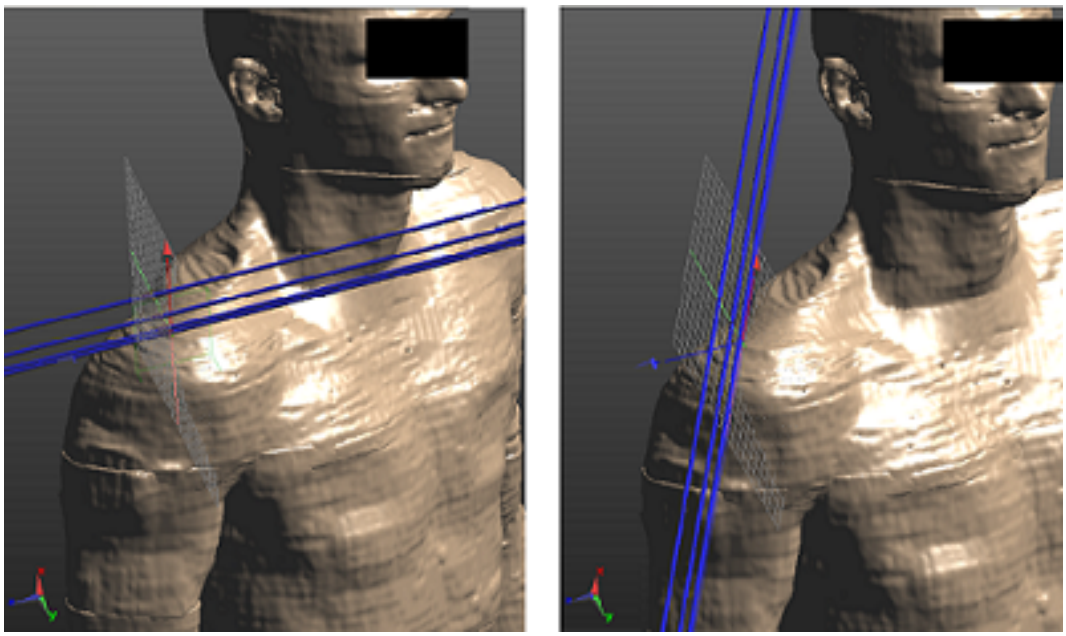

Figure 36: Depiction of the "Shoulder" location for both polarizations used for frequencies 30, 150 and 450 MHz.

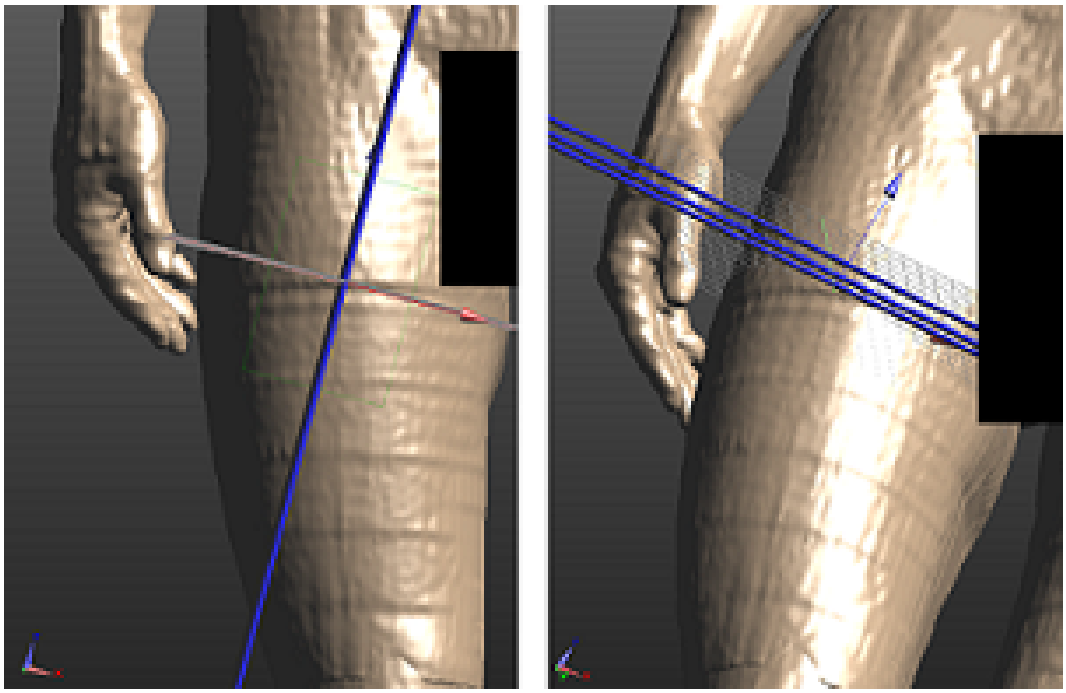

Figure 37: Depiction of the "Thigh" location for both polarizations used for frequencies 30, 150 and 450 MHz.

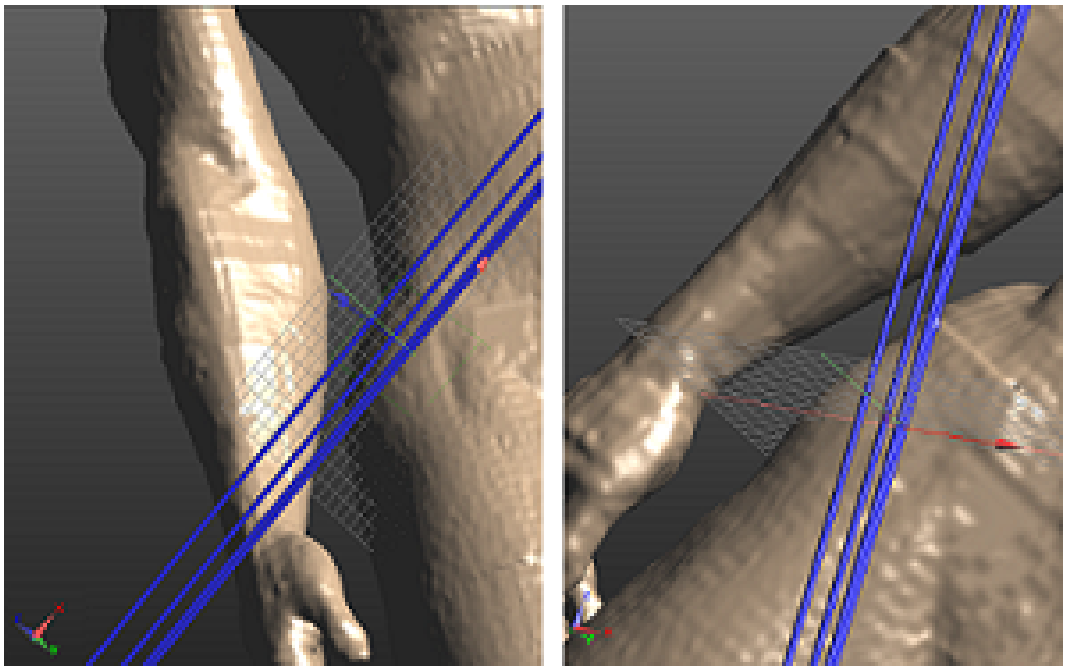

Figure 38: Depiction of the "Waist A" location for both polarizations used for frequencies 30, 150 and 450 MHz.

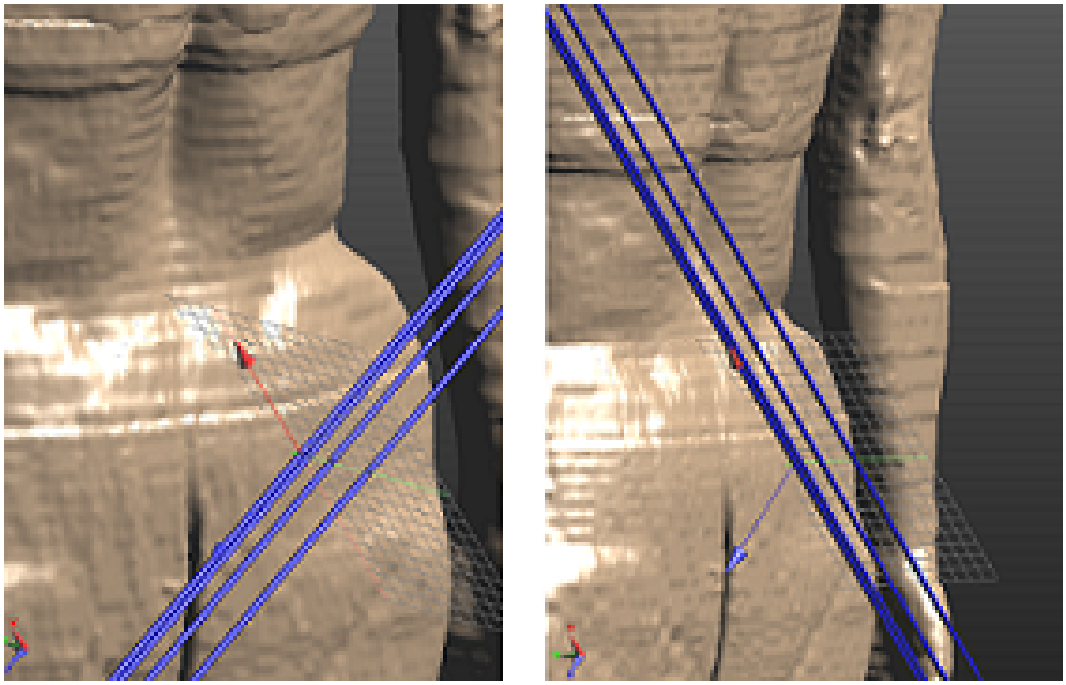

Figure 39: Depiction of the "Waist B" location for both polarizations used for frequencies 30, 150 and 450 MHz.

6.4 Simulation settings for the flat phantom

In the case of the flat phantom only one location was considered for the dipoles, see Figure 40. It was defined according to the instructions in the IEC-62209 Part 2 document. As instructed, the half-wave dipoles were positioned below the bottom of the flat phantom and centred with their axis parallel to the longest dimension of the phantom. A 5 mm distance was measured between the closest dipole and the surface of the liquid as depicted in Figure 41. Simulations were conducted for both the IEC and FCC proposed liquid parameters.

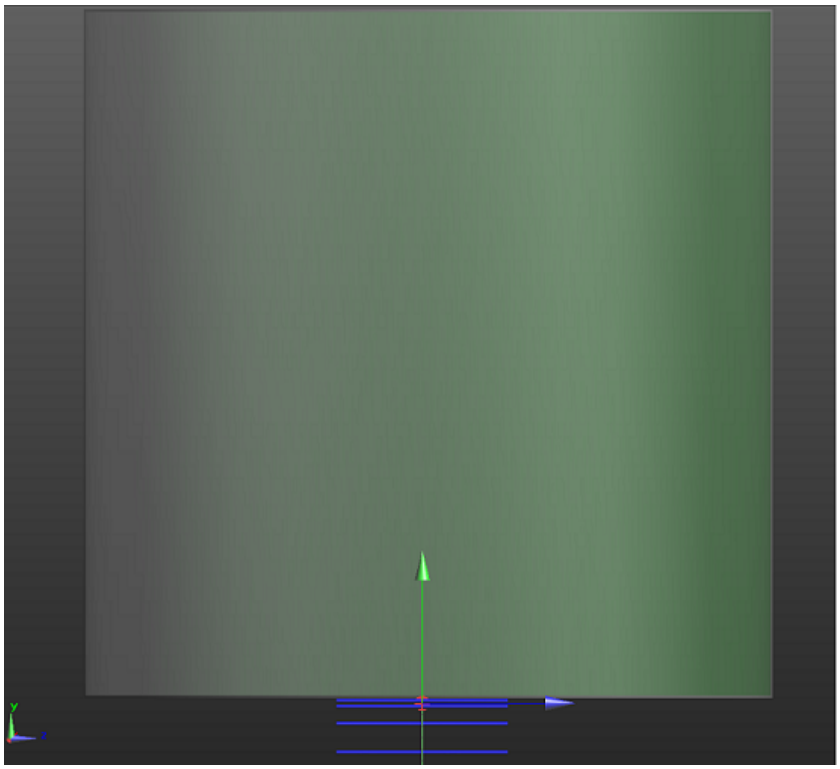

Figure 40: The dipoles positioned near the flat phantom.

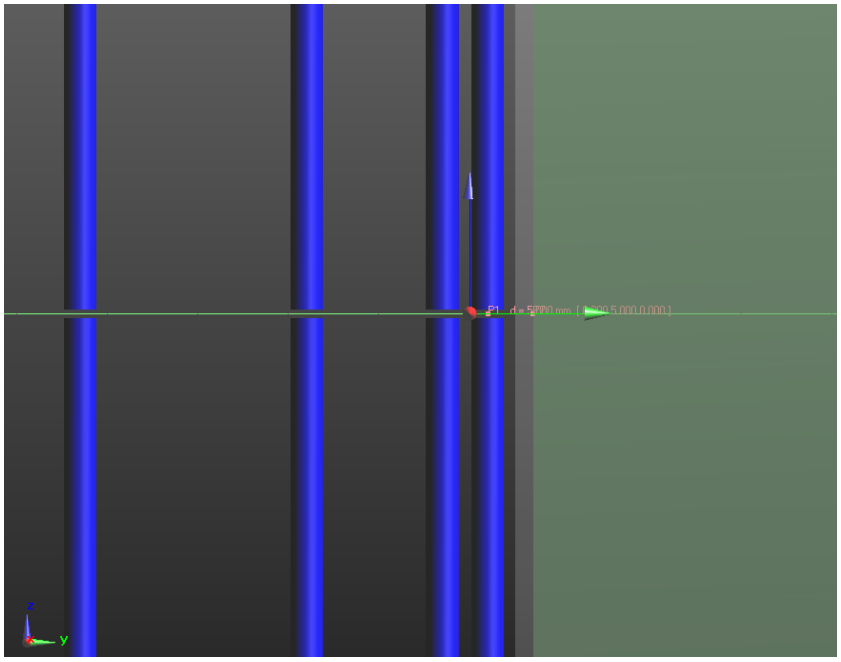

Figure 41: The distance was measured between the dipole axis and the surface of the tissue simulant liquid.

7 Results

The only extracted quantities from the simulations were the 1 and 10 g averaged SAR values. Additionally, pictures of the SAR distributions across the irradiated phantoms were taken, as this would provide additional data for further analysis.

While the strength of the electromagnetic fields decreases as a function of distance, according to Equation 26 the value of the SAR is expected to diminish respectively. Field gradients are expected to be high in the region near the antenna. Thus, when the antenna is shifted further from the phantom the absorption becomes more uniform throughout the irradiated region. The 10 g SAR distributions in the flat phantom at 900 MHz for the distances 5, 10, 25 and 50 mm are shown in Figures 42 and 43. 900 MHz was chosen for the demonstration because at this frequency radiation has fairly modest penetration capabilities reaching the deeper layers of the human body. The corresponding distributions in Duke phantom when it was irradiated at the "Chest Right" location are shown in Figure 44. The pictures of the Flat phantom are taken from the left showing only the cutting plane where the peak value of the SAR within the 10 g cube was detected. The pictures of Duke are taken from the top also visualizing only the cutting plane. As is shown in Figure 42 absorption is very intense near the feed point of the antenna, hence the peak averaged SAR is typically found near this region. Because of the complex geometry of the employed phantom and the multiple tissue interfaces contained within it, the SAR distributions are hardly distinguishable when the distance of the radiator increases gradually from 5 to 50 mm as indicated by Figure 44.

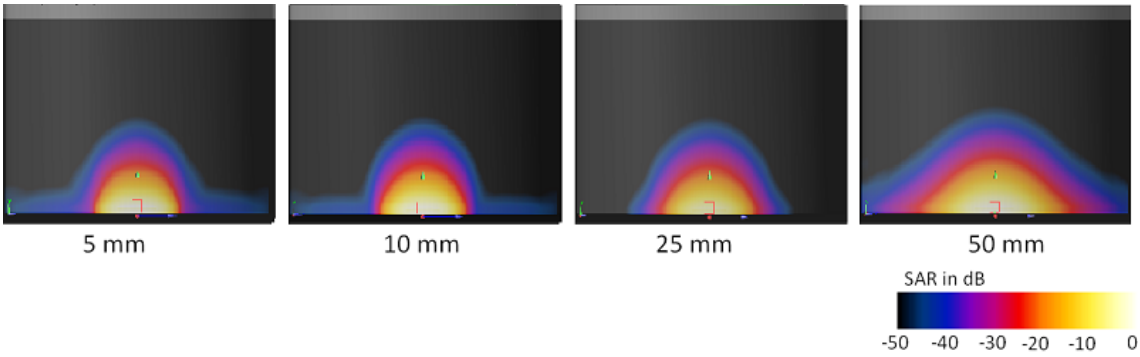

Figure 42: 10g averaged SAR distribution at 900 MHz for distances 5, 10, 25 and 50 mm when the flat phantom is characterized by the tissue simulant parameters proposed by IEC.

As discussed previously, the penetration capabilities of radiation depends on the used frequency. Figures 45 and 46 illustrate peak 10g averaged SAR distribution when frequency increases from 30 MHz to 5800 MHz. Again, the flat phantom is depicted from the left and the top view of the "Chest Right" location was used to record the SAR distributions in Duke. Respectively, only the cutting planes of the models where the peak SAR within the averaging cube was detected are displayed.

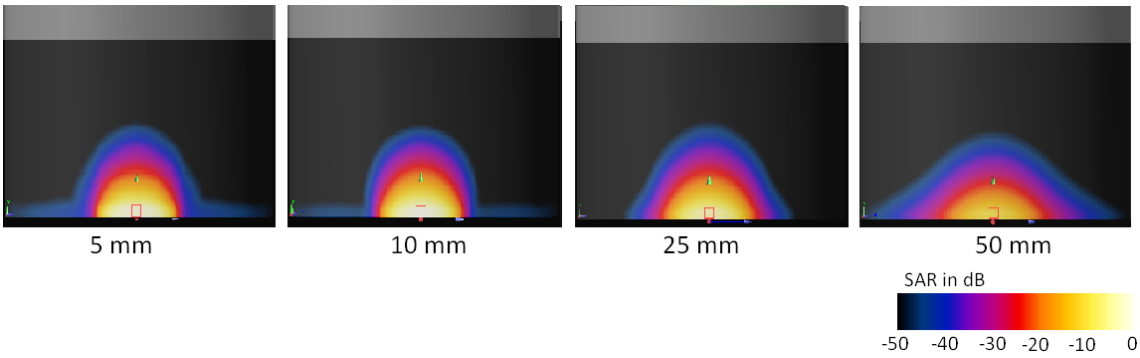

Figure 43: 10g averaged SAR distribution at 900 MHz for the distances 5, 10, 25 and 50 mm when the flat phantom is characterized by the tissue simulant parameters proposed by FCC.

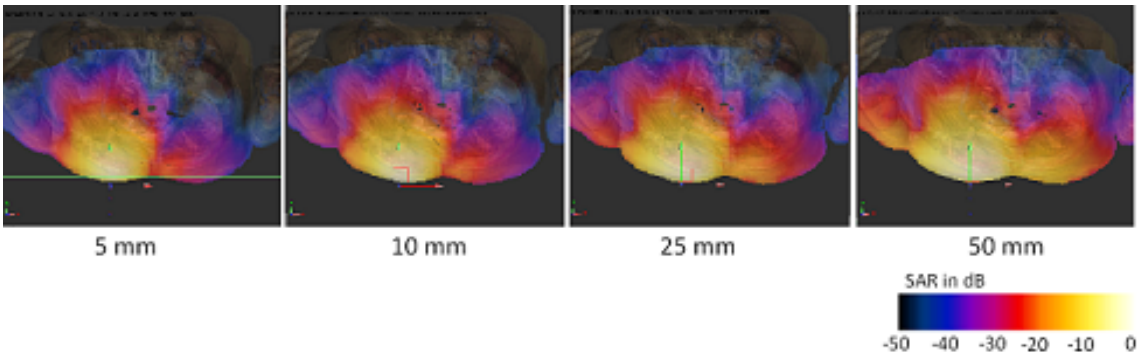

Figure 44: 10g averaged SAR distribution at 900 MHz for the distances 5, 10, 25 and 50 mm ("Chest Right" location on Duke).

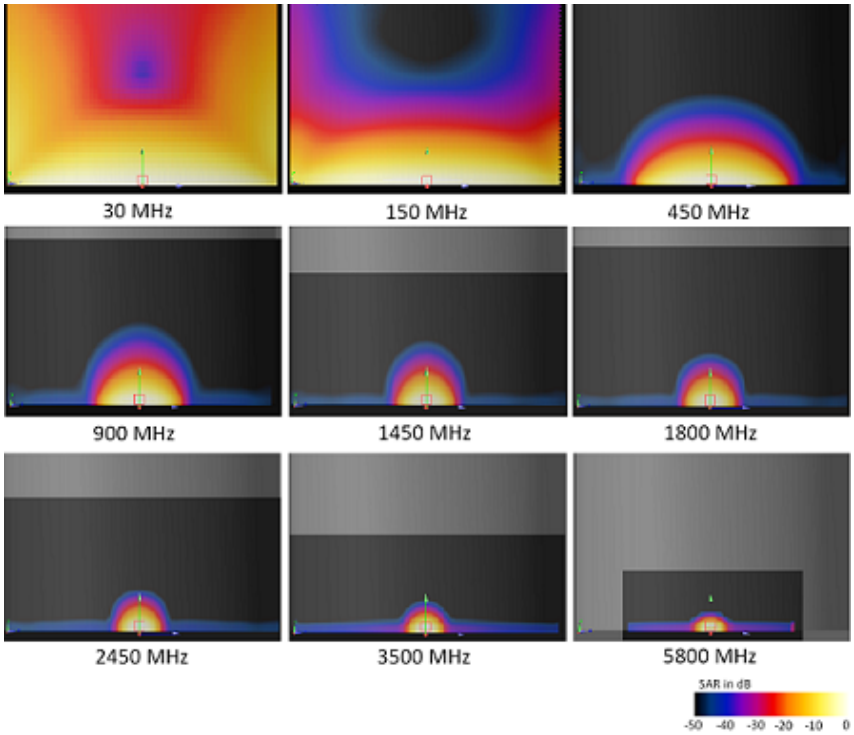

Figure 45: 10g averaged SAR distribution for the frequencies 30 to 5800 MHz in the flat phantom (IEC) irradiated at 10 mm distance.

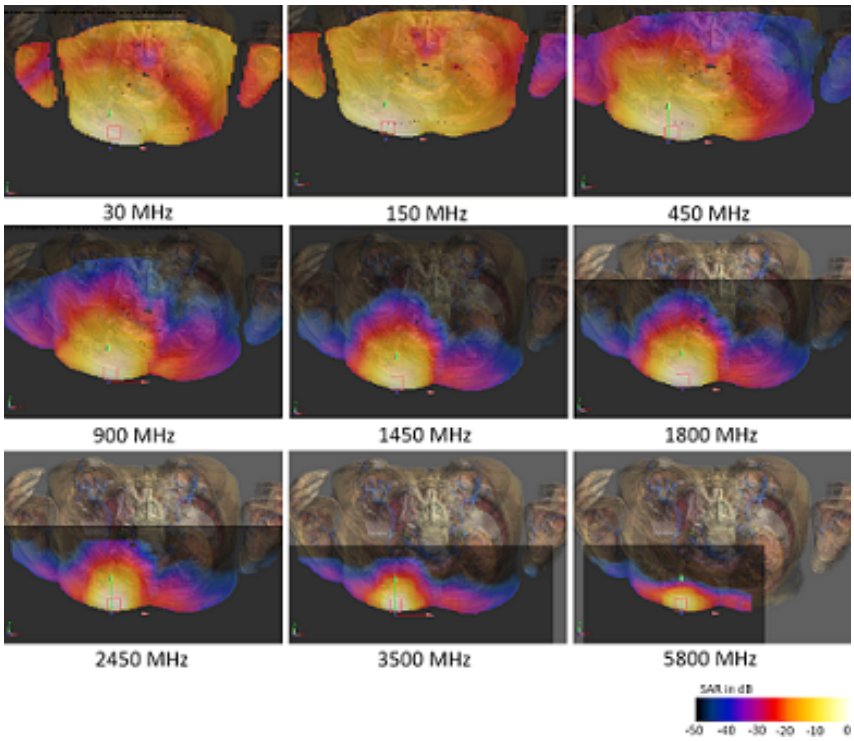

Figure 46: 10g averaged SAR distribution for the frequencies 30 to 5800 MHz in Duke phantom ("Chest Right" location) irradiated at 10 mm distance.

The 10 g averaged SAR results for all combinations of distances, frequencies and locations are presented in Figures A1 - A12 in Appendix A. In these graphs the SAR values obtained in the human phantom are compared to the respective SAR values recorded in liquid defined by both the IEC and FCC parameters. The other polarization on the same location is referred to as "H-pol", i.e. when the antenna is rotated 90 degrees.

A separate treatment is given for cases where the flat phantom underestimated SAR. In Figures 47 - 49 the underestimated SAR values are normalized to both the IEC and FCC results. This normalization was done in order to obtain the deviations in percentages, which makes it easier to analyse the results. Again, "H-pol" marking refers to the other used polarization.

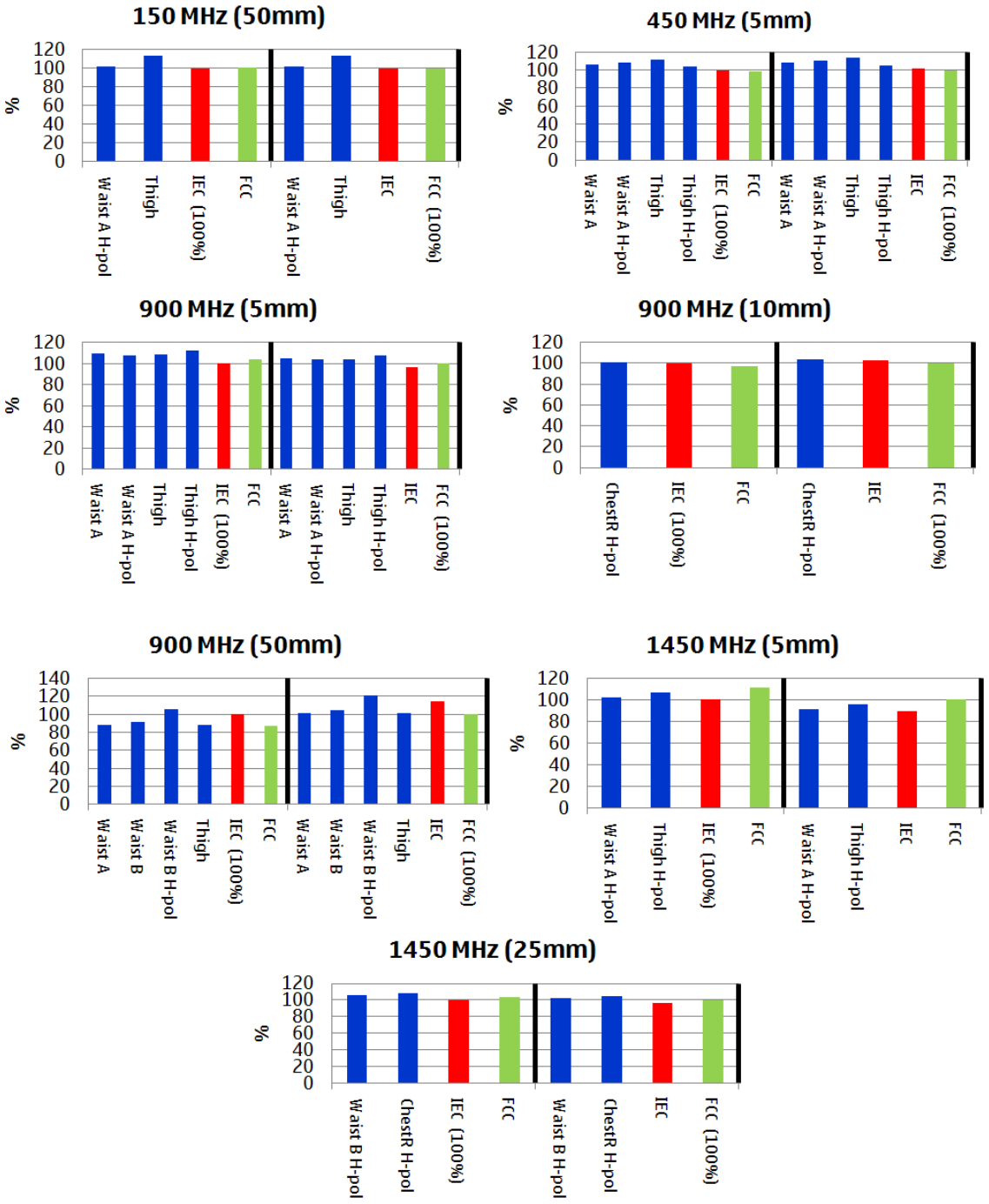

Figure 47: Cases where the flat phantom underestimates SAR.

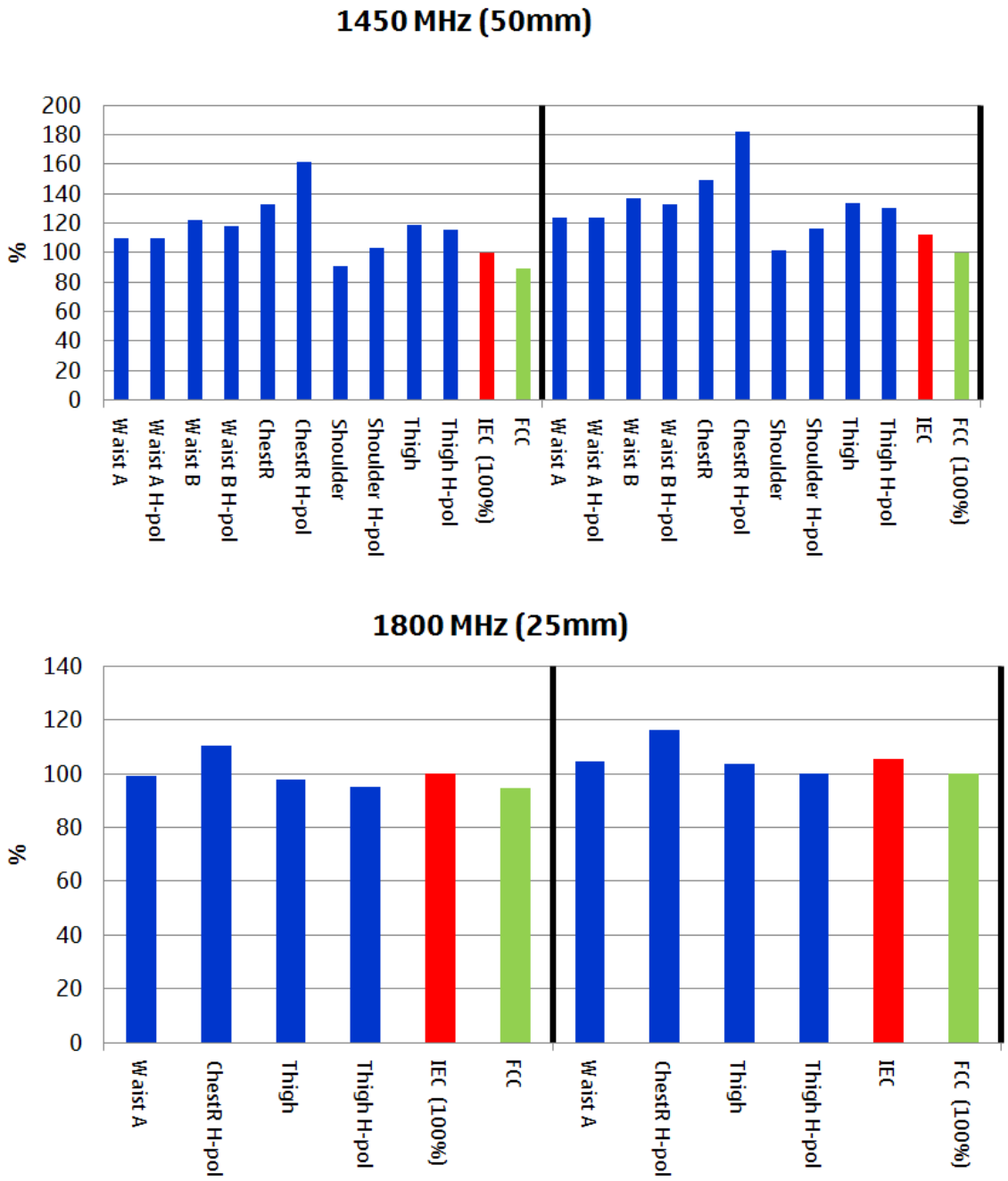

Figure 48: Cases where the flat phantom underestimates SAR.

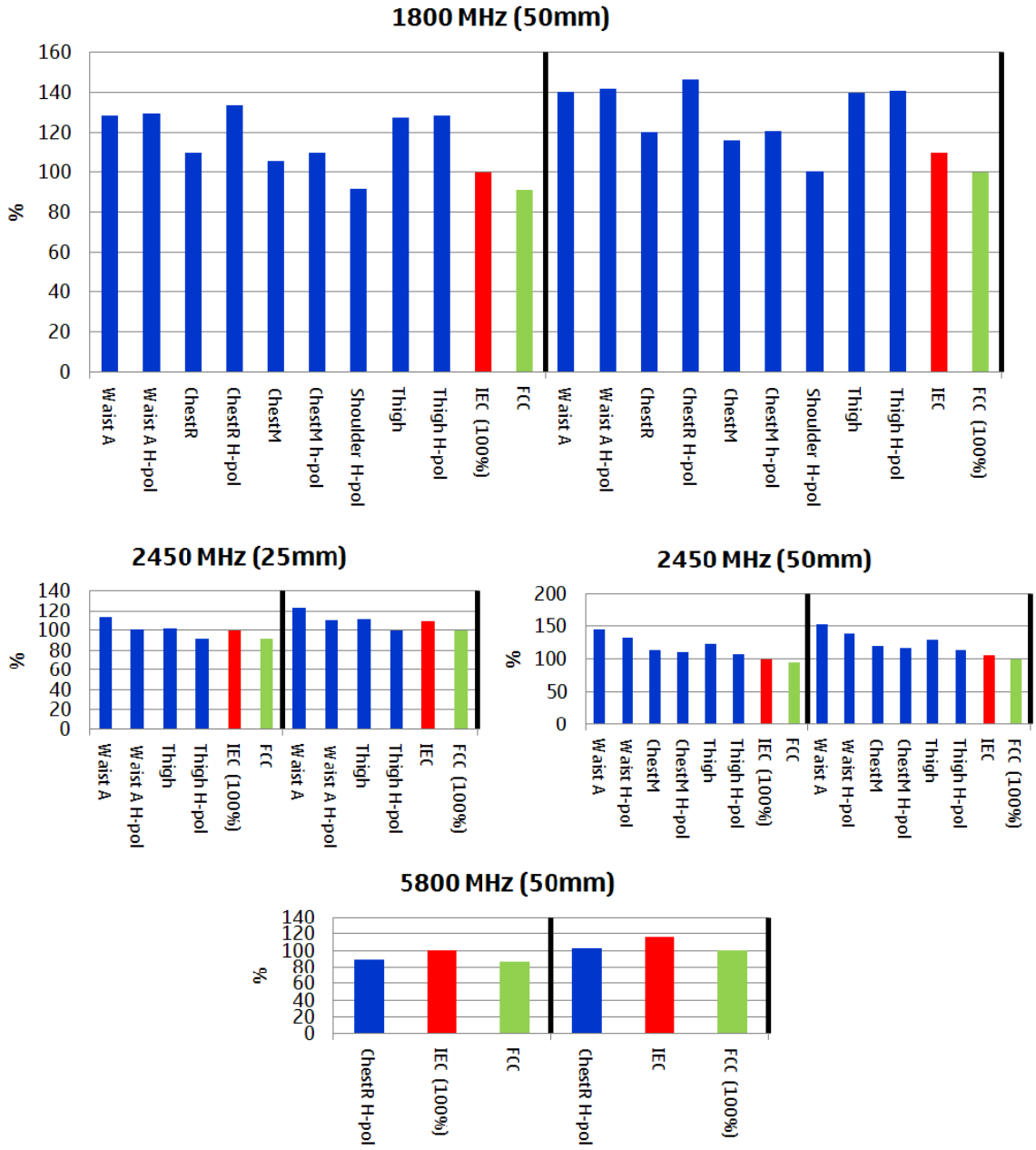

Figure 49: Cases where the flat phantom underestimates SAR.

In summary, a total of 432 exposure scenarios were simulated. The flat phantom underestimated SAR in 53 cases. This happened with both the IEC and FCC proposed liquid parameters in 41 cases. Underestimation with only the FCC parameters was perceived in 10 cases and, correspondingly, with only the IEC parameters in 2 cases. Thus, when the IEC parameters were employed the flat phantom underestimated SAR in 43 cases and when the FCC parameters were used underestimation was noticed in 51 cases. Out of the 53 cases 44 included the same dipole location with both polarization, i.e. rotating the dipole 90 degrees did not result in a significant deviation in the SAR value. The major contributors to the 53 cases, where the flat phantom underestimated SAR, were the "Thigh" and "Waist A" locations, as they are represented 15 and 14 times respectively in Figures 47 - 49. Correspondingly, the "Chest Right" location appears 8 times, "Waist B" and "Shoulder" 3 times each and "Chest Middle" 2 times. Most of the underestimations took place at middle frequencies: 9 underestimations at 900 MHz, 14 at 1450 MHz, 15 at 1800 MHz and 10 at 2450 MHz. The rest consisted of 2 underestimations at 150 MHz, 4 at 450 MHz and 1 at 5800 MHz. 50 mm appeared to be the most problematic distance with its 32 out of 53 representation of the underestimation cases. However, it is worth mentioning that in a typical measurement situation 25 mm is the furthest irradiation distance for body mounted devices. 25 and 5 mm distances yielded both 10 underestimations and the 10 mm distance only 1.

In the 43 underestimated cases SAR in the human model exceeds SAR in the flat phantom described by the IEC parameters on average by 14.17 %. Respectively, when the FCC parameters were used, i.e. 51 underestimation cases, the SAR exceeding was on average 18.30 %. At worst, the human model yielded 61.94 % higher SAR (1450 MHz 50mm ChestRight H-pol) with respect to the IEC liquid and 82.10 % higher with respect to the FCC liquid. Typically, 30 % is regarded as an error margin for this type of simulation. Considering the IEC parameters, 5 cases were found where the 30 % threshold is exceeded. For the FCC parameters 30 % error margin was exceeded 13 times.

8 Conclusions

In this study the validity of tissue simulant liquids proposed by IEC and FCC were assessed. The assessment was carried out with the FDTD based simulation platform SEMCAD X. The SAR values in the flat phantom filled with the aforementioned liquids were compared to the SAR values in an anatomically realistic human male phantom. Typical measurement settings were considered in these simulations, i.e. deciding several locations on the body that are most commonly exposed to small radiating devices and performing the simulations at a few different distances. It is expected for the SAR in the flat phantom to slightly overestimate the SAR in the human model. According to the results this was not always the case. Of 432 exposure scenarios 53 yielded higher SAR than in the flat phantom with respective settings. Over half of these cases resulted when the transmitter was furthest from the body, i.e 50 mm. As mentioned above, this distance is not used in actual measurement procedures, the longest distance between the DUT and the body being typically 25 mm, but was merely included in this study as a point of reference.

The highest SAR values were reached in the "Waist A" and "Thigh" locations. Respectively, the majority of the underestimations, when the flat phantom produced lower SAR, took place at these locations. The values remained almost the same when rotating the antenna 90 degrees, which implies that the specific body surface geometry at these locations did not have a significant effect on the radiation properties of the antenna and thus did not contribute to the high SAR. The next highest SAR values were obtained in the "Chest Right" location and only a few underestimations happened in the "Waist B", "Shoulder" and "Chest Middle" locations. The last three mentioned locations are characterized by presence of a bone near the surface while the first three consists mainly of muscle. As expected, lower SAR is to be found when the irradiated region consists of bone tissue, i.e. dry tissue, in addition to muscle tissue. However, since the dielectric parameters of the FCC liquid are those of muscle, the effects of tissue interfaces and other characteristics of a heterogeneous phantom are to be considered.

The study provided also a way to compare the two liquids with each other, e.g. which one would yield more anticipated results. However, while in general the underestimations by the IEC liquid were somewhat meager than those of the FCC liquid, the difference was not significant. Correspondingly, few cases were confronted where the IEC liquid produced underestimations while the FCC liquid did not. Based on these results, there is no substantial difference when using the dielectric parameters of head (IEC) or muscle (FCC).

Although, in some cases, the results of this study indicate the inability of the liquids to represent the human tissues for measurement purposes, further research with different human models is yet required. In upcoming studies it could be considered employing an obese model, thus assessing the effect of an increased fat layer. In addition, similar analysis on female and child phantoms would be required to obtain a more feasible representation of the general public.

References

[1] Yee, K. S. "Numerical solution of initial boundary value problems involving Maxwell's equations in isotropic media," *IEEE Trans. Antennas Propagat.,* vol. AP-14, pp. 302–307, 1966.

[2] Taflove, A. and Hagness S. C. *Computational Electrodynamics: The Finite-Difference Time-Domain Method* Artech House, 3rd ed., 2005.

[3] Taflove, A. "Review of FD-TD Numerical Modeling of Electromagnetic Wave Scattering and Radar Cross Section," *Proceedings of the IEEE,* vol. 47, pp. 682–699, 1989.

[4] Taflove, A. and Brodwin M. E. "Numerical Solution of Steady-state Electromagnetic Scattering Problems Using the Time Dependent Maxwell's Equations," *IEEE Transactions on Microwave Theory and Techniques,* vol. MTT-23, pp. 623–630, 1975.

[5] Yu, W. and Mittra R. "A Conformal FDTD Software Package Modeling Antennas and Microstrip Circuit Components," *IEEE Antennas and Propagation Magazine,* vol. 42, pp. 28–39, 2000.

[6] Shlager, K. L. and Schneider J. B. "A Selective Survey of the Finite-Difference Time-Domain Literature," *IEEE Antennas and Propagation Magazine,* vol. 37, pp. 39–56, 1995.

[7] Berenger, J. P. "A Perfectly Matched Layer for the Absorption of Electromagnetic Waves," *Journal of Computational Physics,* vol. 117, pp. 185–200, 1994.

[8] Sadiku, M. N. O. *Numerical Techniques in Electromagnetics* CRC Press LLC, 2nd ed., 2001.

[9] Katz, D. S., Taflove A. and Thiele, E. T. "Validation and Extension to Three Dimensions of the Berenger PML Absorbing Boundary Condition for FD-TD Meshes," *IEEE Microwave and Guided Wave Letters,* vol. 4, pp. 268–270, 1994.

[10] Gedney, S. D. "An Anisotropic Perfectly Matched Layer-Absorbing Medium for the Truncation of FDTD Lattices," *IEEE Trans. Antennas Propagat.,* vol. 44, pp. 1630–1639, 1996.

[11] International Comission on Non-Ionizing Radiation Protection "Guidelines for Limiting Exposure to Time-Varying Electric, Magnetic, and Electromagnetic Fields (up to 300 GHz)," *Health Physics ,* vol. 74, pp. 494–522, 1998.

[12] Kumar, N. S., Alamelu, N., Bharathy, B. R. Piriyavathani, V. "FDTD based evaluation of Specific Absorption Rate distribution in human head due to mobile phones ," *Electromagnetic Interference and Compatibility,* pp. 411 – 417 , 2008.

[13] IEEE Std 1528-2003 *IEEE Recommended Practice for Determining the Peak Spatial-Average Specific Absorption Rate (SAR) in the Human Head From Wireless Communications Devices: Measurement Techniques,* IEEE, 2003.

[14] Nyberg, H. and Jokela, K. (Editors), *Ionisoimaton säteily Sähkömagneettiset kentät.* Radiation and Nuclear Safety Authority of Finland, 2006.

[15] Gandhi, O. P. "State of the knowledge for electromagnetic absorbed dose in man and animals," *Proceedings of the IEEE,* vol. 68, pp. 24 – 32, 1980.

[16] Räisänen, A. and Lehto, A. *Radiotekniikan perusteet.* Otatieto, 12th ed., 2007.

[17] Michaelson, S. M "Human exposure to nonionizing radiant energy - Potential hazards and safety standards," *Proceedings of the IEEE,* vol. 60, pp. 389 – 421, 1972.

[18] Johnson, C. C. and Guy, A. W. "Nonionizing electromagnetic wave effects in biological materials and systems ," *Proceedings of the IEEE,* vol. 60, pp. 692 – 718, 1972.

[19] International Commission on Non-Ionizing Radiation Protection (ICNIRP), "Guidelines for limiting exposure to time-varying electric, magnetic , and electromagnetic fields (up to 300 GHz)," *Health Physics,* vol. 74, pp. 494 – 522 , 1998.

[20] IEEE Std. C95.1 - 2005, *IEEE Standard for Safety Levels with Respect to Human Exposure to Radio Frequency Electromagnetic Fields, 3 kHz to 300 GHz,* IEEE, 2006.

[21] Federal Communications Committee, Office of Engineering and Technology, *Evaluating Compliance with the FCC Guidelines for Human Exposure to Radiofrequency Electromagnetic Fields, Additional Information for Evaluating Compliance of Mobile and Portable Devices with FCC Limits for Human Exposure to Radiofrequency Emissions,* Supplement C (Edition 01-01) to OET Bulletin 65 (Edition 97-01), June 2001.

[22] "Magnolia Medical imaging Center". [Online]. Available: `http://camoodle.org/magnolia/index.php` [Accessed: Aug. 14. 2010].

[23] Gualdrini, G. "Monte Carlo Simulations for In Vivo Internal Dosimetry (including phantom development)". [Online]. Available: `http://w3.tue.nl/nl/diensten/daz/amvs/sbd/sbd_tue_studiemateriaal/irpa_refresher_courses/` [Accessed: Nov. 27. 2010].

[24] Petoussi-Henss, N., Zankl, M., Fill U, J. and Regulla, D. "The GSF family of voxel phantoms," *Physics in Medicine and Biology,* vol. 47, pp. 89 - 106, 2002.

[25] Caon, M. "Voxel-based computational models of real human anatomy: a review," *Radiation and Environmental Biophysics,* vol. 42, pp. 229 - 235, 2004.

[26] Snyder, W. S., Ford, M. R., Warner, G. G. and Fisher, H. L. Jr. "Estimates of absorbed fractions for monoenergetic photon sources uniformly distributed in various organs of a heterogeneous phantom (Medical Internal Radiation Dose Committee (MIRD) Pamphlet No 5, Supplement No 3)," *Journal of Nuclear Medicine,* vol. 10, 1969.

[27] International Commission on Radiological Protection, *Report of the Task Group on the Reference Man,* ICRP Publication 23, 1975.

[28] Gajsek, P., Hurt, W. D., Ziriax, J. M., and Mason, P. A. "Parametric dependence of SAR on permittivity values in a man model," *IEEE Transactions on Biomedical Engineering,* vol. 48, pp. 1169 - 1177, 2001.

[29] Zankl, M., Veit, R., Williams, G., Schneider, K., Fendel, H., Petoussi, N. and Drexler, G. "The construction of computer tomographic phantoms and their application in radiology and radiation protection," *Radiation and Environmental Biophysics,* vol. 27, pp. 153 - 164, 1988.

[30] Zubal, G., Harrel, C., Smith, E., Ratner, Z., Gindi, G. and Hoffer, P. "Computerised three-dimensional segmented human anatomy," *Medical Physics,* vol. 21, pp. 299 - 302, 1994.

[31] Dimbylow, P-J. "TFDTD calculations of the whole-body averaged SAR in an anatomically realistic voxel model of the human body from 1 MHz to 1 GHz," *Physics in Medicine and Biology,* vol. 42, pp. 479 - 490, 1997.

[32] Zankl, M. and Wittman, A. "The adult male voxel model "Golem" segmented from whole-body CT patient data," vol. 40, pp. 153 - 162, 2001.

[33] Caon, M., Bibbo, G., and Pattison, J. "An EGS4-ready tomographic computational model of a fourteen year-old female torso for calculating organ doses from CT examinations," *Physics in Medicine and Biology,* vol. 44, pp. 2213 – 2225, 1999.

[34] Saito, K., Wittman, A., Koga, S., Ida, Y., Kamei T, H., Funabiki J, N. and Zankl, M. "Construction of a computed tomographic phantom for a Japanese male adult and dose calculation system," *Radiation and Environmental Biophysics,* vol. 40, pp. 69 - 76, 2001.

[35] Nipper, J., Williams, J. and Bolch, W. "Creation of two tomographic voxel models of paediatric patients in the first year of life," *Physics in Medicine and Biology,* vol. 47, pp. 3143 – 3164, 2002.

[36] Choonik, L., Choonsik, L., Williams, J. and Bolch, W. "Whole-body voxel phantoms of paediatric patients - UF Series B," *Physics in Medicine and Biology,* vol. 51, pp. 4649 - 4661, 2006.

[37] Ackerman, M. J. "The Visible Human Project™: a resource for anatomical visualization," *Proceedings of the IEEE Engineering in Medicine and Biology Society Region 8 International Conference,* pp. 29 - 31, 1997.

[38] Fill, U. A., Zankl, M., Petoussi-Henss, N., Siebert, M. and Regulla, D. "Adult Female Voxel Models of Different Stature and Photon Conversion Coefficients," *Health Physics,* vol. 86(3), pp. 253 - 272, 2004.

[39] Nagaoka, T., Watanabe, S., Sakurai, K., Watanabe, A., Taki, M. and Yamanka, Y. "Development of realistic high resolution whole-body voxel models of Japanese adult male and female of average height and weight, and application of models to radio-frequency electromagnetic-field dosimetry," *Physics in Medicine and Biology,* vol. 49, pp. 1 - 15, 2004.

[40] Lee, C. and Lee, J. "The Korean reference adult male voxel model "KRman" segmented from 23 whole-body MR data and dose conversion coefficients (abstract only)," vol. 84, 2003.

[41] Shi, C. and Xu, X. "Development of a 30-week-pregnant female tomographic model from computed tomography CT images for Monte Carlo organ dose calculations," *Medical Physics,* vol. 31(9), pp. 2491 - 2497, 2004.

[42] Dimbylow, P. "Development of the female voxel phantom, NAOMI, and its application to calculations of induced current densities and electric fields from applied low frequency magnetic and electric fields," *Physics in Medicine and Biology,* vol. 50, pp. 1047 – 1070, 2005.

[43] Christ, A., *et al* "The Virtual Family - development of surface-based anatomical models of two adults and two children for dosimetric simulations," *Physics in Medicine and Biology,* vol. 55, pp. 23 – 38, 2010.

[44] "Whole-Body Human Models". [Online]. Available: `http://www.itis.ethz.ch/index/index_humanmodels.html` [Accessed: Aug. 27. 2010].

[45] "Visible Human Project". [Online]. Available: `http://www.nlm.nih.gov/pubs/factsheets/visible_human.html` [Accessed: Jan. 20. 2011].

[46] "Visible Human". [Online]. Available: `http://escience.anu.edu.au/lecture/cg/CGIntroduction/printNotes.en.html` [Accessed: Aug. 27. 2010].

[47] "Italian National Research Council". [Online]. Available: `http://www.cnr.it/sitocnr/Englishversion/Englishversion.html` [Accessed: Aug. 27. 2010].

[48] Drossos, A., Santomaa, V. and Kuster, N. "The dependence of electromagnetic energy absorption upon human head tissue composition in the frequency range of 300-3000 MHz," *IEEE Trans. Microwave Theory Tech. ,* vol. 48, no. 11 pp. 1988 – 1995, 2000.

[49] Schmid & Partner Engineering AG, "SEMCAD X Manual," 2010.

A 10g averaged SAR results

The 10 g averaged SAR results for all combinations of distances, frequencies and locations are presented in Figures A1 - A12 below. In these graphs the SAR values obtained in the human phantom are compared to the respective SAR values recorded in liquid defined by both the IEC and FCC parameters. The other polarization on the same location is referred to as “H-pol”, i.e. when the antenna is rotated 90 degrees.

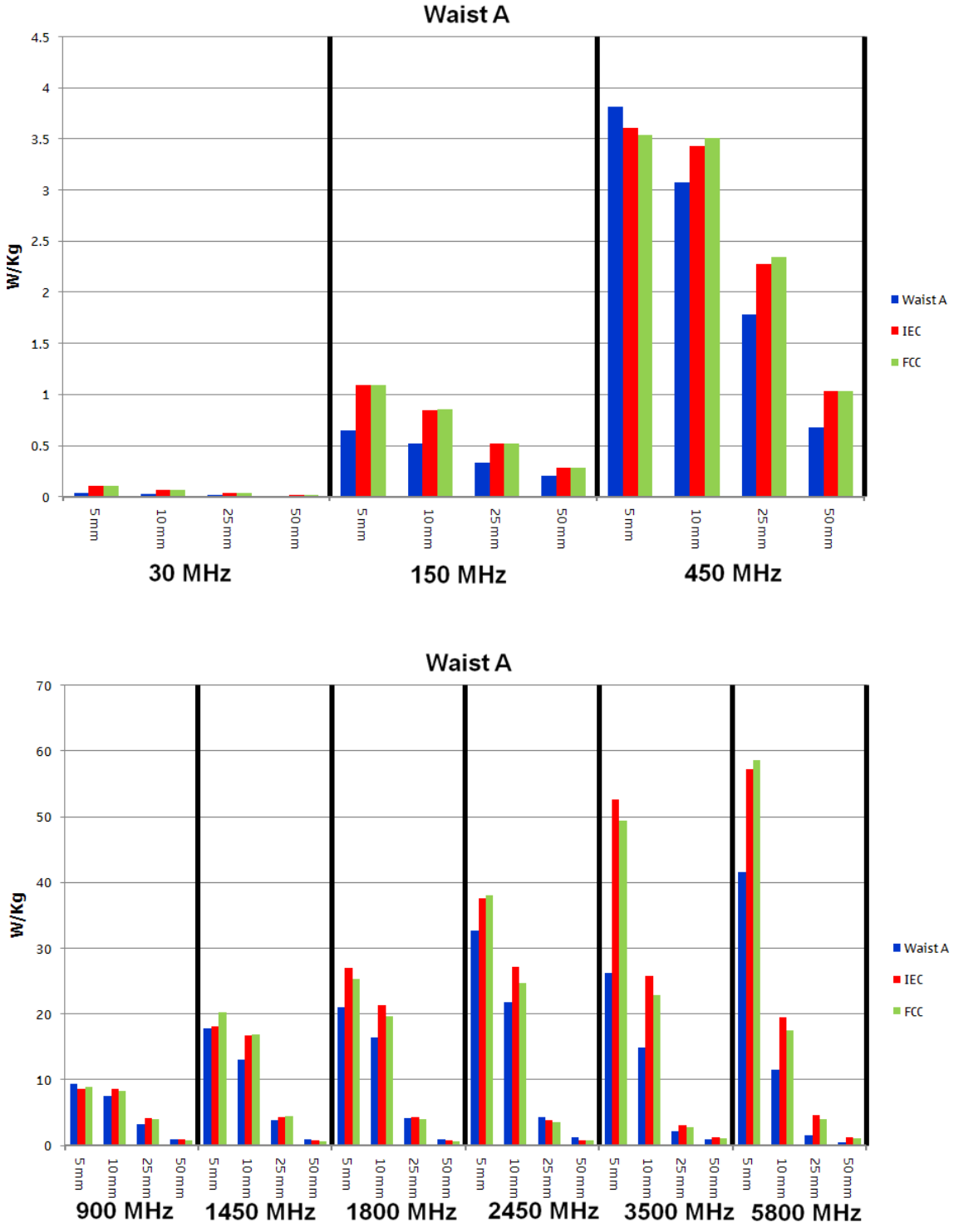

Figure A1: 10g averaged SAR (W/kg) in "Waist A" location.

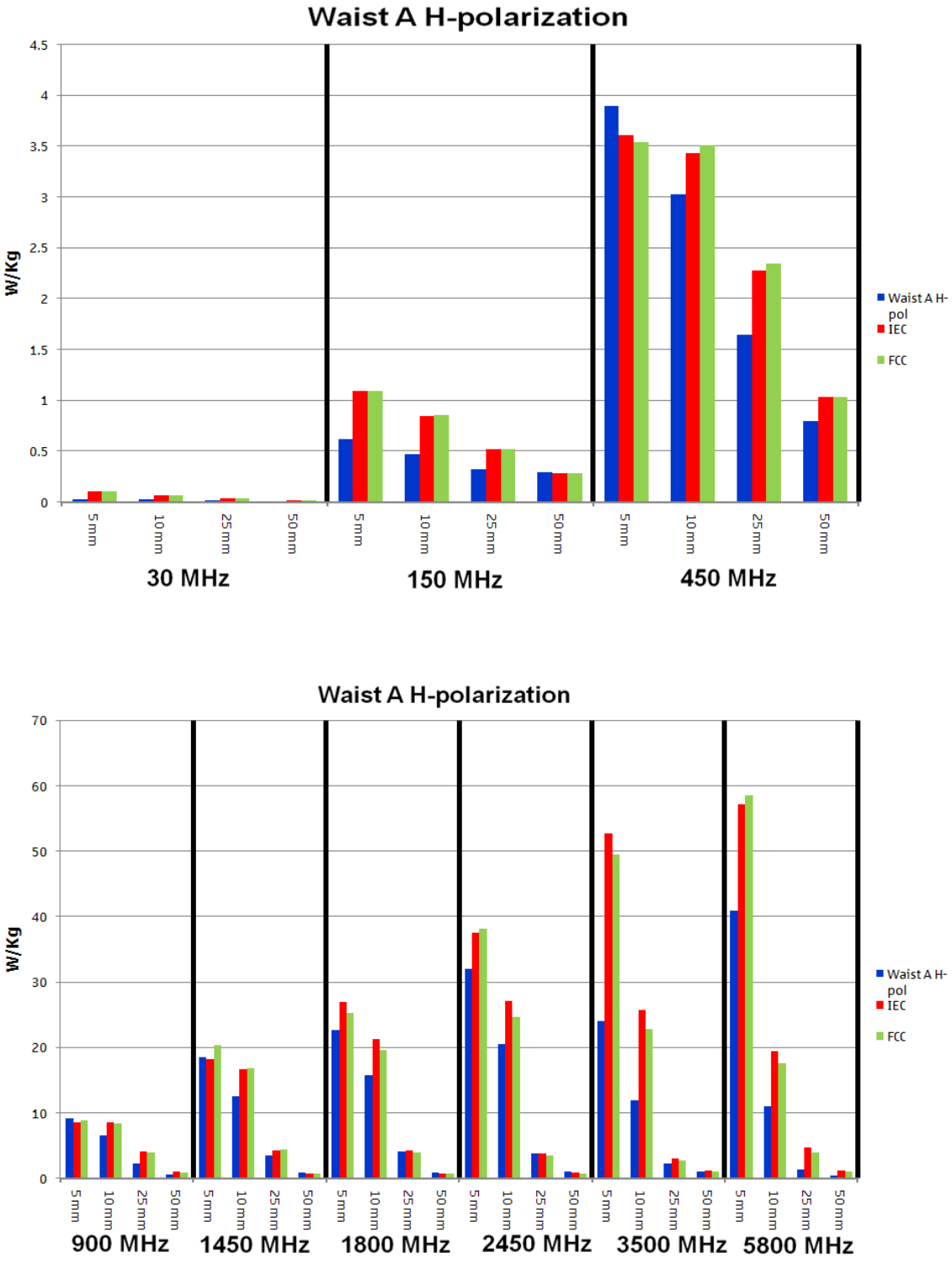

Figure A2: 10g averaged SAR (W/kg) in "Waist A" location.

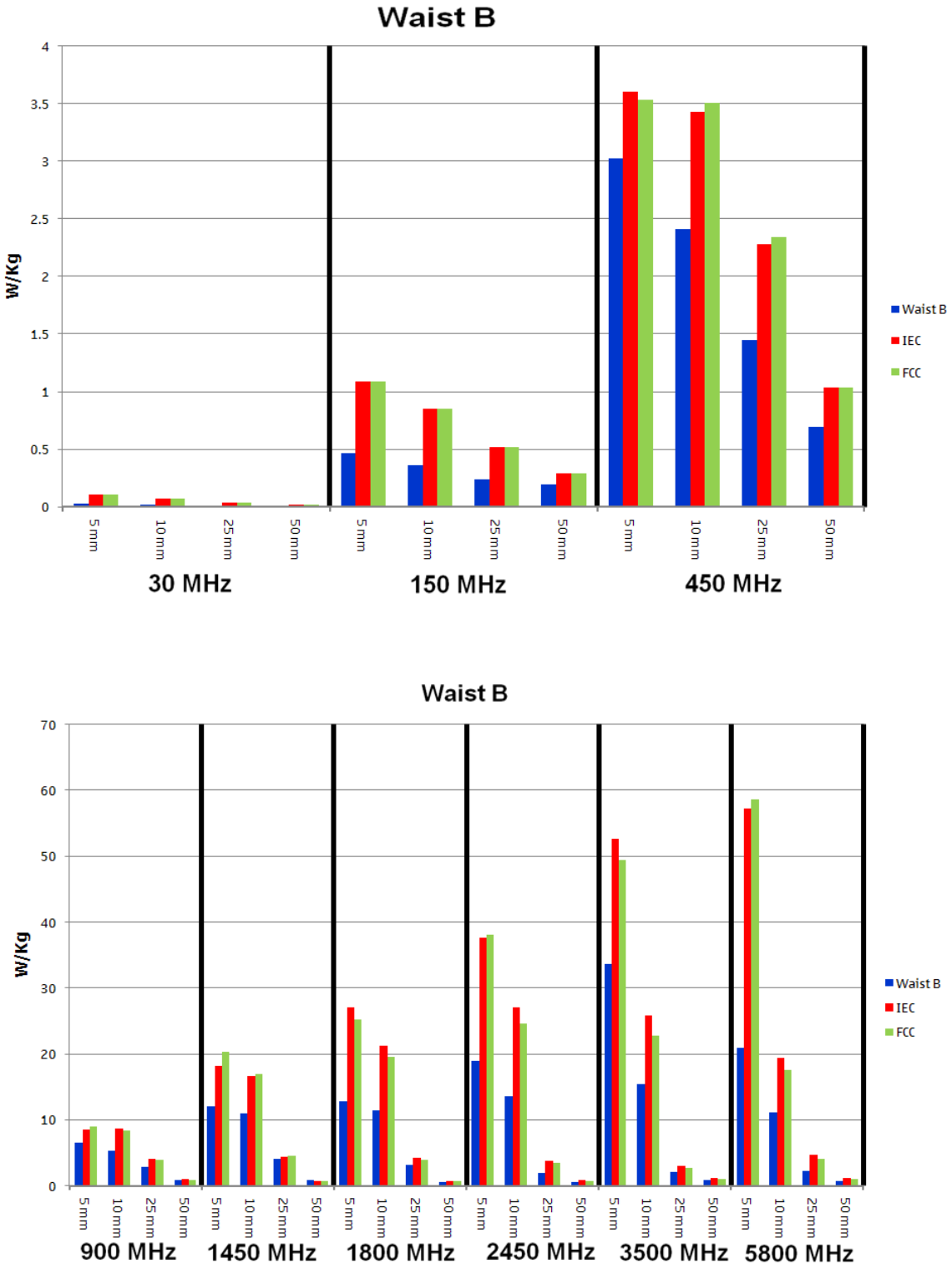

Figure A3: 10g averaged SAR (W/kg) in "Waist B" location.

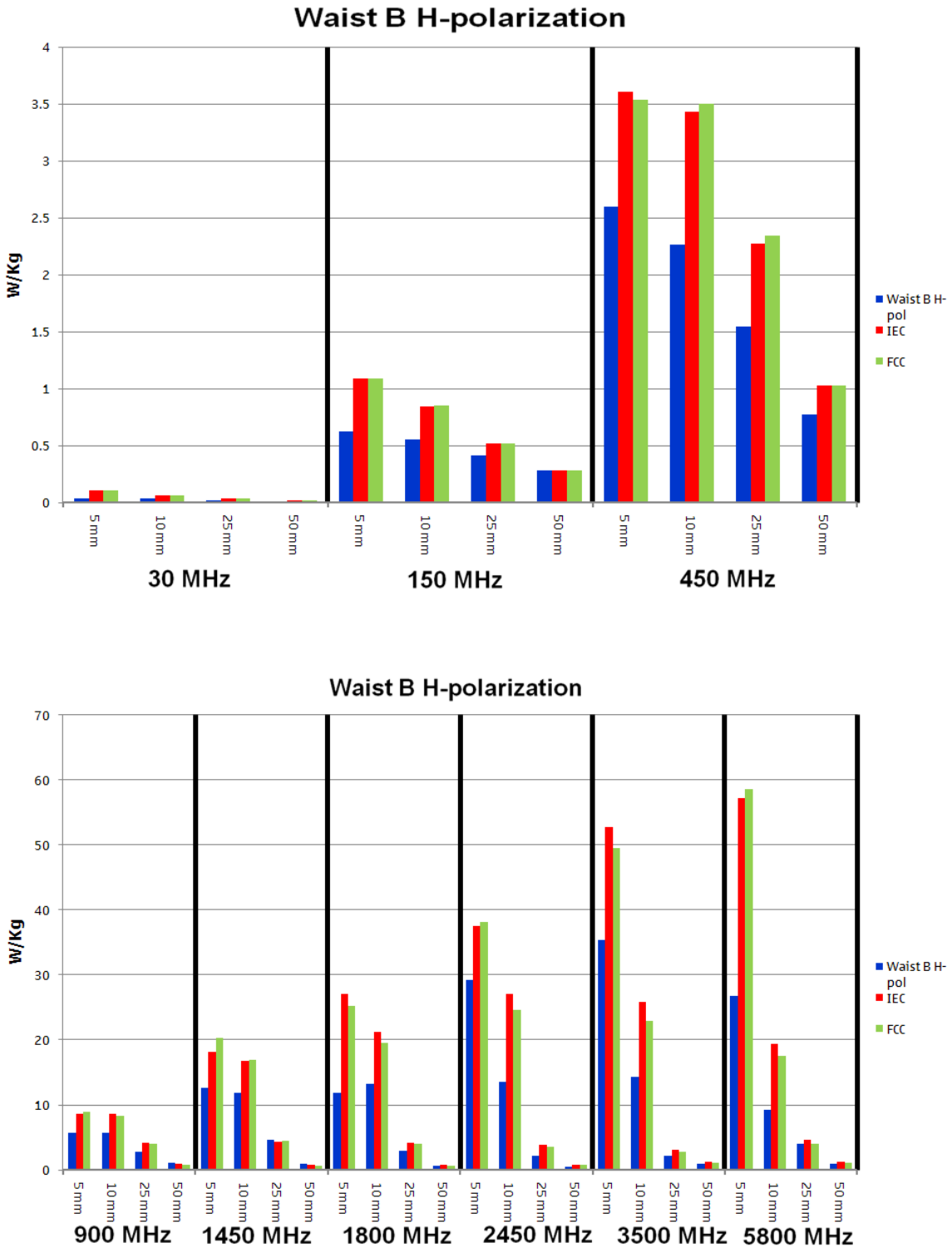

Figure A4: 10g averaged SAR (W/kg) in "Waist B" location.

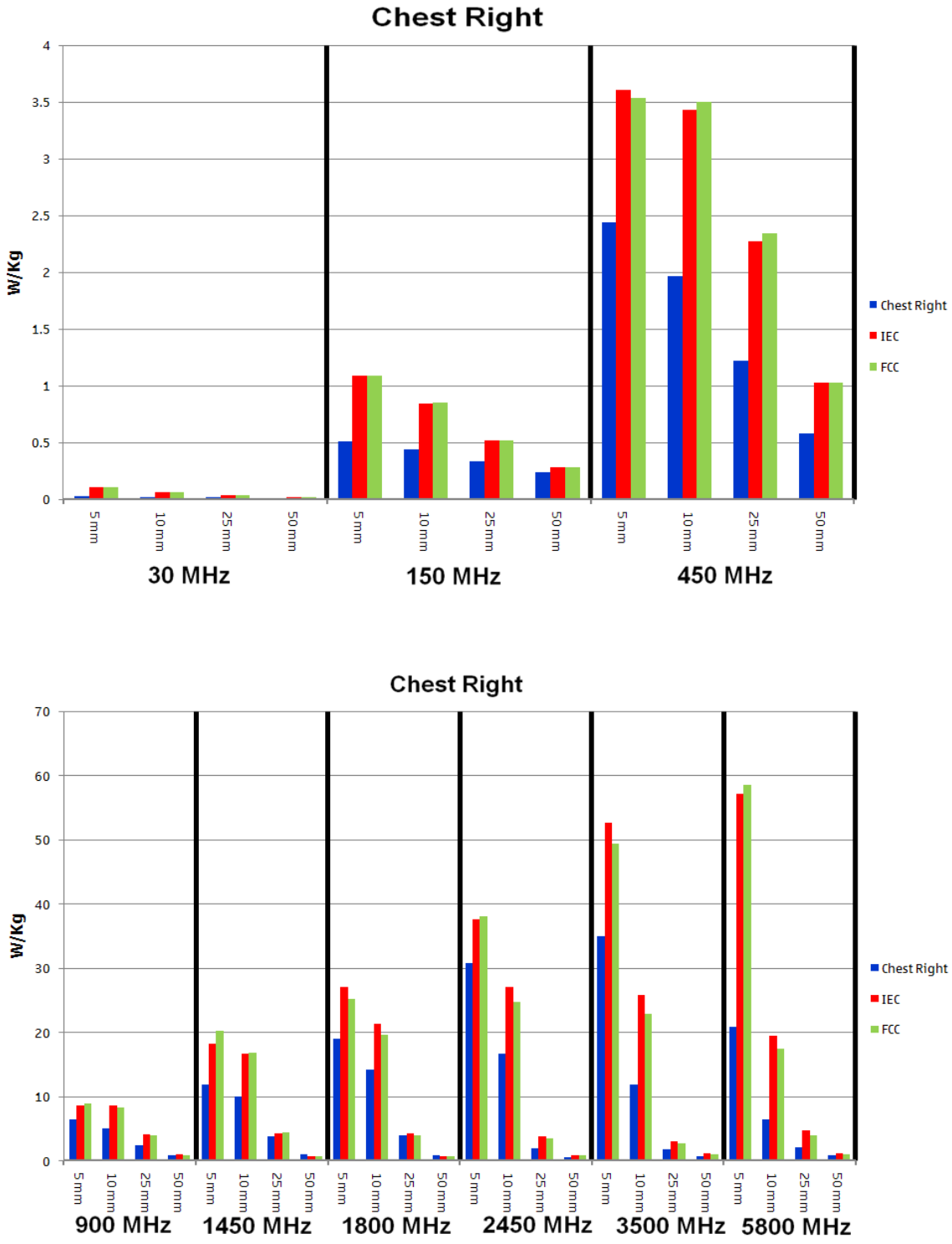

Figure A5: 10g averaged SAR (W/kg) in "Chest Right" location.

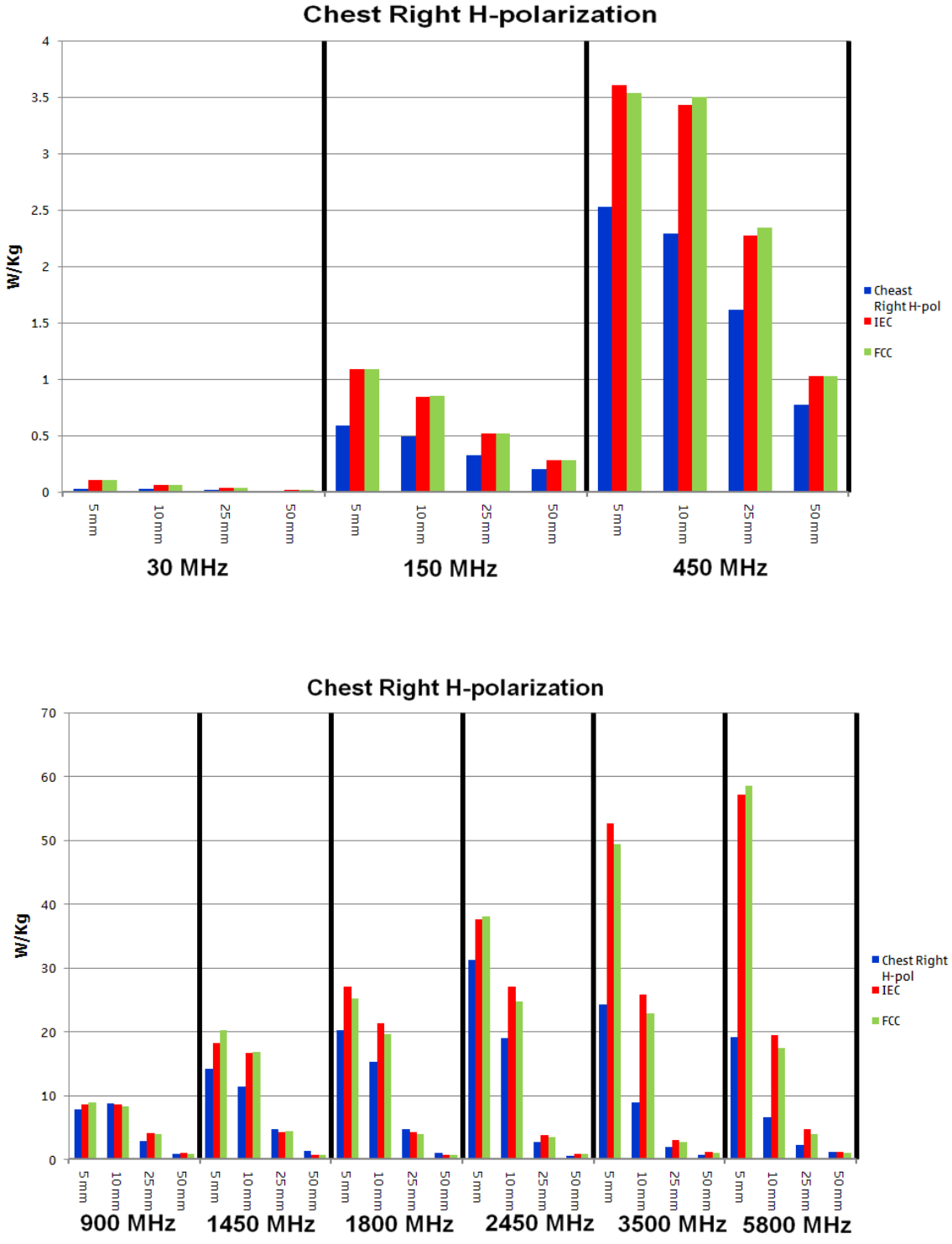

Figure A6: 10g averaged SAR (W/kg) in "Chest Right" location.

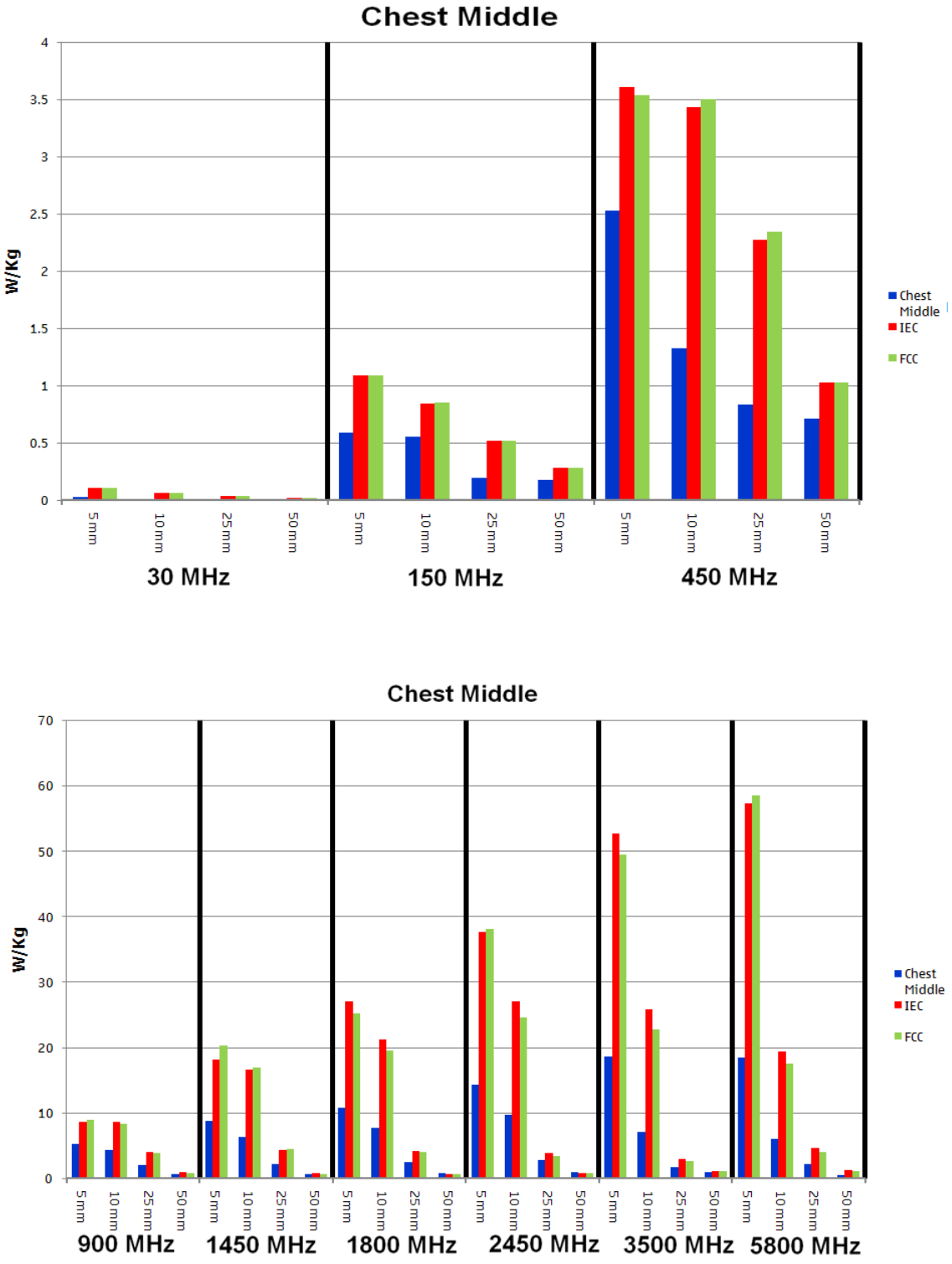

Figure A7: 10g averaged SAR (W/kg) in "Chest Middle" location.

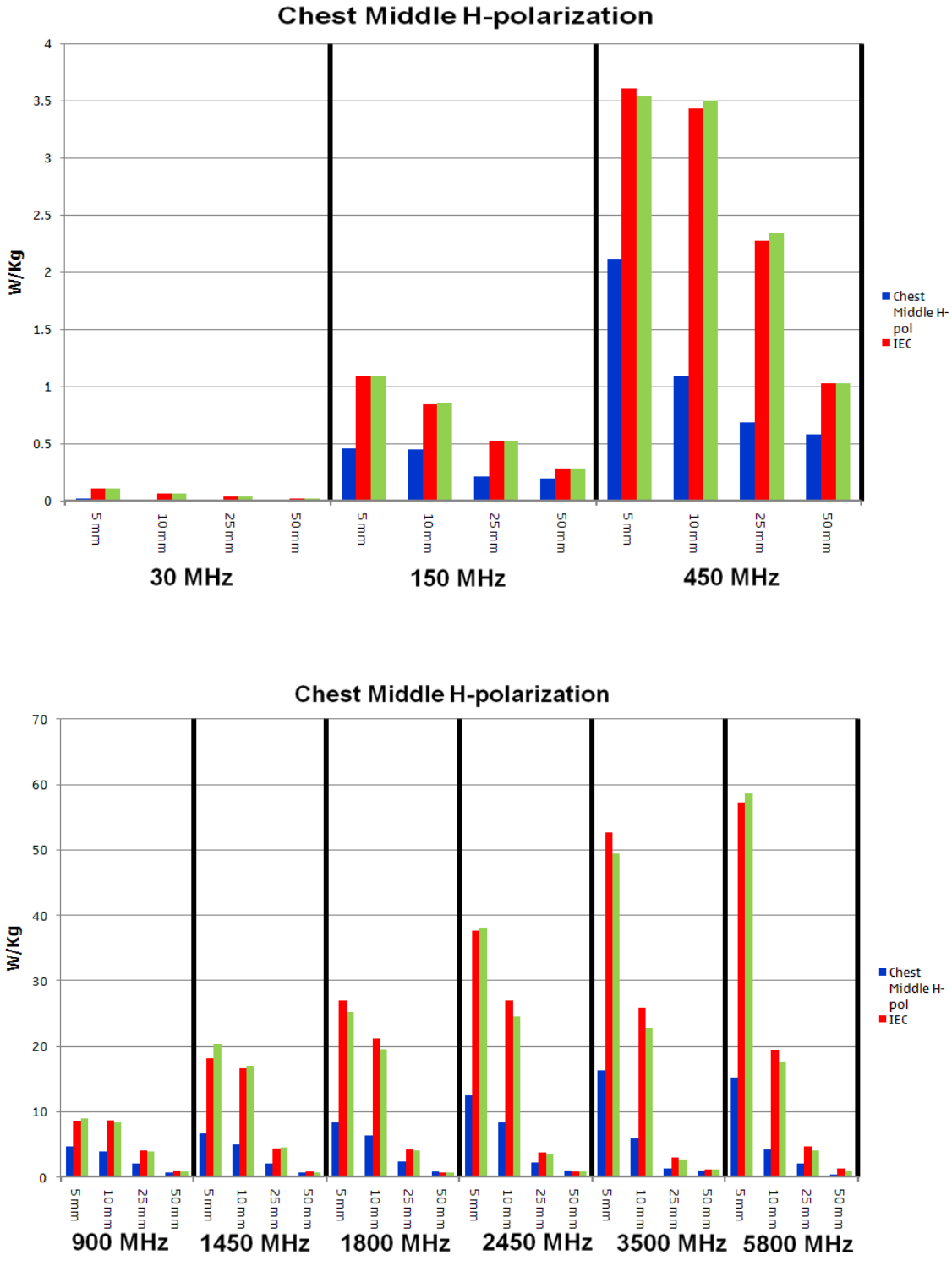

Figure A8: 10g averaged SAR (W/kg) in "Chest Middle" location.

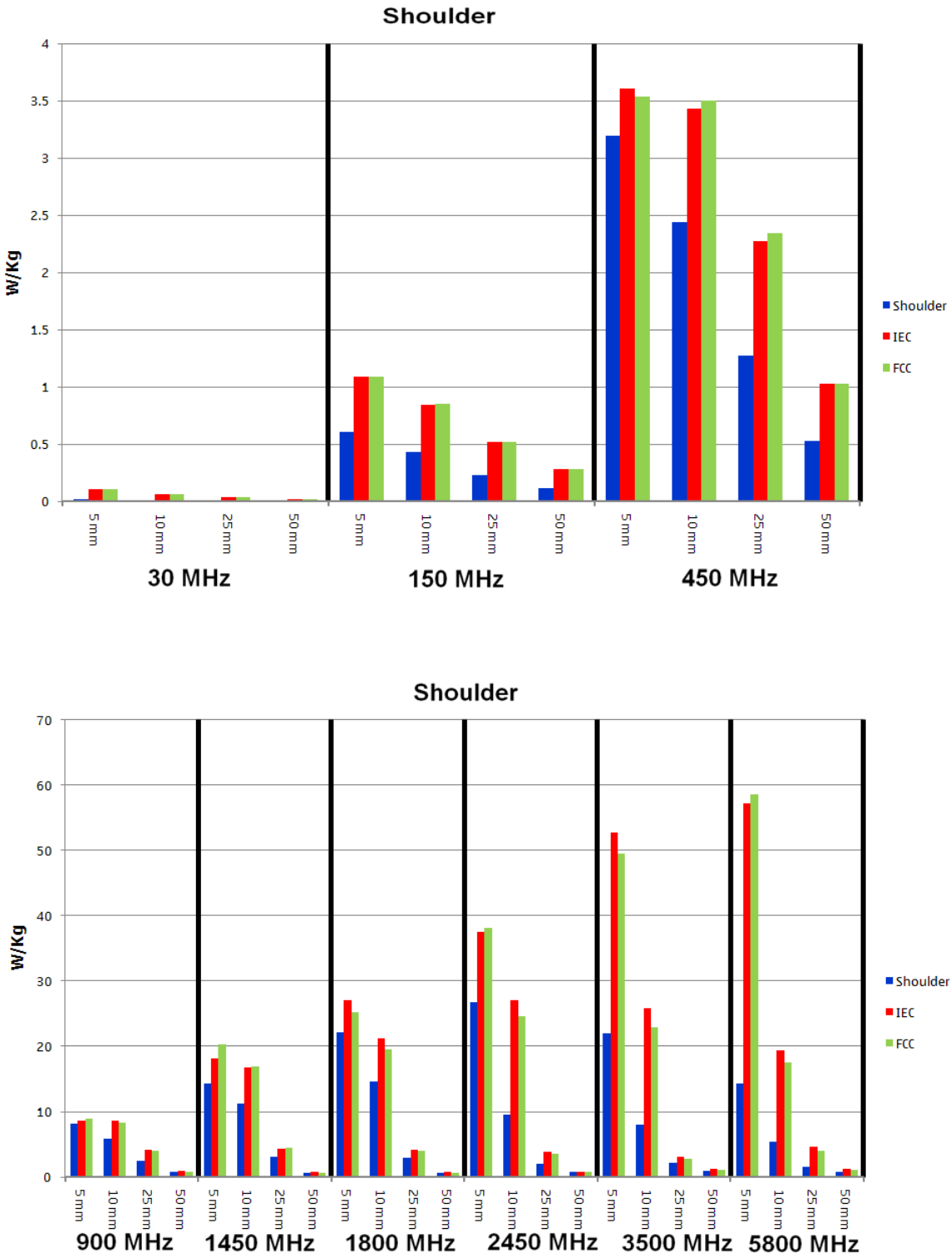

Figure A9: 10g averaged SAR (W/kg) in "Shoulder" location.

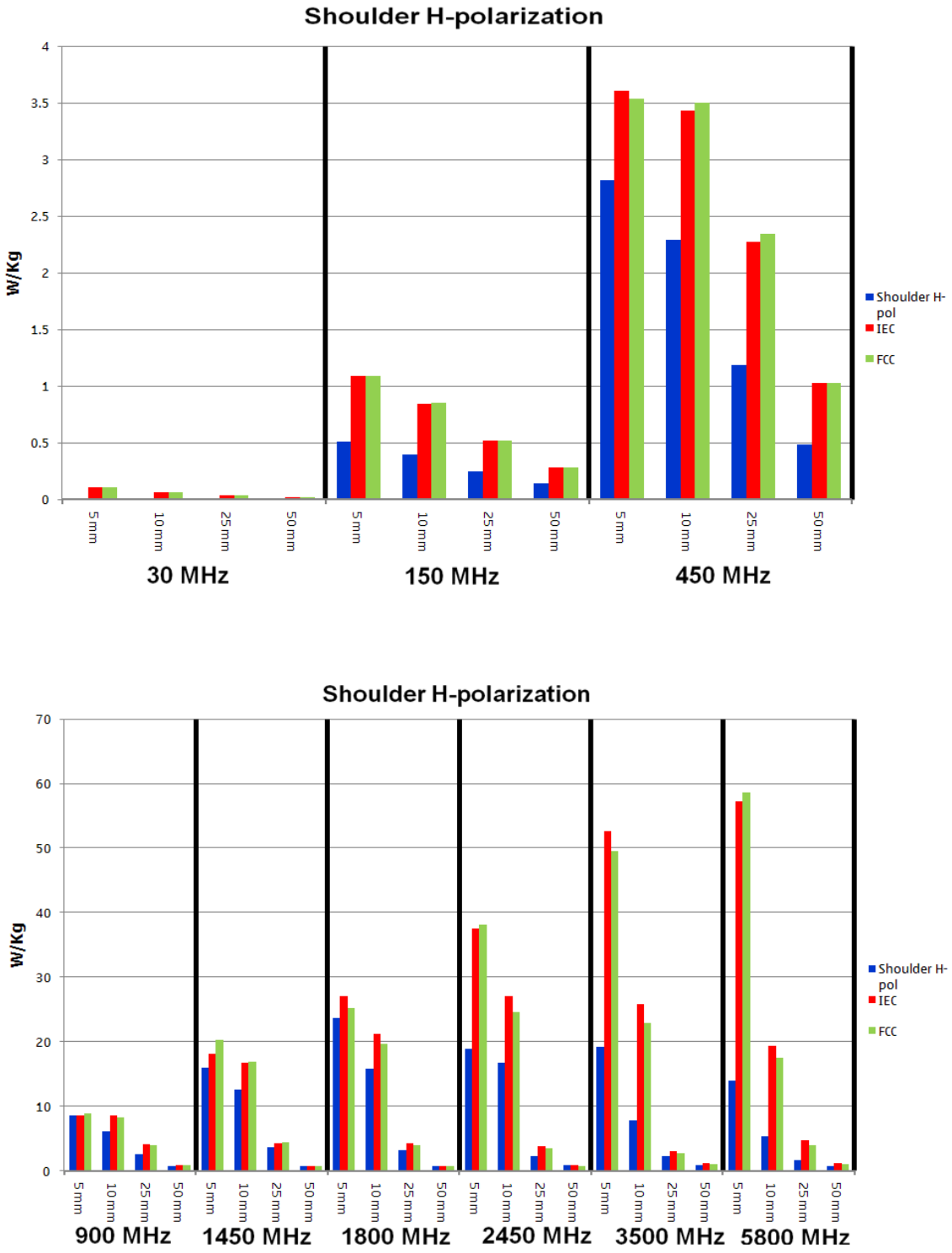

Figure A10: 10g averaged SAR (W/kg) in "Shoulder" location.

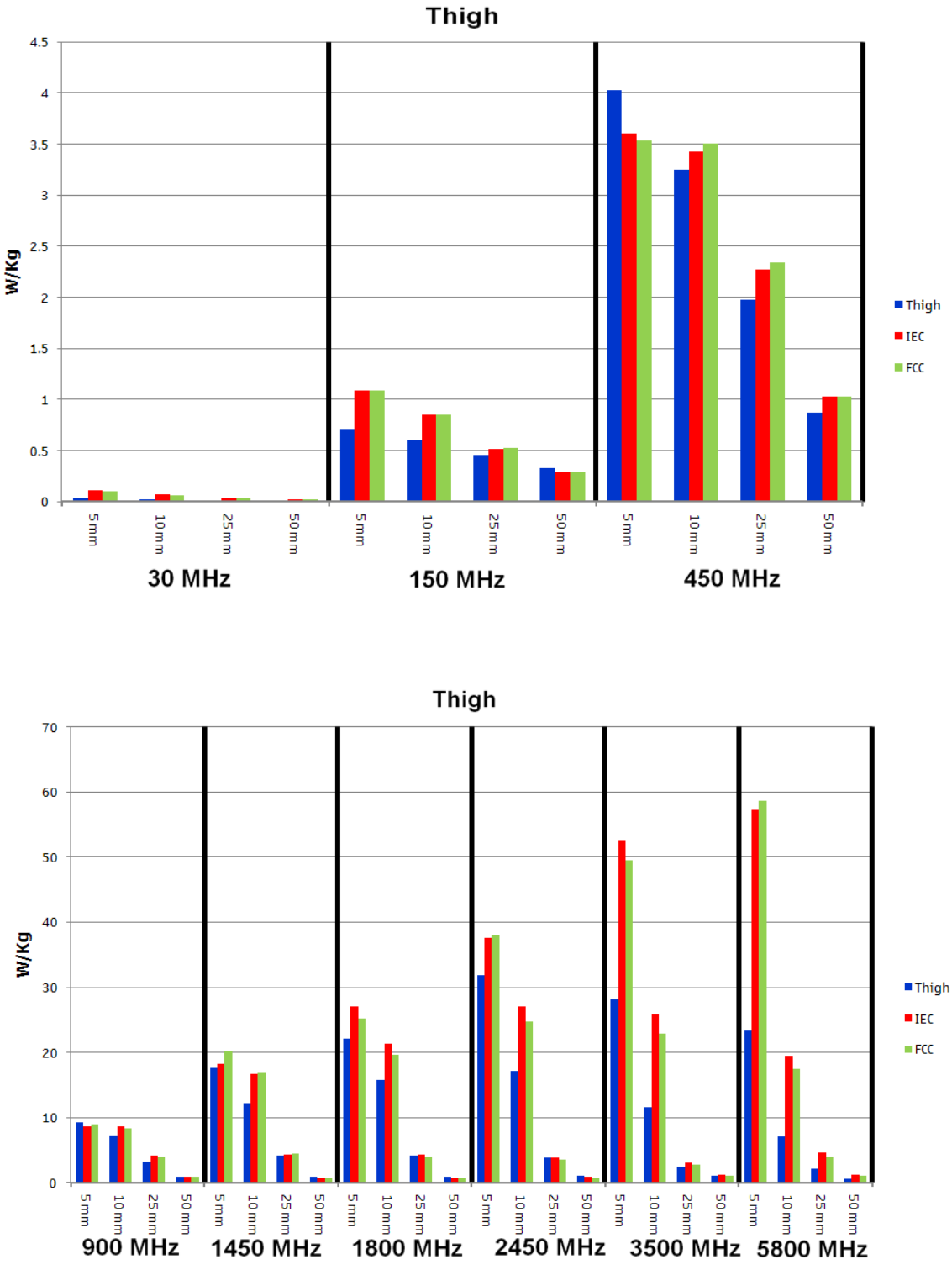

Figure A11: 10g averaged SAR (W/kg) in "Thigh" location.

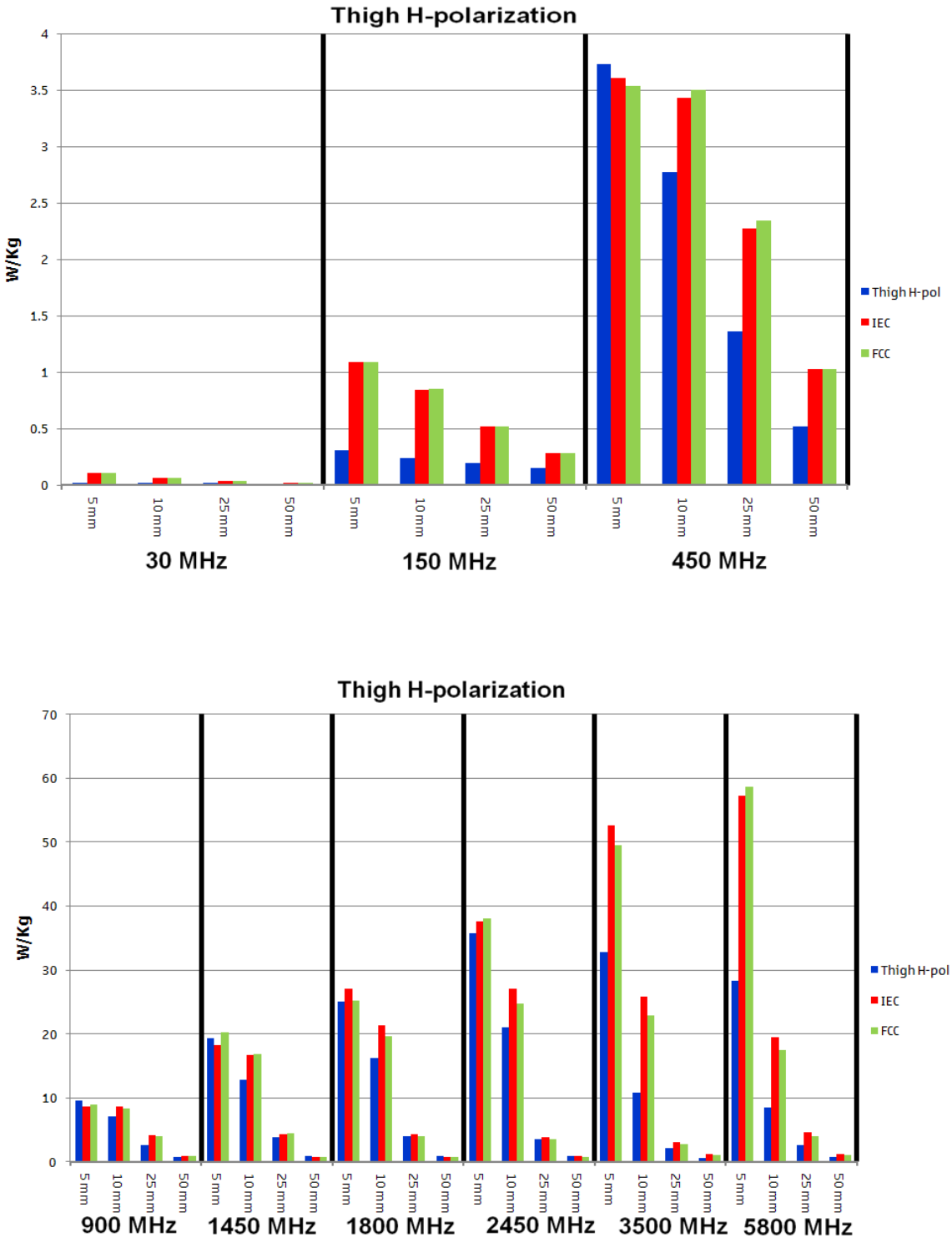

Figure A12: 10g averaged SAR (W/kg) in "Thigh" location.